Continuous Collective Strong Coupling Between Atoms and a High Finesse Cavity on a Forbidden Optical Transition

by

Julia R. K. Cline

B.A., Williams College, 2015

M.S., University of Colorado, 2018

A thesis submitted to the

Faculty of the Graduate School of the

University of Colorado in partial fulfillment

of the requirements for the degree of

Doctor of Philosophy

Department of Physics

2021

Committee Members:

James K. Thompson, Chair

Murray J. Holland

Adam M. Kaufman

Jun Ye

Vanja Dukic

Cline, Julia R. K. (Ph.D., Physics)

Continuous Collective Strong Coupling Between Atoms and a High Finesse Cavity on a Forbidden Optical Transition

Thesis directed by Prof. James K. Thompson

Over the last several decades, developments in the control and manipulation of cold atoms, ions, and molecules have opened new doors into our understanding of the universe. In particular, precision measurement and quantum information technology have provided a wealth of new knowledge. In this thesis, I present progress towards a continuous wave superradiant laser, a novel ultra-narrow linewidth laser and active frequency reference that promises to further advance precision measurement and quantum science.

In my thesis work, I have demonstrated a major milestone towards the creation of a superradiant laser with kilosecond coherence times: continuous loading and strong collective coupling of atoms to a high finesse cavity on a forbidden optical transition. To this end, I constructed a new experiment to guide atoms through a series of spatially separated laser cooling stages and deliver a continuous flux of atoms into a travelling lattice supported by a high finesse optical cavity. Unlike many cold atomic experiments that operate in a time-sequential manner, with distinct phases for sample preparation and measurement, this system delivers a truly continuous flux of atoms. This continuous atomic apparatus is the first to demonstrate steady-state strong collective coupling on a narrow linewidth atomic transition and has the highest phase space density of any continuous atomic beam. In addition to setting the foundation for the creation of a continuous wave superradiant laser, this work opens the door to a new generation of continuous cold atomic devices and a wealth of applications.

Dedication

To Jason, Bear, and Moose.

Acknowledgements

Earning a PhD has been a rewarding experience, but also a challenging one, and I wouldn't be here without the support of my family, friends, colleagues, professors, and mentors.

First, I would like to thank my parents, Daryl and Rick Cline. They have always been incredibly supportive and consistently encouraged me to design and build anything I could imagine. From soap-box cars for the local race to custom cabinets for my toys, I got my hands dirty in the workshop from a young age. I was equally encouraged to explore creative fields, making art with my mom and playing music with school bands. My parents instilled in me a simultaneous sense of pragmatism and optimism that has been incredibly valuable.

I'd like to thank my brother Ben for being un-endingly supportive, empathetic, and always excited to hear what is going on in lab. His zest for life is always inspiring and grounding - there is always another adventure to be had. Thank you for the bottomless box of passionfruit and good luck with baby Ollie!

In high school, my math teacher Susan Wildstrom and physics teacher Kismet Talaat piqued and encouraged my interest in science. Without Kismet's wonderful cartoon depictions of physics problems and Susan's clear and precise explanations of math, I doubt I would be where I am today.

My undergraduate thesis advisor Ward Lopes encouraged me to think critically and to investigate any idea I had, even if it turned out to be a terrible idea. Ward helped me develop as a researcher by making implicit skills explicit, for example by teaching me how to use lab notebooks and give presentations. Additionally, I'm thankful for Ward's compassion and understanding. When the school cafeterias closed for three weeks and Ward learned that none of his summer re-

search students knew how to cook, he invited us to his house and taught us how to cook, and then continued inviting us over for dinner every week to make sure we had at least one good meal.

In grad school I made the fantastic decision to join James Thompson's group. The combination of physics, engineering and James' emphasis on simple visual explanations have made this a far better choice than I could have known. James's passion for physics is contagious and his demand for accurate physical explanations has made me a much better physicist. During my time in the group, I have had the opportunity to work with some fantastic students, including Matt Norcia, Matthew Winchester, Dylan Young, Juan Muniz, Vera Schafer, and Zhijing Niu on the Strontium experiment, and Kevin Cox, Graham Greve, Baochen Wu, Chengyi Luo, and Vanessa Koh on the Rubidium experiment. Thank you all for the years of great discussions.

I would also like to acknowledge the entire staff of the machine, computing and electronics shops, without whom the apparatus would not exist.

I would like to thank my friends here in Boulder and further abroad who have brought balance and adventure to my life while I've pursued this degree. To the homework gang, Alex, Lucas, Jason, and Ellyn, thank you for making Jackson fun, or close enough to fun to be passable, and thank you for the games, corn-mazes, and pumpkin carving. To Allie, Charlie, Miranda, and Tanya, thank you for your kindness and friendship over the years. Thanks especially to Jason, who has been equally fun, good company, and supportive through the ups and downs of an experimental physics PhD.

Contents

Chapter

Tables

Table

Figures

Figure

Chapter 1

Introduction

A fundamental goal of physics is to expand the boundaries of what we know and understand. Over the last several decades, developments in the control and manipulation of cold atoms, ions, and molecules have opened new doors into our understanding of the universe. In particular, precision measurement and quantum information technology have provided a wealth of new knowledge, complementing and sometimes extending the results obtained by more established techniques in fields such as high energy and condensed matter physics.

Developments in atomic physics have been made possible by recent advancements in tools and techniques to prepare, manipulate, and detect cold atoms, ions, and molecules. There has been continuous progress in developing new techniques to prepare novel states of matter, including laser cooling and trapping methods, advancements in evaporative cooling, and breakthroughs in quantum gas assembly [1, 2, 3, 4, 5]. Advances in techniques for controlling particles with microwave and laser radiation have given scientists new handles with which to coherently manipulate quantum states and precisely engineer interactions between particles [6, 7, 8]. Finally, advances in techniques and technologies for detection have lowered noise floors and extended observations times, allowing the measurement of new phenomena in previously unobserved regimes [9, 10, 11].

Precision metrology in particular has enhanced our understanding of the universe by providing a wealth of new measurements and bounds for a variety of fundamental quantities. These quantities include the electron electric dipole moment [12, 13], the anomalous magnetic moment of the electron and fine structure constant [14], and precision tests of key predictions of relativity

[15, 16]. Additionally, precision frequency metrology has also been proposed as a means of studying quantum many-body physics [17, 18], searching for exotic physics [19, 20, 21] and exploring fundamental quantum limits imposed by gravity [22, 23, 24].

In this thesis, I present milestones on the journey towards a continuous wave superradiant laser, a novel ultra-narrow linewidth laser and active frequency reference for further advancing precision measurement and quantum science.

1.1 Superradiance: a Novel Active Frequency Reference

At the heart of this thesis is superradiance: a phenomena in which an ensemble of atoms emits photons at a greater rate than the sum of the rates at which photons would be emitted from the individual atoms. This section will give a brief overview of what superradiance is, where the idea originated from, and some of the motivations for using superradiance for precision metrology.

The idea of superradiance began in the 1950s when Robert Dicke first proposed the phenomenon of superradiance [25] and the field has slowly grown over the last few decades [26, 27, 28]. Over the last ten years, superradiance has been observed in a wide variety of platforms including atoms trapped in the near field of a photonic crystal waveguide [29], lattice-confined atoms inside hollow core fibre [30], and quantum dots in a nanophotonic waveguide [31].

In 2010, Murray Holland's group at JILA proposed the creation of a superradiant laser based on an ultra-narrow optical atomic transition, a cutting-edge approach to dramatically improve laser stability that has the potential to achieve optical coherence times on the order of kiloseconds [32, 33]. A superradiant laser has promise to be a robust frequency reference that could operate outside the extremely low vibration environment of a precision laser laboratory.

The interest in a superradiant laser is in large part because it operates in a novel regime that promises to overcome a challenge for the current state-of-the-art frequency references: cavity frequency noise. Optical atomic clocks, which are the most precise and accurate absolute frequency references to date [34, 35, 36, 37, 38, 39, 40, 41, 42, 43, 44, 45] are limited by the frequency stability of the lasers used to probe them. The primary limitation on laser frequency stability is set by thermal

and environmental vibrations of the laser reference cavities [46, 47, 48] to which lasers are frequency stabilized. The main culprit is thermal brownian motion in the spacer, mirror substrates, and reflective coatings [49, 50]. This is a difficult problem: the performance of the world's most stable laser for time-keeping and the world's most sensitive large-scale interferometer for the detection of gravitational waves, Advanced LIGO, as well as cavity opto-mechanics experiments, are all limited by this fundamental noise source.

In a superradiant laser, the phase information is primarily stored in the collective, radiating dipole of laser-cooled and trapped atoms. This is in contrast to more conventional lasers, where the phase information is primarily stored in a large intracavity light field. The intracavity light field interacts strongly with the noisy laser cavity mirrors, decreasing the frequency stability of the laser. In the superradiant laser regime, the light directly inherits a collectively enhanced coherence time of the atoms. Thus, the optical coherence can be more than 10^5 times less sensitive to the laser mirror noise and vibrations.

From another perspective, because the light emitted from a superradiant laser comes directly from a narrow-linewidth atomic transition, one can view a superradiant laser as an active optical frequency reference. A superradiant laser is essentially the optical equivalent of a maser, which is an active microwave frequency standard [51]. The power of working at optical frequencies can be seen in the great improvement in the performance of atomic clocks moving from the microwave to the optical domain. Because of the higher operating frequency, the fractional frequency stability and accuracy of optical clocks quickly overtook their microwave counterparts, and are now several orders of magnitude more favorable.

Preliminary proof-of-principle superradiance experiments were conducted by previous members of the Thompson lab using both rubidium and strontium atoms. The model rubidium system demonstrated operation in the superradiant regime where spontaneous synchronization of more than one million rubidium atomic dipoles was sustained by less than 0.2 photons on average inside the optical cavity [52]. This experiment used Raman transitions to create an effective long-lived optically excited state in an ensemble of cold rubidium atoms. In this case, frequency noise on the

"dressing" laser used to create the Raman system appears on the laser output, so it is not useful as a frequency reference, but had great use for studying many aspects of steady-state superradiance [52, 53, 54, 55].

The next step in the trajectory of the superradiant laser was to switch to atomic strontium, which has several narrow-linewidth optically excited states that are suitable for the operation of a true narrow linewidth optical superradiant laser. The underlying reason is that strontium has two valence electrons (as opposed to rubidium's single valence electron). The intrinsic magnetic moments, or spins, of these two electrons can either be aligned in a configuration known as a "triplet" state, or anti-aligned in a configuration known as a "singlet" state. Moving from a singlet state to a triplet state or vice-versa requires flipping the spin of one of the electrons. Photons are very bad at doing this, so these transitions are called "forbidden" or "dipole-forbidden" and happen very slowly. The work here uses two such transitions in atomic strontium: the somewhat forbidden 7.5 kHz linewidth $^3P_1$ to $^1S_0$ transition and the far more forbidden 1 mHz linewidth $^3P_0$ to $^1S_0$ clock transition. These narrow-linewidth transitions in strontium and similar elements have enabled the development of optical atomic clocks, which are the most precise and accurate absolute frequency references to date [34, 35, 36, 37, 38, 39, 40, 41, 42, 43, 44, 45].

A continuous wave superradiant laser based on the mHz linewidth optical clock transition in strontium offers the potential to improve the short-time performance of optical atomic clocks even further. Just before I joined the Thompson lab, Matt Norcia built a strontium system and demonstrated pulsed and quasi-steady state lasing on the 7.5 kHz linewidth transition in ^{88}Sr [56]. Similar experiments have since demonstrated superradiance on the $^3P_1$ to $^1S_0$ transition in calcium [57] and again in strontium [58]. These works are further milestones on the journey towards a superradiant laser, but to achieve kilosecond coherence, a superradiant laser must be operated on an atomic transition about 10^4 times narrower in linewidth, such as the mHz linewidth optical clock transition in the fermionic isotope ^{87}Sr.

In this thesis, I present our work on two major fronts: moving from the narrow kHz to the ultra-narrow mHz optical transition in strontium and moving from a pulsed to a continuous

experimental apparatus.

1.2 First Generation Experiments

Before beginning the construction of the continuous strontium experiment, I contributed to several experiments that I will mention briefly here. These experiments were performed on the strontium cavity QED apparatus with fellow graduate students Matt Norcia and Dylan Young, postdoc Juan Muniz, and undergraduate student Matthew Winchester. They include a novel form of cavity-enhanced atomic spectroscopy we call magnetically induced transparency [59], a new method of laser cooling with reduced reliance on spontaneous emission [60, 61], a method of enhancing the sensitivity of proposed atomic gravitational wave detectors [62], an investigation of cavity-mediated spin-spin interactions [63], a direct quantum nondemolition detection of a millihertz linewidth optical atomic transition [64], an observation of dynamical phases of matter that are precluded from existence at equilibrium but can be stabilized by driving a system out of equilibrium [65], and a new class of laser (a "superradiant laser") based on optical superradiance from ultra-narrow linewidth transitions [66, 67]. As part of the pulsed superradiant laser project, we demonstrated the most precise active absolute frequency standard realized to date, providing an encouraging indication that a superradiant laser may become a key experimental tool for precision measurement in the near future.

Below I briefly expand upon three of those research areas: a pulsed superradiant laser on a milihertz optical transition, cavity-mediated spin-spin interactions, and a new form of laser cooling that relies on narrow-linewidth transitions.

1.2.1 A Pulsed Superradiant Laser on a Milihertz Optical Transition

We demonstrated superradiant emission from the 1.35(3) mHz linewidth clock transition [64] in an ensemble of laser-cooled ^{87}Sr atoms trapped within a high-finesse optical cavity [66]. The cavity decay rate far exceeded both the atomic dissipation and the rate of coherent interactions, placing us deep in the superradiant regime. We showed that atoms collectively emitted photons

into the cavity, up to 10,000 times faster than independently radiating atoms.

To characterize the frequency of our pulsed superradiant laser, we compared our laser to a state-of-the-art cavity-stabilized laser [68, 69] and optical lattice clock [40] in Jun Ye's lab. We observed a fractional Allan deviation of $6.7(1) \times 10^{-16}$ at 1 second of averaging and established absolute accuracy at the 2 Hz (4×10^{-15} fractional frequency) level [67]. The short term frequency stability was within an order of magnitude of the record in an atomic frequency reference at the time, which was encouragingly close given the maturity and careful engineering of optical lattice clocks. Furthermore, the short-term stability greatly surpassed that of existing active atomic frequency references (masers), which operate at microwave frequencies [70, 71], making ours the most precise active frequency reference demonstrated to date.

We also characterized the sensitivity of the superradiant laser to perturbations such as cavity frequency shifts and magnetic fields. We demonstrated a reduction in sensitivity to changes in cavity frequency by $5(3) \times 10^5$ compared to a conventional laser. Additionally, we demonstrated insensitivity to magnetic fields by populating and lasing on both stretched states simultaneously. These observations were very encouraging for the prospect of creating an even more precise superradiant frequency reference.

1.2.2 Cavity-Mediated Spin-Spin Interactions

Ensembles of atoms have emerged as powerful quantum simulators of many-body physics. We demonstrated a new approach to engineering controllable interactions between the atoms, where two atomic states connected by a clock transition each serve as an effective spin and long-range spin-exchange interactions are mediated by the cavity photons [63].

When our optical cavity is on resonance with a narrow linewidth optical transition, the primary effect is superradiance, or an increase in the rate of decay of atoms from the excited state. When our optical cavity is detuned from atomic resonance, interesting Hamiltonian dynamics emerge, which we can describe as spin-exchange interactions mediated by the emission and reabsorption of photons inside an optical cavity. In our case, these interactions manifest as

a one-axis twisting (OAT) term and a self-energy term that leads to a so-called many-body gap protection.

OAT has been demonstrated in driven systems as a way to create entangled spin-squeezed states [6, 72, 73, 74]. In our system, the atoms themselves create the drive that leads to twisting, an idea which was also independently proposed in Ref. [75]. Experimentally, we used the superradiant light exiting the cavity as a precise realtime nondestructive probe of the atomic evolution [54]. We observed frequency shifts of the superradiant light versus atomic inversion to characterize the OAT dynamics at the mean-field level.

The many body energy gap term could be potentially used to protect optical coherence against dephasing. A similar effect, mediated by collisions between atoms, has been observed and utilized in optical magnetometers [76], and cold-atom systems [77, 78, 79]. We demonstrated the emergence of the many-body energy gap and signatures of gap protection of the optical coherence against dephasing. To demonstrate the gap protection, we introduced controllable, reversible dephasing to perform a direct spectroscopic measurement of the many-body energy gap.

This work has important implications for understanding potential perturbations to the superradiant laser and may enable future applications for entanglement enhanced metrology and for explorations of rich quantum many-body dynamics.

1.2.3 A Novel Laser Cooling Mechanism

The development of laser cooling revolutionized atomic physics. Typically, laser cooling relies on broad-linewidth optical transitions. Techniques similar to those used on broad transitions have been extended experimentally to narrow linewidth transitions [80, 81, 82, 83, 84, 85], but the conceptual framework used to understand the cooling is very similar to the broad linewidth case. The use of narrow linewidth optical transitions opens up fundamentally new possibilities for laser cooling beyond those previously explored.

We discovered and demonstrated a novel cooling mechanism in which large accelerations can be achieved on optical transitions with low scattering rates [60]. We named it sawtooth wave

adiabatic passage (SWAP) cooling. By sweeping the frequency of counter-propagating laser beams in a sawtooth manner, we adiabatically transfer atoms from the ground state to a long-lived optically excited state and back to the ground state. The time-ordering of these adiabatic transfers is determined by Doppler shifts, which ensures that in each sweep, the atom receives two photon recoils in the direction opposite to the its motion. The slowing process ends when the Doppler shift is comparable to the Rabi frequency of the beams, so the time-ordering is no longer well determined.

Because this technique reduces reliance on spontaneous emission, it may be an appealing mechanism for the cooling of molecules, which often lack closed cycling transitions. Moreover, from a technical perspective, SWAP cooling has the advantage of being a much more robust cooling technique for narrow linewidth transitions, as it has low sensitivity to long-term laser frequency drifts and to perturbations of the atomic transition frequency.

We extended this 1D observation to a SWAP magneto-opical trap (MOT), a related mechanism that provides a confining force as well as a cooling force [61]. This mechanism utilizes a similar sawtooth ramp to SWAP cooling, but relies on shelving atoms in one of several long-lived excited states to generate a differential scattering force that depends on the local magnetic field, which allows for the formation of a magneto-opical trap (MOT). In contrast to SWAP cooling, where only occasional spontaneous emission is required, our SWAP MOT relies heavily on spontaneous emission to reset the atom to its ground state at the beginning of each sweep.

We accidentally discovered this technique when Matt pushed a button on a function generator that switched the frequency modulation of the red 3D MOT beams from a symmetric triangle ramp to a sawtooth triangle ramp and we immediately saw two times more atoms loaded into the lattice. From a practical perspective, a SWAP MOT has proved to be very useful in our experiment and forms the basis of our cooling in everyday operation. It benefits from a simpler laser system, a larger capture fraction from higher temperature samples, improved robustness, and the ability to operate in the presence of large inhomogeneous broadening of the atomic transition frequency.

We worked with graduate student John Bartolotta from Murray Holland's group to under-

stand the phenomenon [86] and they went on to extend the theoretical explanation to SWAP cooling in a magneto-optical trap [87], present a method of speeding up particle slowing using shortcuts to adiabaticity [88], and understand entropy transfer from a quantum particle to a classical coherent light field [89].

Since our initial demonstration, SWAP cooling has been rapidly adopted by many groups. Here I will highlight a few follow-up works: a similar demonstration of a SWAP MOT in strontium [90], SWAP slowing of dysprosium [91], SWAP cooling on a Raman transition [92], observation of SWAP cooling in atom–ion collisions [93], as well as theoretical calculations with non-cycling transitions [94] and polar molecules [95].

1.3 Why Continuous Wave Superradiance?

While the spectral properties of the pulsed superradiance explored in 1.2.1 are encouraging, the frequency stability was limited by the pulsed nature of the experiment. The fractional frequency stability at 1 s averaging time of $6.7(1) \times 10^{-16}$ was Fourier limited by the finite pulse length of typically 50 ms [67]. Extending the superradiant pulse length to steady-state or quasi-steady state lasing promises to dramatically improve the short-term frequency stability.

A continuous wave superradiant laser shows promise to improve the demonstrated short-term frequency stability by potentially 2 orders of magnitude from that of the pulsed superradiant laser, potentially outperforming current state-of-the art frequency references at short times. For example, if a steady-state superradiant laser were operated on the mHz transition with a similar output power to what has been demonstrated in pulsed mode and continued to be dominated by photon shot noise out to an averaging time of one second, we would expect to see an improvement in the 1 s fractional Allan deviation by a factor of roughly 10^2 compared to pulsed operation with a single 50 ms long pulse each second. The rapid improvement arises because the Fourier-limited linewidth would be reduced by 20 and simultaneously 20 times more photons would be collected, reducing the standard quantum noise by a factor of $\sqrt{20}$ and allowing the line to be split more precisely.

There are two ways to extend the pulse length: to repump the atoms that have emitted a photon back to the excited state as demonstrated in [52, 56], or introduce fresh atoms already prepared in the excited state and discard atoms that have decayed to the ground state.

The most likely pathway for the repumping approach involves exciting the atoms from $^1S_0$ to $^3P_1$ with a laser at 689 nm, then to $^3S_1$ with a laser at 688 nm. From there, the atoms will decay into all of the ^3P states. An atom that lands in $^3P_1$ will be pumped back to $^3S_1$ and have another chance to decay into $^3P_0$, but additional lasers at 707 nm and 679 nm would be needed to pump atoms out of the $^3P_2$ states and the undesired $^3P_0$ sublevels, respectively. The number of photon recoils imparted on the atoms to reach a particular sublevel within $^3P_0$ is high (several 10's, depending on details), so the atoms would be heated out of the lattice after emitting a few photons. Cooling during the repump process is possible, but each scheme we identified has difficulties: Raman sideband cooling within $^3P_2$ does not address the loosely-confined radial directions and other sub-Doppler cooling methods require high intensities that may perturb the lasing transition frequency. Cooling on the 57 kHz linewidth $^3P_2$ to $^3D_3$ transition at 2.9 μm avoids coupling directly to the lasing transition and has just recently been demonstrated [96].

Besides heating atoms out of the lattice, repumping has two main other challenges: the 679 nm laser used to transfer atoms between $^3P_0$ sublevels would likely lead to large perturbations to $^3P_0$ that would degrade the stability of the superradiant laser. Repumping also requires replacement atoms to compensate for atom loss due to heating and collisions with background gas.

The other approach to maintaining inversion is to supply fresh atoms in the excited state. This steady-state supply of atoms requires a fundamentally different mode of experimental operation than used in typical atomic physics experiments. Typical experiments operate in a time-sequenced manner and for much of the sequence, atoms remain in the same spatial location as fields are turned on and off in time. Like most cold atom experiments, the pulsed apparatus operates in this manner. However, in a continuous atomic experiment, operations have to be performed in spatially separated regions and atoms needs to be transported continuously between stages. This approach is challenging because it is much harder to create a magnetic field or laser beam whose properties

vary abruptly in space than in time. Experiments with a high phase space density cold atomic beam are difficult and quite new: this thesis reports the second such experiment of its kind. The first is from the group of Florian Schreck at the University of Amsterdam and realized an ultracold Bose-Einstein condensate in steady state [97, 98, 99, 100].

We decided to go with the continuous atom approach because of the difficulties with repumping and the fact that a continuous stream of new atoms would be required anyway to compensate for losses. Within the steady-state approach, there are two main methods of supplying new atoms: a hot atomic beam traversing an optical cavity [101] and a cold atomic beam continuously loaded into a lattice supported by the cavity. We decided to go with the latter approach, as has a group at the Quantum Metrology Institute at the National Physical Laboratory in the UK, and the group of Florian Schreck at the University of Amsterdam is following both approaches.

In this thesis, I present a milestone towards a continuous wave superradiant laser: continuous loading and strong collective coupling of atoms to a high finesse cavity on a forbidden optical transition.

1.4 Outline of Thesis

The rest of this thesis is organized as follows: In Chapter 2, I describe the design and construction of the experimental apparatus. In Chapter 3, I demonstrate the continuous loading of a high flux of strontium atoms into a high finesse optical cavity. In Chapter 4, I demonstrate steady-state strong collective coupling between atoms and an optical cavity, on a narrow linewidth atomic transition. Finally, in Chapter 5 I provide an outlook to future extensions of this work and a rough outline for a possible experimental implementation of a steady-state superradiant laser.

Chapter 2

Experimental Apparatus

In this chapter, I describe the design principles of our experiment and the basic experimental hardware and processes that allows us to operate our experiment.

2.1 Design Principles

The goal of this experiment is to set the stage for continuous wave superradiance. We would like to deliver a continuous, high flux of strontium atoms into a lattice supported by a high finesse optical cavity, while minimizing atomic decoherence and scattering. In other words, the rate of collective interactions between the atoms and cavity, mediated by the mHz linewidth transition, must exceed all atomic decoherence rates in the system. This requirement to obtain superradiance dictated most of the design choices in the experiment.

For superradiance experiments operating deep in the "bad-cavity" regime (where the cavity is much more lossy than the atoms), the rate of collective interactions is given by $NC\gamma$, where N is number of atoms coupled to the cavity, C is the single-atom cavity cooperativity parameter, and γ is the excited state lifetime for that transition. In order to achieve superradiant pulses, the collectively enhanced emission rate from the atoms must be made larger than atomic decoherence rates. Because the natural decay rate of the transition is so slow, this represents a stringent requirement for this system.

Atomic decoherence, or a decay of the atomic coherence at a rate γ_D, has the effect of setting a threshold atom number N_t below which a superradiant pulse will not occur without seeding of

coherence. For homogeneously coupled atoms, the requirement for superradiance is $NC\gamma/2 > \gamma_D$, which sets a threshold atom number $N_t = 2\gamma_D/(C\gamma)$. For atom numbers above this threshold value, N atoms radiating in the presence of decoherence produce a pulse identical to the pulse that the number of excess atoms, $N_x = N - N_t$, would produce without decoherence.

For a given atomic transition, γ is fixed. Thus if we want the collective emission rate to be large, we have three requirements: a high-cooperativity cavity, many atoms, and low decoherence.

In this work, we use a high finesse optical ring cavity. Unlike a 2 mirror cavity, a ring cavity supports a travelling wave mode, which we use to transport atoms from the lattice loading region to a "quieter" region of the cavity. The design, assembly, and characteristics of the cavity are detailed in Sec. 2.5. In practice, achieving a high-cooperativity cavity is simpler than a high atom flux or low dephasing, so much of this work focuses on the latter two requirements.

How many atoms do we need for continuous wave superradiance? As mentioned above, because the rate of collective emission into the cavity scales with atom number, dephasing sets a minimum, or threshold, atom number in order to enable superradiance. In the pulsed superradiant system, our threshold atom number for the mHz transition was $3.3(8) \times 10^4$ ^{87}Sr atoms [66]. To maintain steady-state superradiance, we need to maintain steady-state inversion. This means we would need to supply at least the threshold number of fresh atoms in the excited state before the existing atoms decay to the ground state. The timescale for atoms to decay to the ground state is set by the superradiant pulse length $\sim 1/(NC\gamma)$, which was around 100 ms in our pulsed demonstration of superradiance on the mHz linewidth transition. Compared to the pulsed experiment's single atom cooperativity of $C_{pulsed} = 0.41$, the continuous apparatus has a single atom cooperativity of $C = 0.16(1)$ for atoms interacting with a single directional mode of the ring cavity. If we assume the continuous experimental apparatus will have the same atomic decoherence as the pulsed apparatus, for a characteristic pulse length of 100 ms and a relative cooperativity between the experiments of $C_{pulsed}/C \sim 2.5$, this sets a minimum flux of 8.5×10^5 ^{87}Sr atoms per second.

In this work, we use the 12 times more isotopically-abundant ^{88}Sr. In addition to providing more atoms, this isotope is bosonic and has no nuclear spin, which simplifies the electronic structure.

However, in order to demonstrate an atomic source consistent with superradiance on the mHz transition in ^{87}Sr, this means we need a greater flux of ^{88}Sr atoms. Additionally the capture fraction from the blue MOT into the lattice is about a factor of 2 lower for ^{87}Sr [61]. Thus to be above threshold for lasing, assuming the same transverse decoherence rate as the pulsed experiment, we need a flux of at least 2×10^7 ^{88}Sr atoms per second loaded into the lattice. We are within error bars of this flux, with $1.9(3) \times 10^7$ ^{88}S atoms per second continuously loaded into the ring cavity in the strong collective atom-cavity coupling regime! See Sec. 2.6.4 for more details.

The final component needed to achieve lasing is to minimize atomic dephasing. Achieving a low enough decoherence rate involves removing any factors that would cause a scrambling of the relative phase between the superposition states of the different atoms. To suppress atomic decoherence, we rely on techniques used to provide long coherence times in optical lattice clocks [102, 103], as well as new techniques to provide a compact source with minimal dephasing near the cavity mode. By using an ultra-high vacuum environment, we eliminate collisions with background gas molecules. By laser cooling and confining the atoms along the cavity axis with an optical lattice, we eliminate first-order Doppler shifts in the direction of emission without imposing large shifts to the lasing transition frequency.

Unlike a traditional atomic physics experiment that operates in a pulsed manner and can turn any inhomogeneous electric or magnetic fields off, we need to be additionally careful to separate the cavity region from "noisy" inhomogeneous electric and magnetic fields which may decohere or collapse the atomic wavefunctions. To ensure low inhomogeneous broadening in the cavity mode due to Zeeman shifts, we do not load from a red 3D MOT into the lattice, rather we physically separate the inhomogeneous magnetic fields of the MOTs from the cavity mode and load from a red 3D molasses into the lattice (see Sec. 2.4 for more detail). To ensure minimal blue scattered light in the cavity region, we coated much of the chamber with a low-reflectivity black coating and inserted a baffle with a small aperture between the blue 2D MOT region and the cavity (see Sec. 2.2.1 for more detail).

These three requirements of a high-cooperativity cavity, a high continuous flux of atoms,

and low decoherence will continue to be a theme throughout this chapter, as they provide the key constraints for the experimental design and implementation.

2.2 Vacuum System

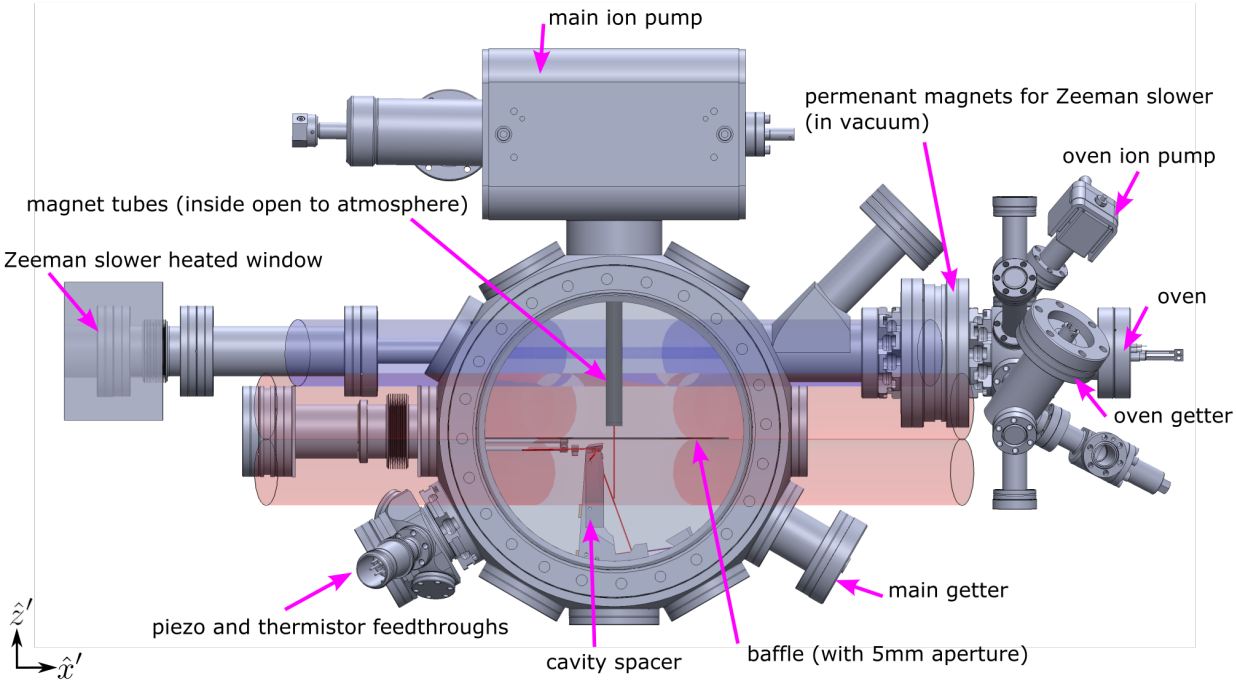

Figure 2.1: The vacuum system consists of one main chamber and a few appendages. The science chamber, which contains the optical cavity, has two main 10 in viewports to provide good optical access. On the right hand side, there is the atom source, which contains an oven and permanent magnet Zeeman slower. The left hand side has a heated window for the Zeeman slower and the mounting hardware for the baffle. Finally, the top has a pumping appendage with a 45 liter/second ion pump and right angle valve to connect a pump station.

A system producing a continuous flux of cold atoms requires a fundamentally different approach than an apparatus that operates in a pulsed manner. Often in a pulsed experiment, once the atoms reach the "science" chamber, the atoms stay in approximately the same location and beams are turned on/off in a time-sequence to address the atoms. In contrast, a continuous supply of atoms requires separating the sequence in space.

With the ultimate long-term goal of creating a metrologically useful, transportable, mHz

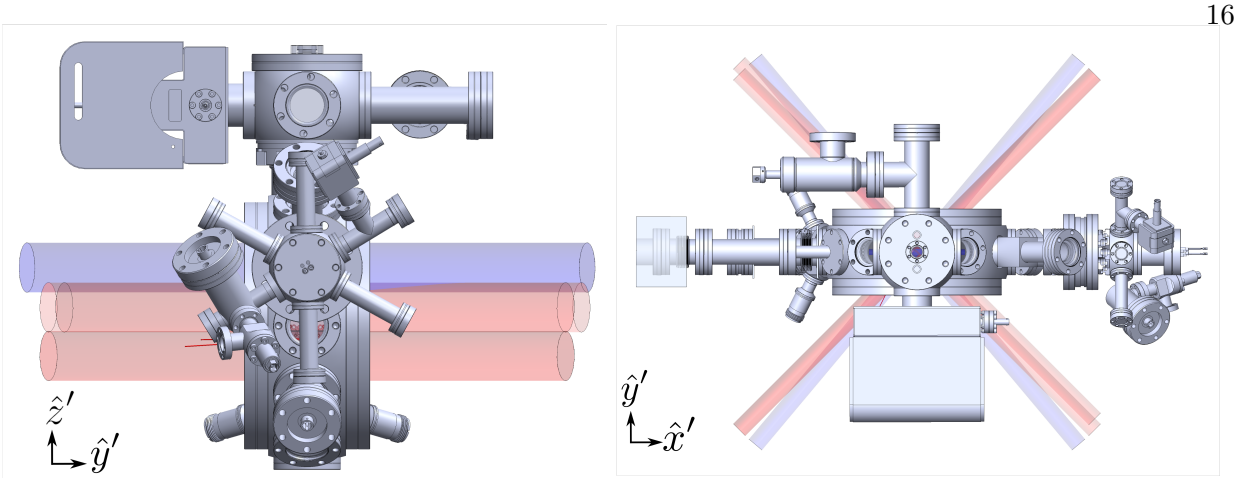

Figure 2.2: Side (left) and top (right) views of the vacuum system apparatus. From the side, one can see the 6 mini nipples mounted just after the output of the oven. These give optical access to measure the flux out of the oven and allow for the possibility of a transverse cooling stage or the creation of a steady-state superradiant laser based on a hot thermal beam. From the top, one can see the main ion pump and right angle valve, the principal pumping components of the main chamber. If we focus on the 4.5 in to mini conflat reducer flange in the center of the image, above and below the mini viewport are two holes reminiscent of a panda fiber. These holes are open to the atmosphere and are the inside of the magnet tubes that extend into the main chamber.

linewidth superradiant laser, we chose to create a compact design based on a single main chamber. Including all appendages, the vacuum system measures about 3 feet by 1.5 feet and could be made smaller if desired. This choice to make a compact system also eliminates the need for transfer between chambers, which adds complexity.

Fig. 2.1 shows an overview of the vacuum system. To maximize future flexibility and be able to continuously address the atoms between the blue 2D MOT and the cavity mode, we opted for great optical access. The main chamber is a custom 10 in spherical dodecagon vacuum chamber from Kimball Physics. The two custom features on this chamber are a welded 4.5 in conflat flange on the top to increase conductance and a y-join on the right to connect to the oven apparatus and also allow optical access. With the exception of the port labeled main getter, all other sides of the dodecagon have optical access to the main chamber. The primary optical access to the chamber is through the two 10 in viewports, which are anti-reflective coated for angles of incidence from 0 to 45 degrees. This allows the main cooling beams to enter close to 45 degrees angle of incidence, as

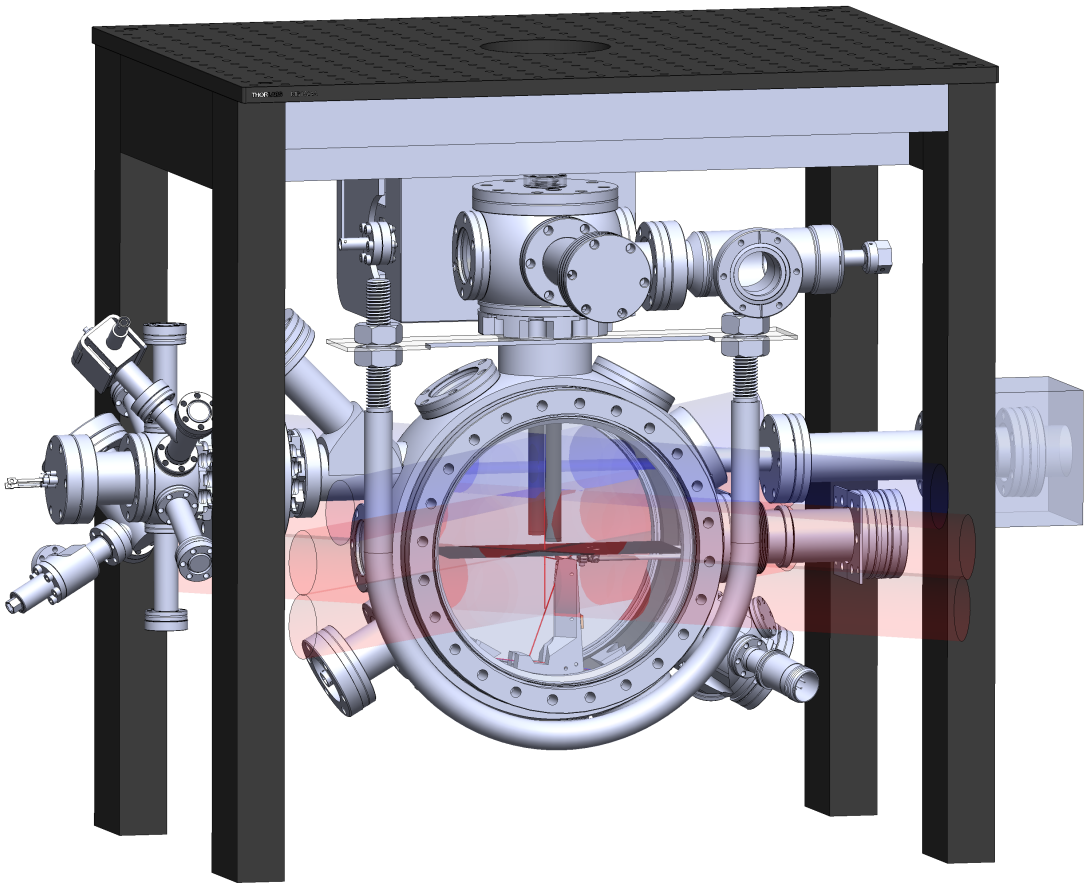

Figure 2.3: Mounting apparatus and back view of vacuum system. The vacuum chamber is supported from the top by an aluminum 80/20 structure. Rubber between the 80/20 structure and the optical table dampens vibrations and the stiffness of the aluminum pushes vibrations to higher frequencies. The main mounting point is a u-bolt around the main chamber flange that connects to the structure above. Additional mounts support the main ion pump from above and the oven assembly from below (not depicted).

shown in Fig. 2.2 on the right side.

Pumping for the main chamber is provided by a 45 litre/second ion pump mounted on the top of the chamber and a Saes D200 getter mounted on the bottom right hand side. The oven has an additional 3 litre/second ion pump and a getter. Parts of the chamber were pre-baked, but the entire assembled system was not baked, as the maximum possible temperature for baking is limited by the glass point of torrseal at 120 C. Moreover, the number and size of viewports present

a difficulty in heating evenly and strontium is highly reactive, so the strontium coating that forms inside the chamber serves as an excellent pump. There is no differential pumping stage between the oven and the main chamber, so when the oven is operated at full temperature, it adds a significant load to the chamber. As measured by the main ion pump, with the oven at 475 C (100 C) the pressure is 2.3×10^{-9} Torr (5.2×10^{-10} Torr). We think the vacuum at the cavity is a factor of 2-3 higher in pressure than at the main ion pump, as the pumping speed of the ion pump is limited by both the conductance to the main chamber and the conductance around the baffle. Our estimated vacuum pressure at the cavity mode of $\sim 7 \times 10^{-9}$ Torr gives a vacuum-limited atomic lifetime of 300 ms [104].

The baffle appendage is described further in Sec. 2.2.1, the Zeeman slower and atomic source appendages in Sec. 2.3, and the magnet tubes in Sec. 2.4.

2.2.1 Scattering Mitigation

To ensure minimal blue scattered light in the cavity region, we inserted a baffle with a small aperture in between the blue 2D MOT region and the cavity and coated much of the chamber with a low-reflectivity black coating.

The baffle between the red 2D MOT and 2D molasses has an aperture of 5 mm. It is mounted on rods that are connected to groove-grabbers that are in turn mounted onto a flange on the baffle appendage (shown in Fig. 2.4). There are two sets of plates mounted on either side of the bellows on the baffle appendage. By changing the separation between the plates, we can move the position of the baffle (and thus the aperture) within the main chamber. The idea behind the baffle is to eliminate the direct line of sight between the blue 2D MOT and the quiet region of the cavity mode (where atoms are transported after being loaded in the travelling lattice). The position of the aperture is adjustable from the outside of the vacuum chamber to allow more flexibility in the experiment.

To limit the number of stray photons in the cavity region, the interior of the vacuum chamber is painted with Alion MH-2200, a solar-absorbing, low out-gassing black paint. All paint was applied

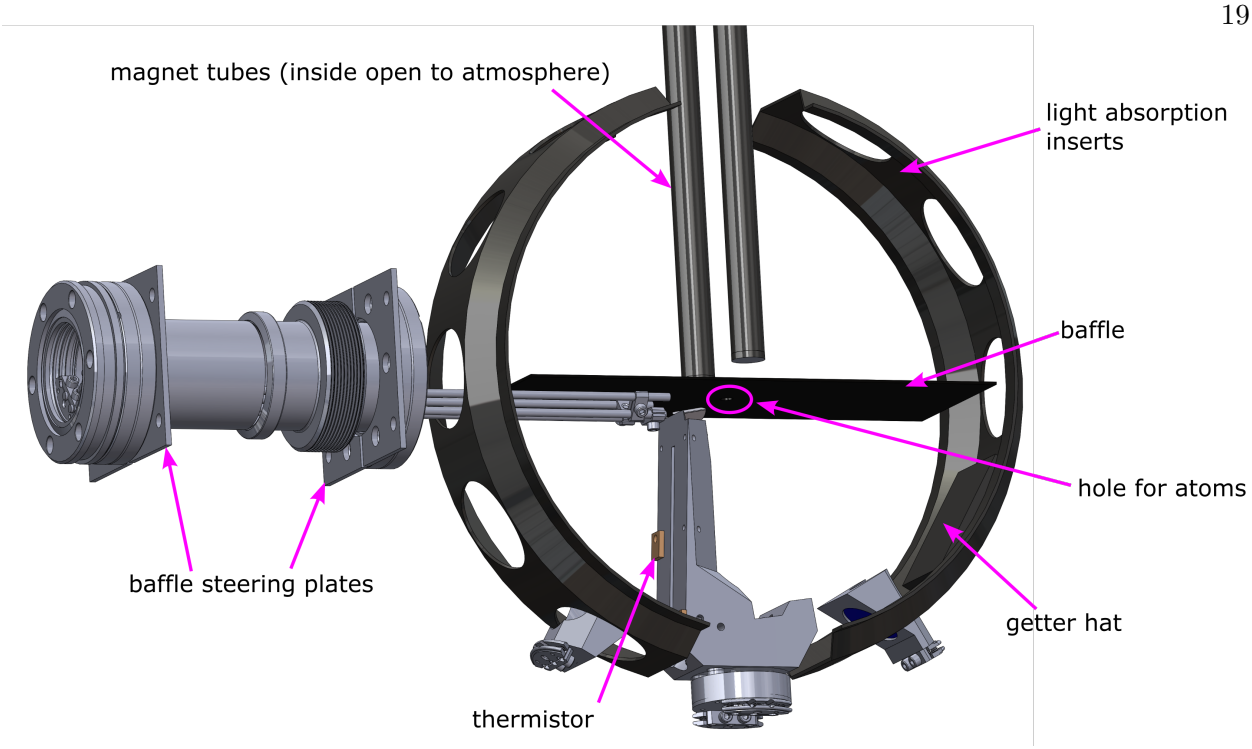

Figure 2.4: Scattering mitigation in the main chamber. This figure highlights the objects inside the main chamber that are designed to absorb optical scattering. The horizontal black baffle in the center separates the blue 2D MOT region from the cavity region and has a 5 mm aperture to allow the atoms to transit between regions. It is mounted to the conflat flange on the left side of the nipple via 6 mm steel rods. The position of the baffle is adjustable outside of the vacuum chamber by changing the separation between the two sets of plates mounted on either sides of the edge-welded bellows (with threaded metal rods, not depicted). Also shown are the black-paint coated magnet tubes, cavity spacer, getter hat, and aluminum inserts. The getter hat is an aluminum shield to protect the high finesse cavity mirrors when activating the getter and can be seen blocking the lower right dodecagon viewport hole. The two aluminum inserts are shaped to fit inside the main chamber and combine with the baffle to provide the main scatter prevention. This image also shows the mounting hardware that affixes the cavity spacer mount and two folding mirrors to the main chamber via groove grabbers.

using an airbrush with Nitrogen gas. A paper from 1985 measured the outgassing of this paint as 8.6×10^{-11} Torr liter/second cm^2 after a 24 hour vacuum bake at 100 C [105]. I wanted to double-check this outgassing rate, so I made 4 concentric cylinders that fit inside a 2.75 in conflat tee out of Aluminum 5052. I measured the outgassing rate after pre-baking in an annealing oven at 260 C for 24 h and then baking the vacuum chamber (in this case, a conflat flange tee) around 250 C for 40 h. After getting to rough vacuum and turning on a 55 litre/second ion pump, the

test setup quickly pumped down and started to flatten out after 3 days at 3.5×10^{-9} Torr (8 days at 2.5×10^{-9} Torr) as measured by the ion pump. From this pressure, the pump speed of the ion pump, and the painted surface area (890 cm^2), I extracted an outgassing rate of 1.5×10^{10} Torr liter/sec cm^2. This value assumes that the outgassing of the paint was dominant over other effects such as a leak rate or outgassing from the steel tee, so it seems reasonable that it is within 50 % of the previously measured value.

After testing the outgassing of the paint, we decided to use it in the main experiment, but coat individual pieces rather than directly coating the inside of the main chamber in case we needed to remove the paint in the future. We coated all the parts that live in the main chamber, including the magnet tubes, baffle, cavity spacer, getter hat, and aluminum inserts. The getter hat is an aluminum shield to protect the high finesse cavity mirrors when activating the getter. It can be seen blocking the lower right insert hole in Fig. 2.4). The two aluminum inserts are shaped to fit inside the main chamber and combine with the baffle to provide the main scatter prevention.

2.3 Atomic Source

We used a third generation strontium atomic source provided by AOSense, Inc. This source consists of an oven that provides a collimated beam of hot strontium atoms and a permanent-magnet Zeeman slower in vacuum. On the pulsed experiment, we observed the development of a strontium "volcano" on the heat shield of the Zeeman slower that eventually connected to and caused a thermal short to the outer heat shield of the oven. To eliminate this issue, we inserted a small Kimball Physics chamber as a spacer between the oven and Zeeman magnets, which separated the two heat shields by 2 in, almost a factor of 10 greater than the separation in the previous generation.

To provide optical access to the thermal beam of atoms between the oven and Zeeman slower, there are six viewports mounted in a hexagonal pattern at the output of the oven (shown in Fig. 2.2). They give optical access to measure the flux of atoms out of the oven and allow for the possibility of a transverse cooling stage or the creation of a steady-state superradiant laser based on a hot thermal beam. They are mounted on nipples to prevent them from being coated in strontium, but

after about 2.5 years of operation, the viewports have started to accumulate a strontium coating.

The other component of the atomic source is a home-built heated sapphire window through which the optical Zeeman slower beam enters the vacuum chamber. It must be heated to prevent the thermal beam of strontium atoms from sticking to the viewport and creating a mirror-like surface. The window is heated to 350 C by a heater ring around the viewport flange (outside of vacuum) and is thermally separated from the main chamber by a set of edge-welded bellows. Further operating details of the atomic source are given in Section 2.6.2.

2.4 Magnetic Fields

In a continuous experiment, we rely on a spatial sequence rather than a time-sequence to cool and address the atoms. This means our magneto-optical traps (MOTs) and associated magnetic fields need to be on continuously. This simplifies our magnetic field production in one sense, as we can use permanent magnets rather than quickly switching coils, but complicates it in another, as we need the magnetic field gradient to be small by the time the atoms reach the cavity mode.

We chose to use permanent magnets close to the atoms. To allow flexibility to switch out magnets or add shims or coils in the future, we decided to create magnet tubes that extend into the vacuum chamber and are open to the atmosphere on the inside. The magnet tubes can be seen in the main chamber in Figs. 2.4 and 2.3. They are welded onto a 4.5 in reducer flange on the very top of the experiment, as seen in Fig. 2.2. In this image, above and below the mini viewport are two holes reminiscent of a panda fiber. These holes are open to the atmosphere and comprise the inside of the magnet tubes that extend into the main chamber.

The axes of the magnet tube cylinders are separated by 2 in, to be as close as possible while allowing a 1 in wide beam oriented at 45 degrees (with respect to the plane between the cylinder axes) to pass between them. Each tube contains one neodynium 40 magnet with dimensions $1.590 \times 3/16 \times 1/8$ in (magnetized through the 3/6 in dimension, model Rect1400 from supermagnetman). The magnets are oriented as shown in Fig. 2.5. This magnet configuration produces a quadrupole field in the horizontal plane and a magnetic field zero along the center line between the magnets.

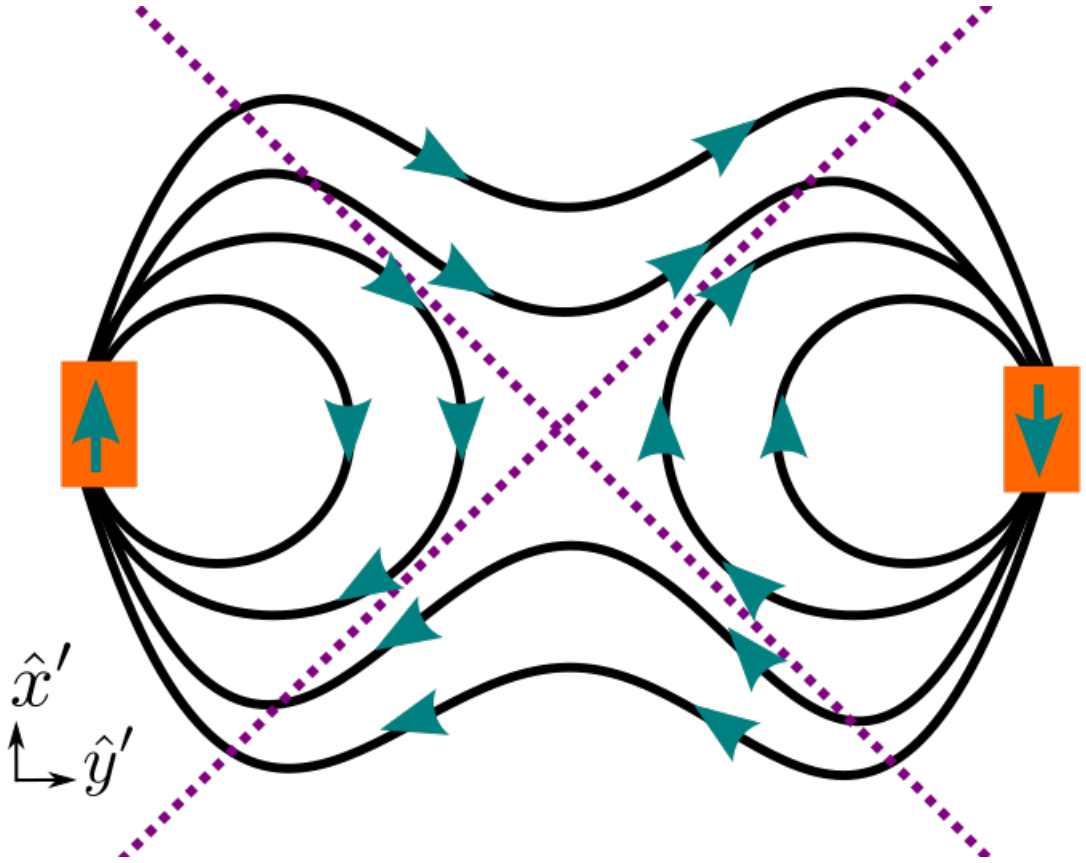

Figure 2.5: Representation of the 2D magnetic quadrupole field from our two permanent magnets (orange rectangles). Black lines represent magnetic field lines and teal arrows show the direction of the magnetic field. This magnet configuration produces a quadrupole field along the purple dotted axes and a magnetic field zero where the dotted lines intersect. This image shows a horizontal cross section through the magnets, which extend out of the plane.

The magnets are each mounted on aluminum L-angle stock. Both aluminum angles are connected at the top to an 80/20 bar, which is mounted to an XY translation mount to control the position of the quadrupole field.

The permanent magnets are centered vertically on the blue 2D MOT and produce a magnetic field gradient along the quadrupole axes of 50 Gauss/cm. Below the magnets, the gradient of the quadrupole field decreases and is about 5 Gauss/cm in the center of the red 2D MOT, appropriate for operation on the 7.5 kHz linewidth transition. Thus with one pair of permanent magnets, we produce a magnetic field suitable for both the red and blue 2D MOT stages.

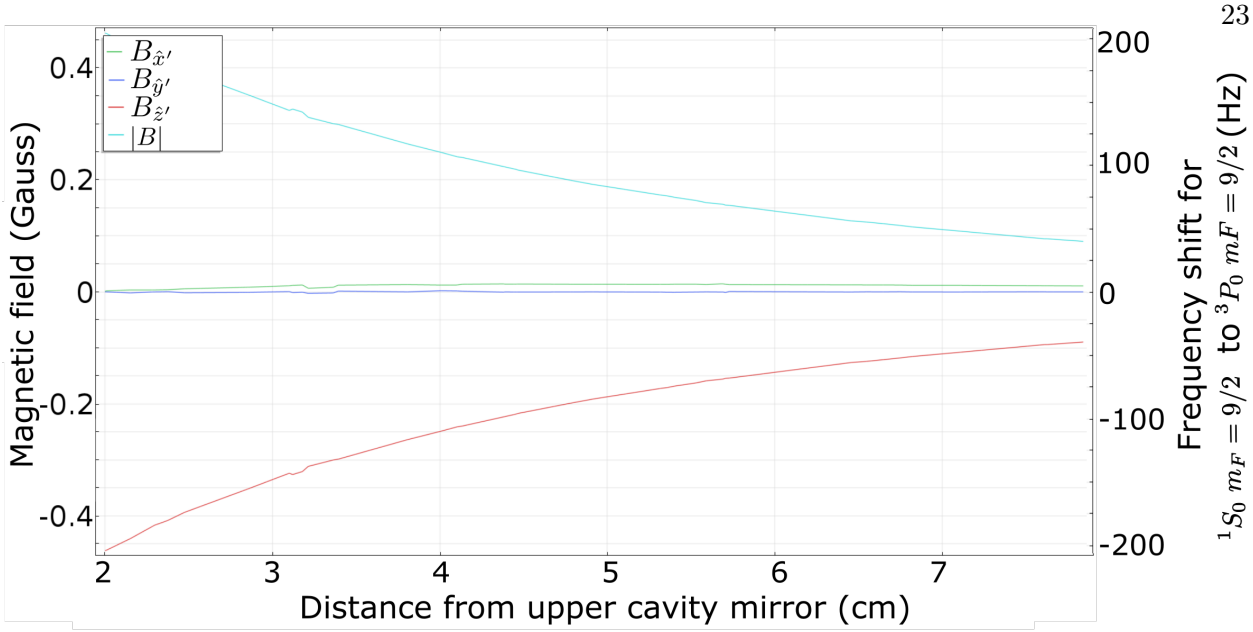

Figure 2.6: Simulated magnetic field inhomogeneity along the cavity mode from the MOT permanent magnets and corresponding Zeeman shift for the ${}^1S_0, m_F = 9/2$ to ${}^3P_0, m_F = 9/2$ transition. The majority of the magnetic field points straight down (along $-\hat{z}'$). Atoms are loaded into the cavity $\sim$ 2 cm from the upper cavity mirror. If we transport the atoms 2 cm down the cavity mode to a "quieter" lasing region and the atoms move 5 mm while participating in superradiance, they would experience a differential magnetic field between the start and end of the superradiant emission of about 25 mGauss. This corresponds to an 11 Hz differential shift on the $m_F = 9/2$ state of the clock transition.

The last question to address with the magnetic fields is the inhomogeneity of the magnetic field at the cavity mode, which would produce inhomogeneous Zeeman shifts on the clock transition. Fig. 2.6 shows the magnetic field inhomogeneity along the cavity mode from the MOT permanent magnets. If we transport the atoms 2 cm down the cavity mode before they participate in superradiance and they move 5 mm while participating in superradiance, they would experience a differential magnetic field between the start and end of the superradiant emission of about 25 mGauss. This is an 11 Hz differential shift on the $\mathrm{m}_F = 9/2$ state of the clock transition, which is about 3 times larger than the 3.5 Hz decoherence rate observed in the pulsed demonstration of mHz superradiance [66]. To reduce this inhomogeneous broadening, we may have to either transport the lattice slower so that atoms are spread over a smaller distance during their participation

in superradiance or add shim magnets or coils to reduce the magnetic field gradient. I suspect that before investing effort into minimizing the inhomogeneous field from the MOT magnets, it will be worth checking the magnetic field inhomogeneities from other sources near the atoms, such as the magnets on the ion pump or the nominally nonmagnetic optical table.

2.5 The Ring Cavity

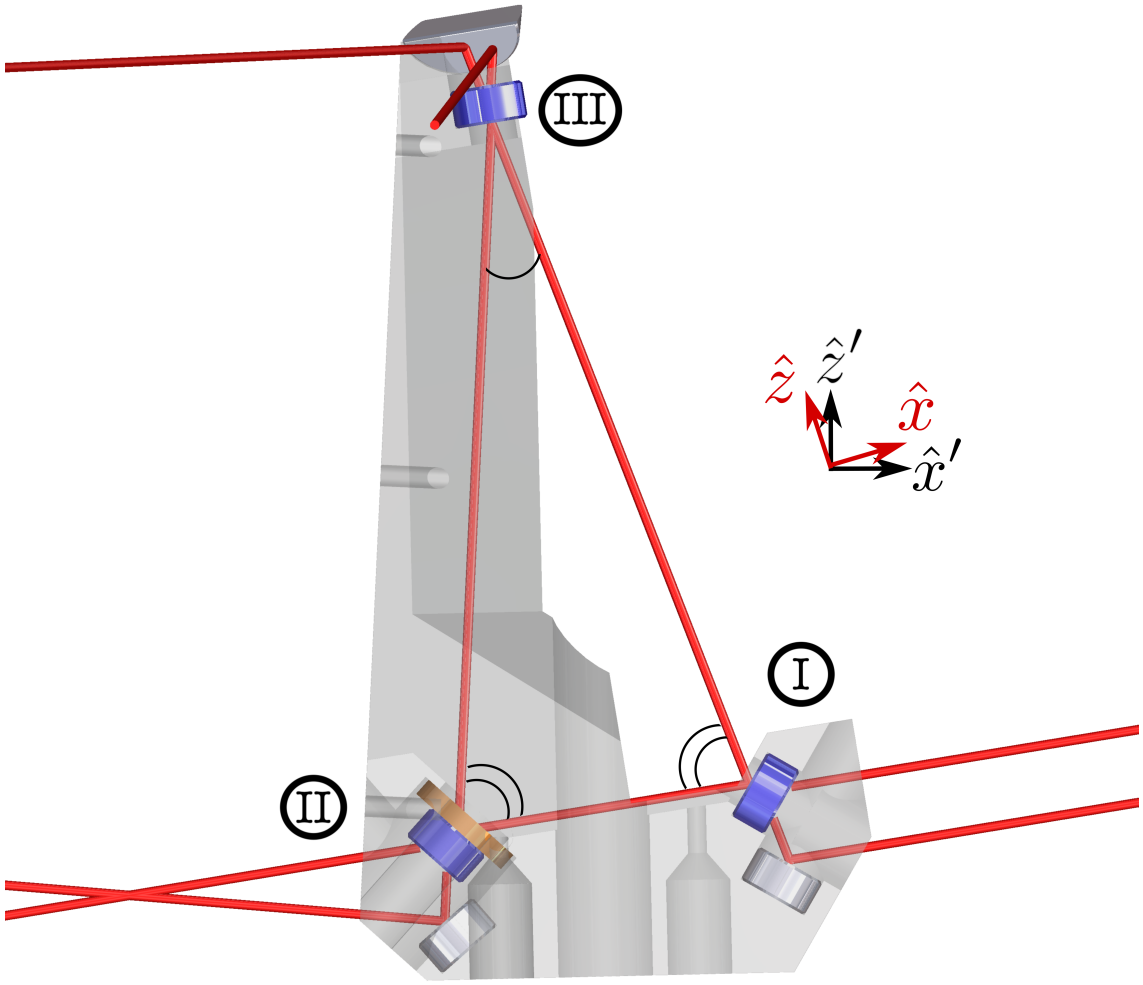

Figure 2.7: Representation of the cavity spacer (transparent grey) and light coupled into the cavity (red, not to scale). The three blue mirrors labeled I, II, and III are the primary mirrors of the cavity and the three silver mirrors are secondary mirrors to direct the light after it exits the cavity. The piezo is shown in orange.

To increase the collectively enhanced atomic decay rate, we trap the atoms within a high finesse optical cavity (Fig. 2.7), effectively increasing the optical depth of the atomic ensemble. The optical cavity consists of three highly reflective mirrors that light bounces back and forth between many times. The cavity provides distinct resonant optical modes, defined by their spatial profile and frequency, with which the atoms can interact through the exchange of photons. Section 2.5.1 describes the design and geometry of the cavity, Sec. 2.5.2 the design of the cavity spacer, Sec. 2.5.4 tuning the length of the cavity, Sec. 2.5.4 the construction and assembly of the cavity, and Sec. 2.5.5 the cavity performance.

2.5.1 Cavity Design

Why a three mirror cavity? A two mirror cavity allows only standing wave modes, whereas a ring (3+ mirror) cavity allows travelling wave modes, which we use to create a travelling lattice supported by the cavity. A ring cavity has several features (read: complications) compared to a two mirror cavity.

Mirrors often have different reflectivities for s (out of plane) and p (in plane) polarization, which leads to a different finesse for the each polarization. Mirrors also often impart a different phase shift for s (ϕ_s) and p (ϕ_p) reflections due to differential penetration depths, which splits the s and p modes in frequency. This splitting (in Hz) is given by:

$$\Delta f_{sp} = FSR\left[\frac{(\phi_{s1}+\phi_{s2}+\phi_{s3})-(\phi_{p1}+\phi_{p2}+\phi_{p3})}{2\pi}\right] \tag{2.1}$$

where ϕ_{si} and ϕ_{pi} are the s and p phase shifts from mirror i and FSR is the free spectral range of the cavity. For our cavity, I view both the different finesse of the s and p polarizations and the frequency splitting between the s and p cavity resonances as features, as the s and p polarization states are very well defined with respect to our cavity and we make use of the splitting between the s and p modes to simultaneously stabilize and probe the cavity.

For a cavity with more than 3 mirrors, if one mirror is slightly out of the plane defined by the other three mirrors, this leads to a rotation of the polarization in one round trip. This gives

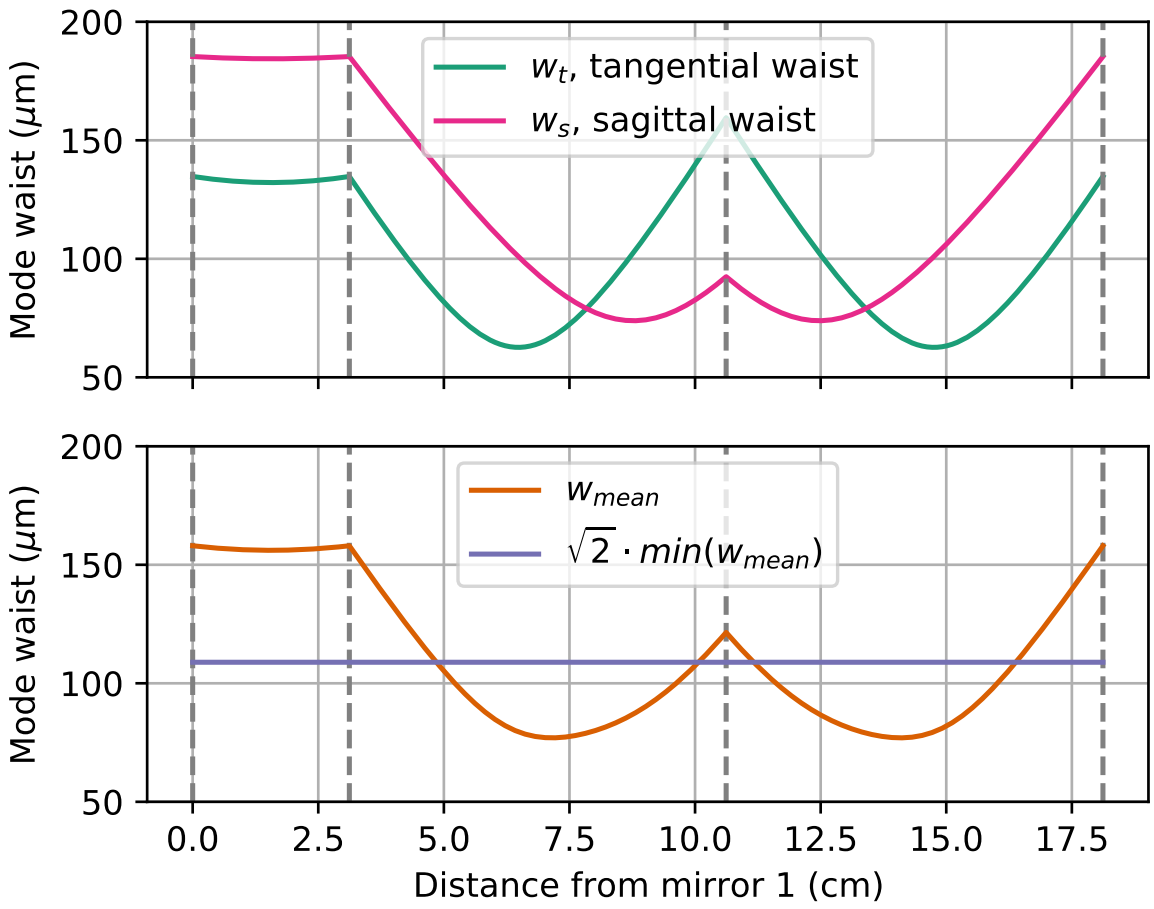

Figure 2.8: The mode waists versus position along the cavity for 698 nm light. The sagittal, w_s and tangential, w_t mode waists are offset in position in order to create a large region of the cavity over which the geometric mean of the mode waists, $w_{mean} = \sqrt{w_s \cdot w_t}$ changes by less than a factor of $\sqrt{2}$. The x-axis is the distance from mirror I, going in the direction I, II, III and the position of the mirrors are depicted by grey dashed lines. For our cavity, the main cavity arm has a 5 cm section over which w_{mean} changes by less than $\sqrt{2}$.

a splitting of the σ^+ and σ^- modes of the cavity, which scales like the rotation angle times the free spectral range. In addition to the added complexity of more mirrors, the possible polarization rotation from a cavity with more than three mirrors was undesirable for us, so we stuck with a three mirror cavity.

After having chosen to go with a three mirror cavity, we needed to pick the lengths of each cavity leg and the radii of curvature of the mirrors. Together, these must create a stable cavity

mode. One of our overarching design goals was to create a cavity with a high single atom cavity cooperativity, C. C is set by the cavity waist w, wavevector k, and finesse F and can be expressed for homogeneously coupled atoms in a standing wave cavity as [106]:

$$C_{standing} = \frac{24F}{\pi k^2 w^2} \tag{2.2}$$

For a two mirror cavity, the modes are standing wave in nature, where the light propagating in one direction, say to the left, interferes with the light propagating in the opposite direction, say to the right. If atoms emit electric field E_L into the cavity mode propagating to the left and E_R propagating to the right, the total field in the cavity is $E_L + E_R = 2E_L$. For a ring cavity, the modes are running wave in nature. Atoms can emit electric field E_{cw} into the clockwise cavity mode and E_{ccw} into the counter-clockwise propagating cavity mode, but if atoms are only on resonance with one of the cavity modes, say the ccw mode, the total field in the cavity is E_{ccw}. The cooperativity scales as $C \propto g^2 \propto E^2$, so the cooperativity for atoms in a ring cavity interacting with one directional cavity mode is 1/4 the cooperativity of a standing wave cavity:

$$C_{ccw} = C_{cw} = C_{standing}/4 = \frac{6F}{\pi k^2 w^2} \tag{2.3}$$

For the work in this thesis and for the future continuous superradiant laser, the atoms interact with a single directional mode of the ring cavity. For the rest of this thesis, when I refer to the cavity cooperativity in our experiment, I am referring to the cooperativity for atoms in a ring cavity interacting with one directional cavity mode, as per Eq. 2.3.

In order to have a high cooperativity, we need a high finesse F and small mode waist w. The angle of incidence at each mirror affects the reflection coefficient, which in turn sets the finesse. For a three mirror cavity with power reflection coefficients R_1, R_2, and R_3, in the limit where the mirrors are highly reflective, $(1 - R_i) \ll 1$, we can express the finesse as:

$$F = \pi \frac{\sqrt[4]{R_1 R_2 R_3}}{1 - \sqrt{R_1 R_2 R_3}} \tag{2.4}$$

For us, in order to reach a finesse around 40k, none of the mirrors could have an angle of incidence greater than around 50 degrees. We also wanted two mirrors with greater transmission

and one mirror with lower transmission, in order to allow for good coupling efficiency in one side and high quantum efficiency for detection out the other. This sets the requirement than one mirror have a lower angle of incidence than the other two mirrors. An additional desired design feature was to offset the sagittal, w_s and tangential, w_t mode waists in order to create a large region of the cavity over which the geometric mean of the mode waists, $w_{mean} = \sqrt{w_s \cdot w_t}$ changes by less than a factor of $\sqrt{2}$. The reason for this is so that characteristics such as the lattice depth, which scales like w_{mean}^2, do not vary much along the cavity mode.

Table 2.1: Geometry of our ring cavity. It is an isosceles triangle. The mirror labels can be found in Fig. 2.7.

mirror	angle of incidence (degrees)	mirror radius of curvature (cm)	cavity leg length (cm)
I	39	10	3.12 (d_{12}*)
II	39	10	7.50 (d_{23})
III	12	5	7.50 (d_{31})

*d_{12} is the distance between mirrors I and II

Table. 2.1 describes the geometry of our cavity, which satisfies all of the above criteria. We decided we had enough degrees of freedom elsewhere, so we chose to make the cavity an isosceles triangle for simplicity. Fig. 2.8 shows the tangential and sagittal mode waists, as well as w_{mean} for our cavity geometry. The main cavity arm has a 5 cm section over which w_{mean} changes by less than $\sqrt{2}$. The free spectral range of our cavity is $FSR = 1,650,740(20)$ kHz.

2.5.2 Cavity Spacer Design

In addition to supporting the cavity mirrors, the primary design criteria of the cavity spacer is to maximize optical access to the cavity mode, as shown in Fig. 2.9. The vertical arm of the cavity spacer is cut at 45 degrees, allowing access for the red 2D and 3D molasses beams to load atoms into the cavity mode. A slot through the back side of the spacer (seen in the middle image) and a 1 cm diameter hole through the bottom of the spacer (seen in the right image) allow access to the main arm of the cavity from all sides. Smaller diameter holes seen in the back and sides of

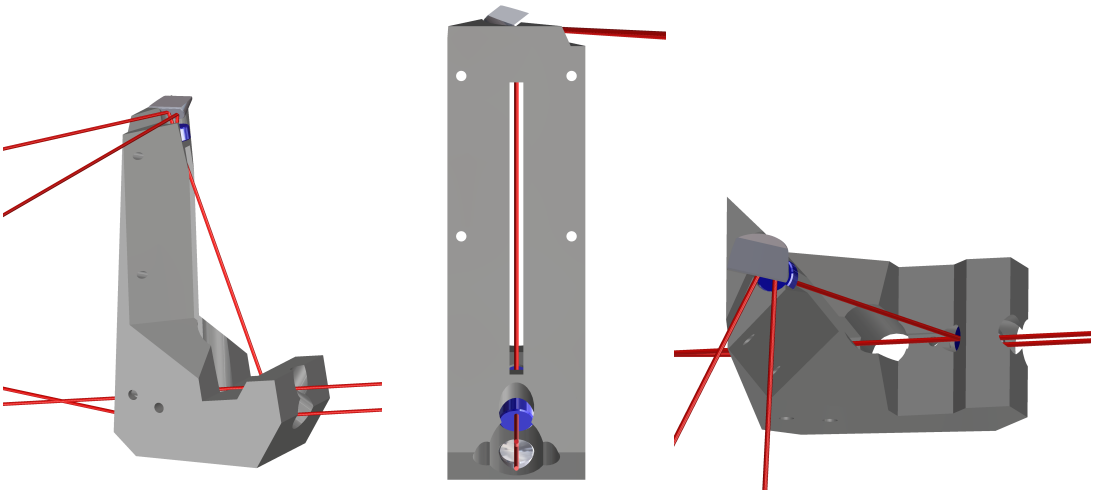

Figure 2.9: One primary design criteria of the cavity spacer is to maximize optical access to the cavity mode. The vertical arm of the cavity spacer is cut at 45 degrees, allowing access for the red 2D and 3D molasses beams to load atoms into the cavity mode. A slot through the back side of the spacer (seen in the middle image of this figure) and a 1 cm diameter hole through the bottom of the spacer (seen in the right image) allow access to the main arm of the cavity from all sides. Smaller diameter holes seen in the back and sides of the spacer allow for venting and to attach thermistors to the spacer.

the spacer allow for venting and to attach thermistors to the spacer.

The cavity mode is oriented such that the main arm of the cavity, between mirrors I and III, is 20 degrees from vertical. This angle is a compromise between wanting to minimize this angle so that atoms coming from above have to minimally change their trajectory to be loaded into a moving lattice and the geometrical problem of needing to get atoms around the upper cavity mirror.

In a traditional pulsed experiment, turning off magnetic fields produces eddy currents in anything that is electrically conductive, including a cavity spacer. We decided to use permanent magnets which are constant in time, so we had the option to use a conductive spacer. We chose aluminum because it is stiff (pushes vibrational modes to higher frequencies), easy to machine, vacuum compatible, and the electrical conductivity potentially mitigates patch charges on the surface.

Additionally, the cavity spacer is electrically insulated from the vacuum chamber. It sits on three viton (low-outgassing rubber) balls which in turn sit on three aluminum posts. The

rubber provides mechanical damping as well as electrical insulation. A kapton-coated copper wire connected to the cavity spacer offers the possibility to float the spacer to a voltage if desired. The geometry of the three post support was designed so that the center of mass motion of the cavity spacer is a side to side rocking motion in the $\hat{x}' - \hat{z}'$ plane, which should minimally affect the coupling to the cavity (to first order).

There are also three secondary mirrors mounted in the cavity spacer to direct the light after it exits the cavity, as shown in Fig. 2.7. The secondary mirror after mirror I was placed such that the two paths exiting the cavity through mirror I are parallel, to facilitate coupling into the cavity.

2.5.3 Tuning the Cavity Length

The round trip length of a cavity, ℓ determines the resonant optical modes. A cavity has a resonance whenever an integer number of wavelengths fit in the round trip length. The separation between the resonances in frequency is called the free spectral range, $FSR = c/\ell$, where c is the speed of light.

We would like to be able to make the cavity resonant with a given wavelength, which requires adjusting the round trip length of the cavity by up to half wavelength (or equivalently in frequency, half a free spectral range). We can change the cavity length by changing the voltage applied to a piezo, which makes it contract or expand. The piezo is affixed to the cavity spacer and the mirror is glued to the piezo, so when the piezo expands, the cavity length increases (see Fig. 2.7 for illustration).

The particular piezo we are using is a ring stack piezo with outer diameter 12 mm and inner diameter 6 mm (HPCh 150/12-6/2 from Piezomechanik). Applying a positive voltage increases the height of the piezo roughly linearly, with a maximum stroke of 2 μm when applying 150 V. For our wavelengths around 700 to 800 nm, this means we can change the cavity by three to four free spectral ranges.

If we want to make two frequencies resonant (or close to resonant) with the cavity at the same time, we must change the cavity length by many wavelengths. One might want to do this to

be able to interact with the kHz and mHz transitions simultaneously, or to center the piezo about 0 Volts if working with sensitive transitions such as Rydberg states. Changing the length of a cavity can also be accomplished by heating the cavity spacer, making use of the thermal coefficient of expansion. I painted the cavity with an optically-absorbing paint (which does double-duty as scattering prevention, see Sec. 2.2.1) to enable us to shine a powerful laser at the back of the cavity spacer and change the cavity length by many free spectral ranges. The vertical (back) arm of the cavity spacer was designed to be able to expand and minimally affect coupling into the cavity, as the angle of incidence on the top mirror is small. There are two thermistors mounted onto the back of the cavity spacer to enable a slow feedback to the temperature of the spacer. They are glued onto small copper plates which are attached to the cavity spacer via screws and are designed to be in good thermal contact with the spacer (the copper plates are shown in orange in Fig. 2.4).

2.5.4 Cavity Construction

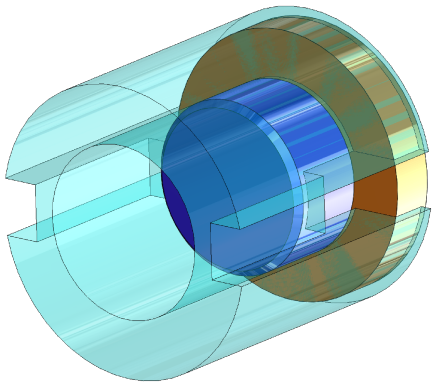

Figure 2.10: Centering jig to construct the cavity. The jig is depicted in transparent cyan, cavity mirror II in blue, and the piezo in orange. The jig allowed me to center and glue the mirror to the piezo. It was also instrumental in centering the piezo in the cavity spacer. The cutouts on the sides of the jig allow space for the piezo wires and access for gluing. The jig has a hole in the center to prevent contamination of the backside of the mirror.

To keep the high finesse mirrors clean, I assembled the cavity in a clean hood of a clean room. Mirrors I and III were designed to be a snug fit within their holes, so attachment proved to be

as simple as dropping them in, making sure they were properly seated, and using torrseal to glue them to the cavity spacer from the back side of the mirror. Mirror II was trickier, as it needed to be mounted centered on a piezo, which needed to be attached to the cavity spacer. I made a jig, as shown in Fig. 2.10, that allowed me to center and glue the mirror to the piezo. The exterior of the piezo jig was a snug fit into the cavity spacer, which centered the piezo in the cavity spacer and ensured all the mirrors would be aligned.

2.5.5 Cavity Performance

The cavity was designed to achieve a moderately high single atom cavity cooperativity parameter ($C \simeq 0.16(1)$) for s-polarized 689 nm and 698 nm light. This value was chosen with the goal of maximizing the collective cooperativity parameter NC within other technical constraints. Our s-polarized cavity linewidth at the ultra-narrow 1.35(3) mHz clock transition in ^{87}Sr [64] is 41 kHz, greatly exceeding the atomic linewidth and placing the system in a highly damped, "superradiant" regime. Additionally, we have p-polarized cavity modes that offer intermediate cavity cooperativity of $C \simeq 0.024(1)$ at 689 nm and 698 nm.

In addition to providing a mode with which the atoms interact via a narrow linewidth transition, the cavity also supports the lattice. The cavity has a lower (but still substantial) finesse at 813 nm to enable a deep lattice with moderate laser power. The cavity parameters are summarized in Table 2.2.

The cavity mirrors were coated by Five Nine Optics. The substrates are 7.75 mm in diameter, 4 mm thick, super polished, fused silica substrates from Research Electro Optics. We ordered two coating batches, one with transmission specifications of about 1 parts per million (ppm) at 689 and 698 nm and one with about 20 ppm at 689 and 698 nm (both at 10 degrees angle of incidence). Based on the transmission specifications and our measured cavity linewidths shown in Table 2.2, we estimate round trip losses of around 130 ppm. This is close to the pulsed experiment's losses of around 30 ppm per mirror, but greater than the estimated 10 ppm per mirror loss specified by the coating company.

Table 2.2: Specified cavity transmission, measured cavity finesse and linewidth, and calculated cavity coupling and cavity cooperativity for various wavelengths. The cooperativity is reported for atoms coupled to a single directional mode of the ring cavity, as in Eq. 2.3

Wavelength, Polarization	T1=T2 (ppm)	T3 (ppm)	Finesse $\times 10^3$	Cavity Linewidth $\kappa/(2\pi)$ (kHz)	Coupling $g/(2\pi)$	Cooperativity
698 nm, s	13	1.3	40(2)	41(3)	1.5(1) Hz	0.16(1)
689 nm, s	13	1.3	40(2)	41(3)	3.5(2) kHz	0.16(1)
689 nm, p	635	2.4	6.2(2)	266(7)	3.5(2) kHz	0.024(1)
813 nm, s	918	608	2.57(7)	645(17)		
461 nm, s	6.8×10^5	8.4×10^5	~ 0.001			

Much like other high finesse optical ring cavity experiments [107], we have observed coupling between the clockwise and counter-clockwise cavity modes. If we input light on resonance with the cavity in only one direction, we observe a small amount of light coming out the other direction. The fractional cross coupling in power is: $7(1) \times 10^{-2}$ for 689 nm s-polarization, $4.3(5) \times 10^{-3}$ for 689 nm p-polarization, and $5(4) \times 10^{-4}$ for 813 nm s-polarization, and appears to scale approximately with the cavity finesse.

2.6 Atomic Conveyor Belt: a High Flux Continuous Source of Cold Atoms

This section gives a summary of the process of creating a steady-state cold atomic beam. More specific information on each step of the process can be found in the following subsections.

Our conveyor-belt style system guides ^{88}Sr atoms through a series of spatially separated laser cooling and deceleration stages before loading them into a travelling wave optical lattice supported by the ring cavity, as shown in Fig. 2.11. We make use of two main optical cooling transitions: the dipole allowed 32 MHz linewidth "blue" transition between the ground state $^1S_0$ and the excited state $^1P_1$ and the intercombination "red" 7.6 kHz linewidth transition between the ground state and $^3P_1$, as shown in Fig. 2.12.

As in the pulsed experimental setup, atoms emerge from an AOSense oven and are slowed using a Zeeman slower. They are then captured into a vertically-oriented 2D blue MOT which has

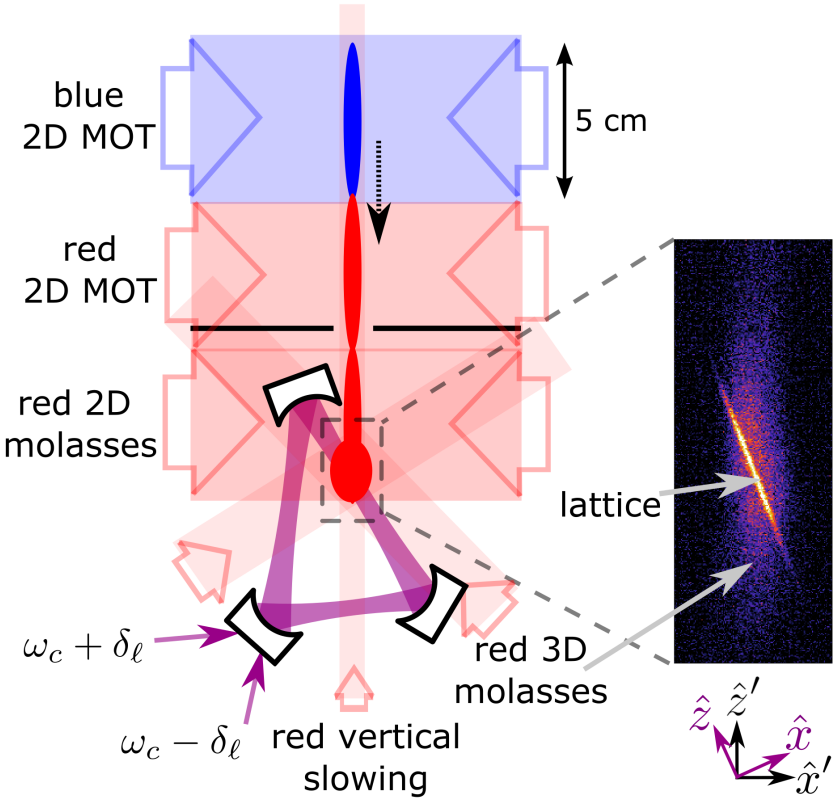

Figure 2.11: Experimental overview. Atoms are guided through a series of spatially separated laser cooling and deceleration stages before being captured into a red 3D molasses and loaded into a travelling wave optical lattice supported by the ring cavity. We make use of two main optical cooling transitions: the dipole allowed 32 MHz "blue" transition between the ground state $^1S_0$ and the excited state $^1P_1$ and the intercombination "red" 7.6 kHz transition between between the ground state and $^3P_1$. To form the optical lattice, light is injected into the cavity in the clockwise direction at frequency $(\omega_c - \delta_\ell)$ and the counterclockwise direction at $(\omega_c + \delta_\ell)$ to form a lattice travelling at $v = \lambda_\ell \delta_\ell/(2\pi)$, where ω_c is the cavity resonance frequency and λ_ℓ is the lattice wavelength. The inset depicts a single shot, 40 ms exposure image of red florescence from atoms in the red 3D molasses and lattice.

confining and cooling forces in the transverse directions and a zero of the quadrupole field in the vertical direction. Atoms move downwards from the blue 2D MOT into the red 2D MOT, where they are further cooled. From there, atoms move downward into the red 2D molasses and are finally captured into a red 3D molasses, from which they are loaded into the lattice. Note that vertical slowing is also necessary to bring the atoms within the capture velocity of the red 3D molasses.

2.6.1 Laser Cooling

In contrast to alkali atoms, the more complicated level structure of alkaline earth atoms, such as strontium, requires many more laser wavelengths. An energy level diagram with relevant states and transitions is shown in Fig. 2.12. Spin singlet states are shown on the left in the blue region, and spin triplet states are shown on the right in the orange region. Transitions between states of the same total spin (within the blue region, for example) can be dipole allowed and have decay rates of at least several MHz. On the other hand, transitions between singlet and triplet are dipole forbidden and decay much more slowly. Also depicted is the 57 kHz linewidth $^3P_2$ to $^3D_3$ transition at 2.9 μm, which was mentioned in Sec. 1.3 as a possibility for cooling during superradiance, as it avoids coupling directly to the mHz transition.

2.6.2 Initial Slowing and 461 nm 2D MOT

The path of atoms through the setup begins with a high-flux atomic beam source, which consists of an oven and a roughly 5 cm permanent magnet-based Zeeman slower operating on the broad-linewidth blue transition. The atoms begin at an initial temperature of 475 C inside the AOSense oven, then exit the oven through a nozzle consisting of an array of narrow capillaries that collimate the atoms into a narrow beam. A portion of the atomic beam is slowed in the Zeeman slower to roughly 50 m/s, within the capture velocity of our blue 2D MOT.

A blue 2D MOT is located approximately 25 cm after the exit of the Zeeman slower and has a non-confining axis oriented in the direction of gravity (see Fig. 2.11). This MOT has a loading rate of 1.1×10^{11} ^{88}Sr atoms/s and a characteristic loading time of 7.0 ms, with a steady-state

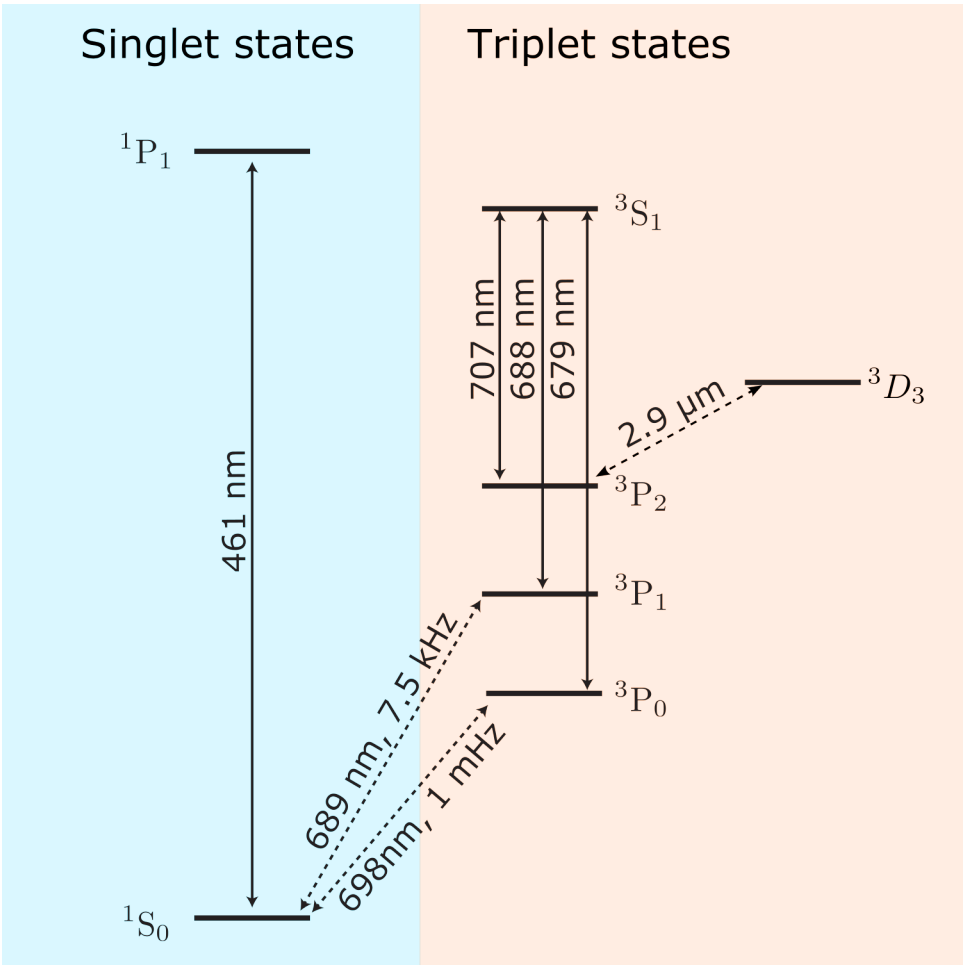

Figure 2.12: Relevant energy levels of strontium. Spin singlet states are shown on the left in the blue region, and spin triplet states are shown on the right in the orange region. Transitions between states of the same total spin (within the blue region, for example) can be dipole allowed and generally decay quickly, whereas transitions between singlet and triplet states (from blue to orange or vice-versa) are dipole forbidden and decay much more slowly. Note that the ^{3}P$_0$ to ^{1}S$_0$ transition is shown for ^{87}Sr. The presence of nuclear spin ($I = 9/2$ for ^{87}Sr) causes the ^{3}P$_0$ to ^{1}S$_0$ transition to become weakly allowed [108], whereas it is completely forbidden for ^{88}Sr, which lacks a nuclear spin.

population of 1.2×10^9 atoms (measured with fluorescence imaging).

While the $^1S_0$ to $^1P_1$ transition is close to a cycling transition, there is a small leakage channel from $^1P_1$ to $^1D_2$ with branching ratio $\sim 10^{-5}$. From $^1D_2$, atoms decay to $^3P_1$ and $^3P_2$. $^3P_1$ has an excited state lifetime of 21 μs, so atoms return relatively quickly from $^3P_1$ back to the ground state. However, atoms are stuck for a long time in the metastable $^3P_2$ state, where they do not interact

with the 461 nm cooling light. Eventually, population starts to build up in $^3P_2$, limiting a blue 3D MOT lifetime without re-pumping to tens of miliseconds. To increase the cooling efficiency and lifetime of our blue 2D MOT, we apply repump beams incident on the blue 2D MOT at 679 and 707 nm so that atoms in $^3P_2$ are pumped back to the ground state $^1S_0$.

The blue MOT beams are elliptical with dimensions roughly 5 cm tall by 2.5 cm wide, limited horizontally by the optical access afforded by the magnet tubes. The beams are retro-reflected after passing through the vacuum chamber, with typical power in a single pass around 23 mW.

2.6.3 689 nm 2D MOT, 2D Molasses, & 3D MOT

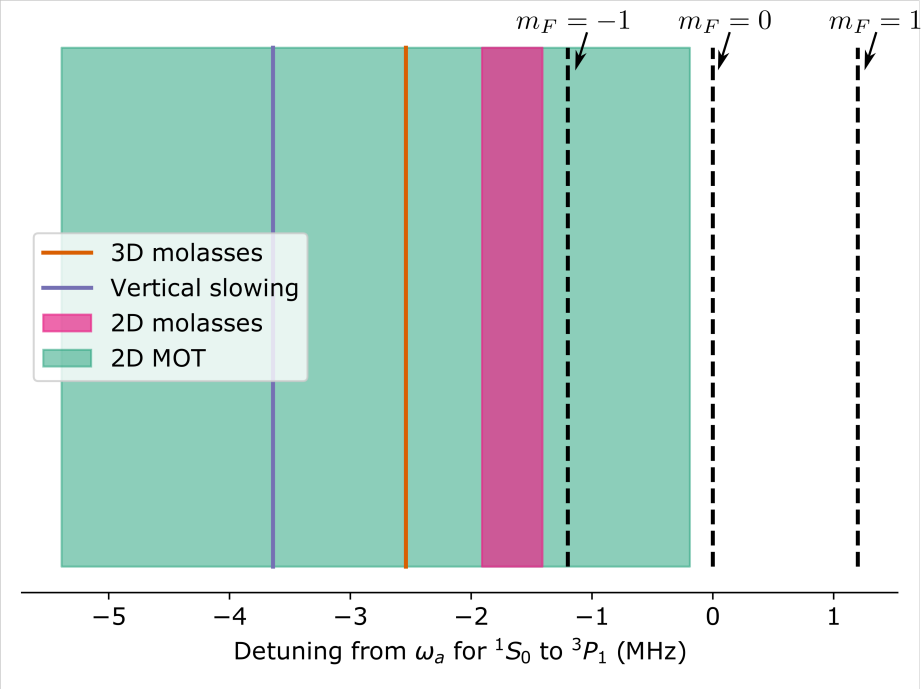

Figure 2.13: Typical frequencies of the red 2D MOT, 2D molasses, 3D molasses, and vertical slowing beams, relative to the $^1S_0$ to $^3P_1$ bare atomic transition frequency (where a negative detuning is red-detuned from the transition). The three Zeeman sublevels are shown as dashed black lines for the observed Zeeman splitting in the cavity region $f_{ZS} = 1.2$ MHz. The red 2D molasses and 2D MOT are operated in a SWAP configuration and the shaded region shows the frequency extent of the beams. The red 3D molasses and vertical slowing beams are fixed in frequency.

After being captured into the blue 2D MOT and cooled to a few milliKelvin in the transverse directions, the atoms make their way to the red 2D MOT. Further cooling is performed using the

"red" transition at 689 nm, which has a much narrower linewidth and is compatible with cooling to much lower temperatures. For the red 2D MOT and 2D molasses steps, we use a new form of cooling and trapping we developed, which we refer to as Sawtooth-Wave Adiabatic Passage (SWAP) cooling [60]. This technique has significant advantages over conventional laser cooling techniques and is described in Section 1.2.3.

Typical frequencies for the red MOT beams are shown in Fig. 2.13. The red 2D molasses and 2D MOT are operated in a SWAP configuration, and the shaded region shows the frequency extent of the beams, while the red 3D molasses and vertical slowing beams are fixed in frequency and have around a MHz Rabi frequency.

The red 2D MOT beams are elliptical with dimensions roughly 5 cm tall by 1 cm wide and the 2D red molasses beams are also elliptical, with dimensions roughly 5 cm tall by 5 mm wide. The red 2D MOT and molasses beams are oriented parallel to the table and address only the transverse atomic velocities. A vertical slowing beam described later in this section addresses the vertical velocity of the atoms.

The red 2D MOT, red 2D molasses, and vertical slowing beam all operate at a 50 % duty cycle, where the transverse beams are on when the vertical beam is off, and vice-versa. This is to ensure that the vertical slowing beam does not interfere with the adiabatic transfers of SWAP cooling. We implement this by turning on and off the RF signal sent to the red 2D molasses and red 2D MOT AOMs. The input to the red vertical slowing AOM is the 0^{th} order of the red 2D molasses AOM, so it receives more power when the red 2D molasses AOM is off and vice-versa. The beams are retro-reflected after passing through the vacuum chamber, with the typical power in a single pass of around 9 mW for the 2D MOT and 10 mW for the 2D molasses (powers reported when the beams are on).

Finally, atoms are loaded from the red 2D molasses into the red 3D molasses. For the red 3D molasses, two of the three beams are retro-reflected after passing through the vacuum chamber and the typical power in a single pass is around 9 mW. The radiation pressure of the red 3D molasses is balanced with the red 2D molasses, which is also incident on the atoms in the cavity mode. The

lifetime of atoms in the red 3D molasses is 260(20) ms, consistent with a vacuum limited lifetime, as discussed in Sec. 2.2.

The trickiest part of these stages was slowing the vertical velocity enough so that the atoms could be captured into a red 3D molasses, while maintaining a large atomic flux. The atoms have a nonzero transverse velocity, so if we slow the atoms too early, they will diverge horizontally and only a very small flux will make it to the red 3D molasses region. The atoms start with a large vertical velocity: upon exiting the bottom of the blue 2D MOT, atoms have a downward velocity of 6.8(1) m/s and a root-mean-squared velocity spread of 1.7(2) m/s (with vertical slowing beams off) and they fall accelerated by gravity into the red 2D MOT stage. This downward velocity is consistent with radiation pressure forces generated by scattering from atoms in the blue 2D MOT and is much too large to be captured into a red 3D molasses.

We slow the atoms with a red vertical slowing beam directed upwards, about 3.75 MHz red-detuned from the bare atomic transition. With this slowing beam, the downwards velocity of the atoms exiting the blue 2D MOT is reduced to 2.6(1) m/s. By the time the atoms reach the cavity mode, with the vertical slowing beam on (off) the atoms are moving downwards at 1.44(1) m/s (7.8(1) m/s) with a root-mean-squared velocity spread of 0.40(2) m/s (1.9(1) m/s). This velocity is within the capture velocity of our red 3D molasses!

2.6.4 The Optical Lattice

After being cooled to a temperature of order 10 μK, the strontium atoms are loaded into the conservative potential of an optical lattice with wavelength $\lambda_\ell = 813$ nm. We achieve a loading fraction from the red 3D molasses into the lattice of 9.7(5)% for a stationary lattice, as shown in Fig. 2.14. This was calculated as the number of atoms in the lattice divided by the sum of the number of atoms in the lattice and the red 3D molasses. We were pleased by this loading fraction, as it greatly exceeds the naive spatial overlap between the red 3D molasses and the lattice and is only a factor of 5 away from the loading fraction from a red 3D MOT to a lattice [61]. Furthermore, a relatively short lattice loading time of 69(9) ms ensures a high refresh rate of new atoms loaded

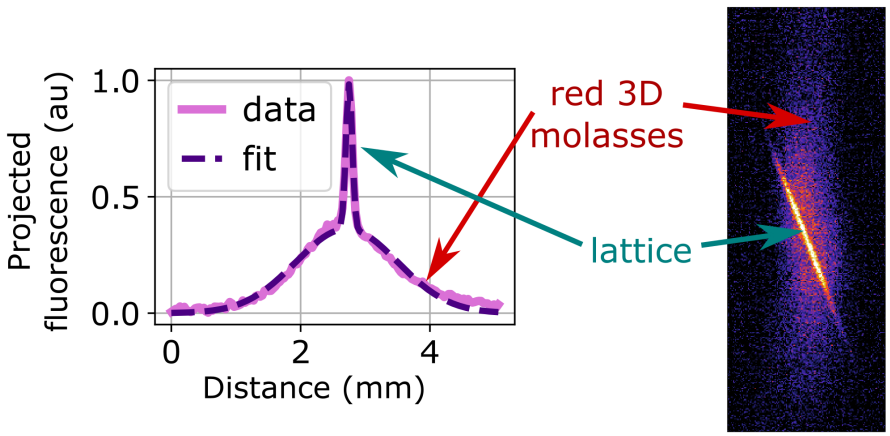

Figure 2.14: Loading from the red 3D molasses into the lattice. The image on the right is a single shot image with 40 ms exposure of red florescence from atoms in the red 3D molasses and lattice. On the left, the fluorescence of atoms is projected onto $\hat{x}$, the direction perpendicular to the lattice (shown in pink). It is shown with a fit to the sum of two Gaussians (in dashed purple) to extract the fraction of atoms loaded into the lattice. We achieve a loading fraction from the red 3D molasses into the lattice of 9.7(5)% for a stationary lattice, which was calculated as the area under the fitted lattice Gaussian divided by the sum of the areas under the fitted red 3D molasses and lattice Gaussians.

into the lattice.

This optical lattice is supported by the same cavity that the atoms interact with via narrow-linewidth transitions, ensuring spatial overlap between the atoms and cavity mode. Atoms are attracted to regions of high intensity of the lattice light. Because the high intensity regions occur every half wavelength of the lattice light, the atoms are tightly confined along the cavity axis, which eliminates a problem associated with atomic motion along the cavity: Doppler shifts. The wavelength of the lattice light is set near a "magic" value, which minimizes perturbations of the milliHertz linewidth clock transition [103, 109].

Unlike a 2 mirror cavity, a ring cavity supports a travelling wave mode, which we use to transport atoms from the loading region to a quieter region of the cavity. We generate a travelling wave lattice with wavelength $\lambda_\ell = 813$ nm moving at $v = \delta_\ell \lambda_\ell/(2\pi)$, where v is the velocity of the lattice with respect to the lab frame. To do this, we inject light into the clockwise direction at frequency $(\omega_c - \delta_\ell)$ and the counter-clockwise direction at frequency $(\omega_c + \delta_\ell)$, where ω_c is the

cavity resonance frequency.

We calculate the number of atoms coupled to the cavity mode by measuring the collective vacuum Rabi splitting, $\Omega = 2g\sqrt{N}$, where $2g$ is the frequency of interaction between a single atom and the cavity mode [110, 111] and N is the total atom number. This approximation assumes that all atoms are homogeneously coupled to the cavity mode, all atoms are in the ground state, and the collective vacuum Rabi splitting is much bigger than the Zeeman splitting between atomic transitions. For a travelling lattice moving at $\delta_\ell = 2\pi \times 75$ kHz, we observe a steady-state vacuum Rabi splitting of 8.1 MHz, which gives a steady-state atom number of $1.3(2)\times10^6$ atoms. Combined with our 69(9) ms lattice loading time constant, we calculate a steady-state travelling lattice loading rate of $1.9(3) \times 10^7$ ^{88}Sr atoms per second. In Sec. 2.1, I estimated that we need a flux of at least 2×10^7 ^{88}Sr atoms per second loaded into the lattice to be in the regime where we are above the threshold atom number for superradiance on the mHz linewidth transition. Thus we are very close to the regime where we can deliver a high enough continuous flux of atoms loaded into the ring cavity in the strong collective atom-cavity coupling regime to be above the threshhold atom number for superradiance!

In our travelling lattice configuration, we are concerned about parametric heating, which occurs when driving a harmonic oscillator at twice its resonance frequency. In a typical standing wave lattice configuration, the lattice is locked on resonance with the cavity mode and there is only a second order conversion from laser frequency noise to amplitude noise in the cavity. In our case, we have two lattice tones that are detuned from the cavity resonance, which allows a first order conversion from laser frequency noise to amplitude noise in the cavity. We symmetrically detune the tones from the cavity resonance and balance the powers in the tones in order to minimize parametric heating. However, we think that for nonzero δ_ℓ, parametric heating limits the lattice lifetime.

In our case, we are concerned about parametric heating at twice the longitudinal oscillation frequency of the lattice. Typical lattice trap depths are around 150 μK, which have a longitudinal frequency of 200 kHz. It is hard to get much suppression of laser frequency noise at a frequency

offset of 400 kHz from the laser carrier using a Pound-Drever-Hall (PDH) style lock to a stable cavity, as typical unity gain frequencies are around 1-2 MHz. Thus we built a cateye configuration interference filter diode laser [112] at 813 nm designed to have a lower intrinsic Lorentzian linewidth to mitigate parametric heating. To evaluate the performance of our new interference filter laser, we compared the lattice lifetime in the 2-mirror cavity using this new laser to the lifetime using our old homebuilt littrow configuration diode laser. The lattice lifetime was 20 times longer with our cateye laser, so it has 20 times less frequency noise at 400 kHz. We observed the transition from Gaussian noise to Lorentzian noise of the new laser around 150 kHz, so we concluded that the intrinsic Lorentzian linewidth of this laser is around 20 times narrower.

2.7 Cavity Locking Schemes

The ability to tune and stabilize the resonance frequency of the ring cavity is crucial for our experiments. There are two sets of paths coupled to the cavity that are critical for generating a travelling wave lattice and probing the vacuum Rabi splitting: the two counter-propagating 813 nm lattice beams and the 689 nm s-polarized cavity probe beam. We want to be able to tune the frequency and amplitudes of these beams, so we do not want to stabilize the cavity to either of these beams or lock either laser to the cavity via these beams. Thus we have two additional paths, one to lock the cavity to 689 nm p-polarized light and one to lock the 813 nm lattice to the cavity. All of these paths are depicted in Fig. 2.15.

2.7.1 Stabilizing the Cavity to 689 nm Light

Our 689 nm laser is stabilized to our stable reference cavity by a Pound-Drever-Hall (PDH) lock on a sideband that provides a tunable offset. We adjust this offset so that the laser carrier is about $f_{la} \sim 78$ MHz to the blue of the bare $^1S_0$ to $^3P_1$ atomic transition frequency. This lock is performed with fairly high bandwidth (roughly 1 MHz unity gain frequency). The s and p 689 nm cavity modes are split in frequency by $f_{sp} = 488.836(5)$ MHz, just less than a third of a free spectral range. A free space EOM adds sidebands to the 689 s-polarized path close to f_{la} that can

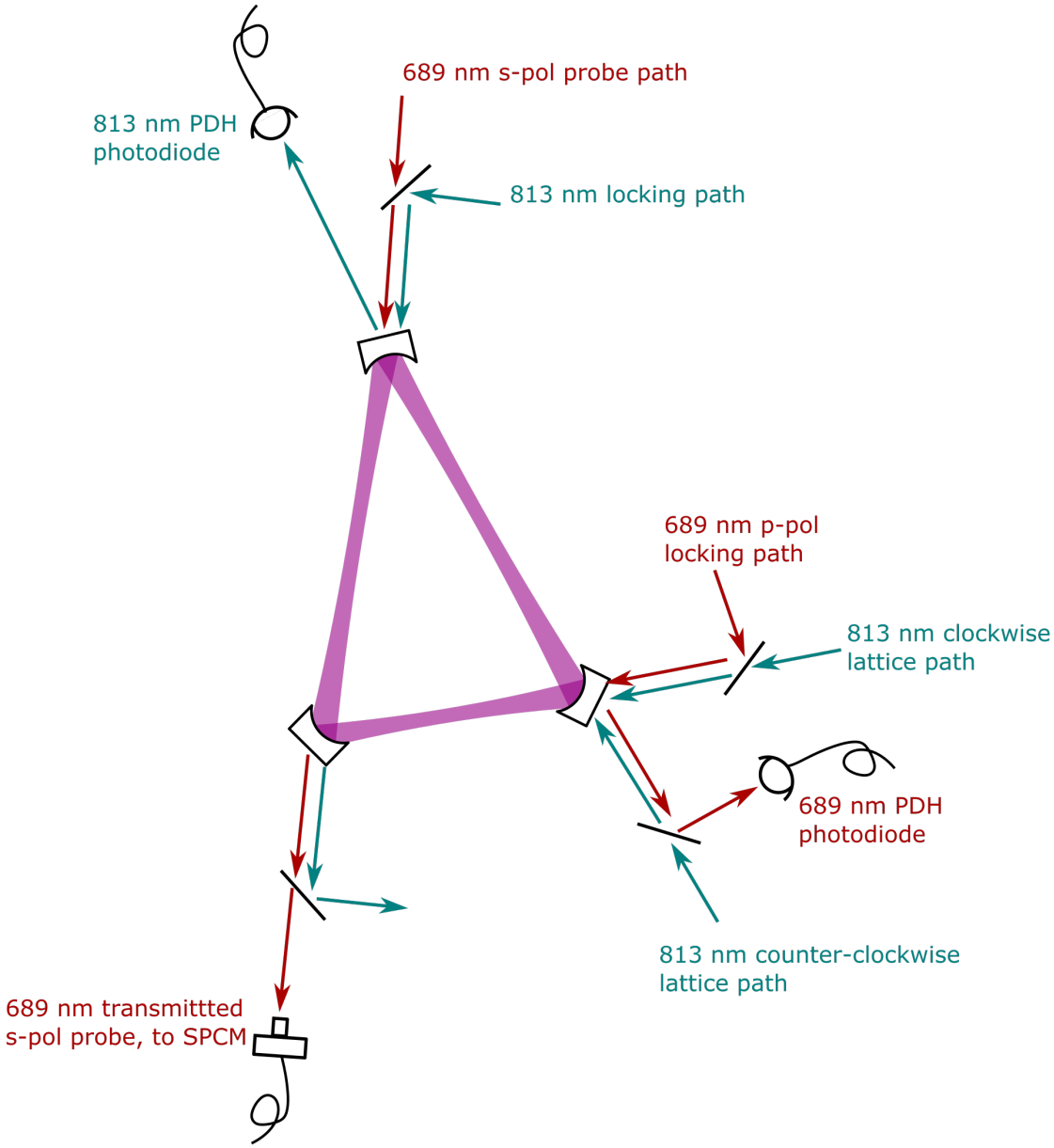

Figure 2.15: Cartoon representation of our cavity locking scheme. The main two sets of paths coupled to the cavity are the two counter-propagating 813 nm lattice beams, which are coupled into the bottom right mirror (mirror 1) and generate a travelling wave lattice, and the 689 nm s-polarized cavity probe beam, which is coupled into the top mirror (mirror 3) and probes the coupled atom-cavity system. We want to be able to tune the frequency and amplitudes of those beams, so we do not want to stabilize the cavity to either of those tones or stabilize either the 813 or 689 nm laser to the cavity via those tones. Thus we have two additional paths, one to lock the cavity to 689 nm p-polarized light, coupled in through the bottom right mirror, and one to lock the 813 nm laser to the cavity, coupled in through the top mirror.

be swept in frequency with a function generator and triggered by the data acquisition control.

The 689 nm p-polarized locking path starts at the laser carrier frequency and has tones added at $f_{PDH689} = 10$ MHz and $f_{\mu wave} = f_{sp} + f_{PDH689} + f_{la} = 577.2$ MHz by a fiber electro-optical modulator (EOM). We stabilize the frequency of the ring cavity to the reference cavity by feeding back to the piezo on the ring cavity based on a PDH error signal generated from one of the $f_{\mu wave}$ sidebands. The sidebands we lock to are set by the choice of signs when adding the frequencies in $f_{\mu wave}$. We lock to a sideband, rather than the central feature of the error signal, to minimize the transmitted power while maximizing the signal to noise of the error signal. The bandwidth with which the ring cavity frequency is stabilized relative to the reference cavity is limited by the piezo on the ring cavity. The first mechanical resonance appears at around 7 kHz, which limits the feedback bandwidth to the piezo to roughly 200 Hz before oscillations become apparent if a simple PI controller is used. This dramatically limits the degree to which we can suppress harmonics of 60 Hz that appear on the output of our high voltage source (unless we decided to do something more sophisticated [113]).

To observe a vacuum Rabi splitting, most of the atoms need to be in the ground state. This sets the requirement that there must be many more atoms in the cavity than photons on resonance with the atomic transition. For typical atom numbers around $N \sim 10^5$, we must have at a maximum 10^4 photons in the cavity mode, which is a power coming out of mirror 2 of 6.1×10^{-11} Watts. This sets the maximum power allowed in the vacuum Rabi splitting probe beam. Even a small background from the 689 nm locking light could overwhelm the transmitted probe, so we took a few precautions to minimize this background. We lock to the sideband of the 689 PDH error signal rather than the carrier, the light propagates in the opposite direction of the probe (but has some backscatter described in Sec. 2.5.5), and the light is orthogonally polarized to the probe and a Glan-Thompson prism before the SPCM rejects the p-polarized locking light.

The splitting between the s and p 689 nm cavity modes means that the p-polarized locking light is far off resonance with the atomic transition. We want the ac-stark shift to the atoms from the transmitted locking beam to be less than the cavity linewidth, but this turns out to be a much

less restrictive criterion than not overwhelming the probe signal incident on the SPCM.

2.7.2 Stabilizing 813 nm Light to the Cavity

To stabilize the 813 nm laser to the cavity, we inject about 1 mW of light into mirror 3 in the counter-clockwise direction. The light is detuned by one free spectral range from the center frequency of the lattice beams in order to minimize the impact of the locking light on the lattice. A fiber EOM adds tones at $f_{latt} = FSR - 80$ MHz and $f_{PDH813} = 13.5$ MHz. We feed back to the current and piezo of the homebuilt 813 nm laser based on a PDH error signal generated from one of the f_{latt} sidebands. This lock is performed with fairly high bandwidth (roughly 700 kHz unity gain frequency).

To generate the lattice at $\lambda_\ell = 813$ nm, we inject light into mirror 1 in the clockwise direction detuned $-\delta_\ell$ from the cavity resonance and light in the counter-clockwise direction detuned δ_ℓ from the cavity resonance. This generates a travelling wave moving at velocity $v = \lambda_\ell \delta_\ell/(2\pi)$. Around 15 mW in each lattice path incident on the cavity mode generates a lattice depth around 150 μK. We generate the two lattice frequencies by sending each beam through an AOM with RF frequency $80 \pm \delta_\ell/(2\pi)$ MHz. These RF tones are generated by the data acquisition hardware using a Novatech DDS9m board and can be controlled synchronously with the experiment.

Chapter 3

Continuous Loading of a High Flux of Strontium Atoms into an Optical Cavity

The first scientific project using the new continuous system has been a demonstration of the novel capabilities afforded by taking a cold atom-cavity experiment to the steady-state regime. Section 3.1 describes possibly the first demonstration of deterministic transport of atoms around a cavity, Sec. 3.2 possibly the first steady-state loading of atoms into a lattice supported by a cavity, and Sec. 3.3 the highest phase space density reported for a continuous atomic beam. Chapter. 4 describes the first demonstration of steady-state strong collective coupling between an optical cavity and atoms, via a forbidden optical transition. The results in Chapters 3 and 4 are also presented in a paper currently in preparation.

3.1 Deterministic Transport of Atoms around a Cavity

Atoms have been transported using either magnetic traps [114, 115] or optical traps [116], or a combination of the two traps. Magnetic transport relies on the translation of the trap minimum either by tuning the current in overlapping pairs of coils [114] or by mechanically moving a single pair of coils [115]. While magnetic transport generates a large trap depth and has been demonstrated reliably for large distances, it requires complex mechanical engineering and is only applicable to magnetically trappable atoms.

Optical transport, on the other hand, can be implemented for any atomic species, although typically at lower trap depths. The most straightforward implementation consists of mechanically relocating the focusing lens of the trap with a large translation stage [116]. Since moving mechanical

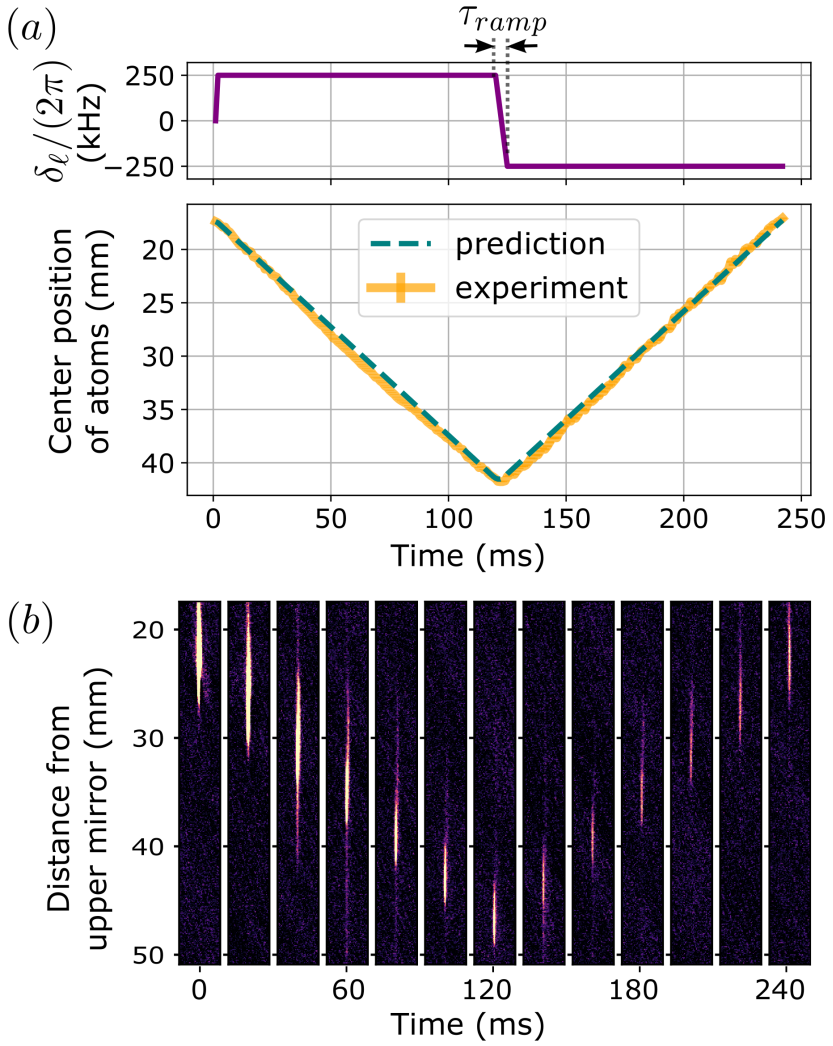

Figure 3.1: Deterministic transport of atoms around the cavity. Atoms are loaded into a stationary lattice ($\delta_\ell = 0$), the lattice detuning is linearly ramped to 250 kHz to transport the atoms down the cavity, and then reversed in time τ_{ramp} to transport the atoms back up the cavity. For this sequence, (a) shows the lattice detuning (purple), center position of atoms along the cavity (yellow), and prediction of the center position (dashed teal). The prediction curve is the integral of the lattice velocity $v = \lambda_\ell \delta_\ell/(2\pi)$. (b) shows single shot fluorescence images at selected times for the data plotted in (a).

parts introduce vibrations, novel schemes based on focus-tunable lenses have been developed [117]. The total transport duration for the moving lens or focus-tunable lens schemes is fundamentally limited by small longitudinal trapping frequencies or by the finite velocities of the mechanical stages, which results in transport times on the order of a second for typical transport distances.

This motivates the use of travelling-wave optical lattices, where the motion of the atoms is controlled via the radio-frequency detuning of two counter-propagating laser beams. This configuration offers large longitudinal trapping frequencies and does not require moving mechanical components [118, 119, 120, 121]. For Gaussian beams, the transport distance is typically limited by the Rayleigh range of the waist and is only applicable over short distances or in the vertical direction, because of the weak radial confinement compared to gravity. Interfering a Bessel and a Gaussian laser beam can realize nearly homogeneous trapping conditions over a 20 to 30 cm long transport length [119, 121]. Because they can be operated in steady-state, travelling wave optical lattices are also the only method compatible with continuously transporting atoms.

In this thesis, I present a different method of transporting atoms: a travelling wave optical lattice supported by an optical cavity. To generate the running-wave optical lattice, we symmetrically change the frequency of two counter-propagating lattice beams coupled into our ring cavity by changing the RF frequencies sent to the two lattice AOMs. I will briefly note here that the lattice beams are no longer on resonance with the cavity, which means we worry about parametric heating (more details can be found in Sec. 2.6.4). Our ring cavity (shown in Fig. 2.7) has offset sagittal and tangential waists (shown in Fig. 2.8), in order to produce a large region of the cavity where the lattice depth varies only slightly. The main cavity arm has a 5 cm region over which the geometric mean of the sagittal and tangential waists changes by less than $\sqrt{2}$, which produces a change in the lattice depth of < 2.

Fig. 3.1 demonstrates our capability to deterministically transport atoms around the cavity. We first load atoms into a stationary lattice ($\delta_\ell = 0$) and then linearly ramp the lattice detuning to 250 kHz in $\tau_{ramp} = 1$ ms to transport the atoms down the cavity, and then reverse the lattice detuning in time $\tau_{ramp} = 5$ ms to transport the atoms back up the cavity. For this sequence, Fig. 3.1(a) shows the lattice detuning and fitted center position of atoms along the cavity and Fig. 3.1(b) shows the single shot fluorescence images at selected times. The prediction of the center position is the integral of the lattice detuning, expressed as a distance.

We also measure the atom loss due to accelerating the atoms. We define a_e as the acceleration

for which $1/e$ of the atoms survive in the lattice, compared to the number of atoms with a very slow acceleration. If we fix the frequency range of the ramp to 500 kHz and vary the ramp time τ_{ramp}, we observe an e-fold loss acceleration of $a_e = 250$ MHz/s. We do not yet understand what is causing this loss.

3.2 Continuous Loading of Atoms into a Traveling Wave Optical Lattice

While hot atomic and molecular beams have been studied since 1911 [122], continuous cold atomic beams are quite new. Continuous transport of a high phase-space beam was first realized in 2019 [98]. In this system, strontium atoms were launched out of a red 3D MOT into a dipole transport guide. A dark spot in the MOT beams along the dipole beam axis allowed atoms to escape the MOT and a push beam set their velocity.

In this Section, I present the continuous loading of atoms into a traveling wave optical lattice supported by an optical cavity. Unlike a dipole trap which has no confinement along the transport direction, a lattice confines the atoms tightly along the direction of transport. In our case, the direction of transport is along the cavity mode, so the tight confinement prevents Doppler shifts along the cavity mode, which is crucial for a demonstration of superradiance. Additionally, we can precisely set the transport velocity of the atoms by tuning two well-determined RF frequencies, which set the detuning between the two counter-propagating lattice beams.

Fig. 3.2(a) depicts the measured lattice lifetime versus lattice detuning for two different lattice trap depths, T_ℓ. The lattice lifetime decreases with increasing trap depth, supporting our hypothesis that is it limited by parametric heating. What is parametric heating? For a more detailed description, see Sec. 2.6.4. To briefly explain, in a standing wave cavity, one typically locks a lattice on resonance with the cavity, where there is no first order conversion from laser frequency noise to amplitude noise inside the cavity. In our case, we are sending in tones detuned from the cavity resonance so there is a linear conversion from frequency noise to amplitude noise. We mitigate this effect by sending in nominally equal power, symmetrically detuned tones about the cavity resonance.

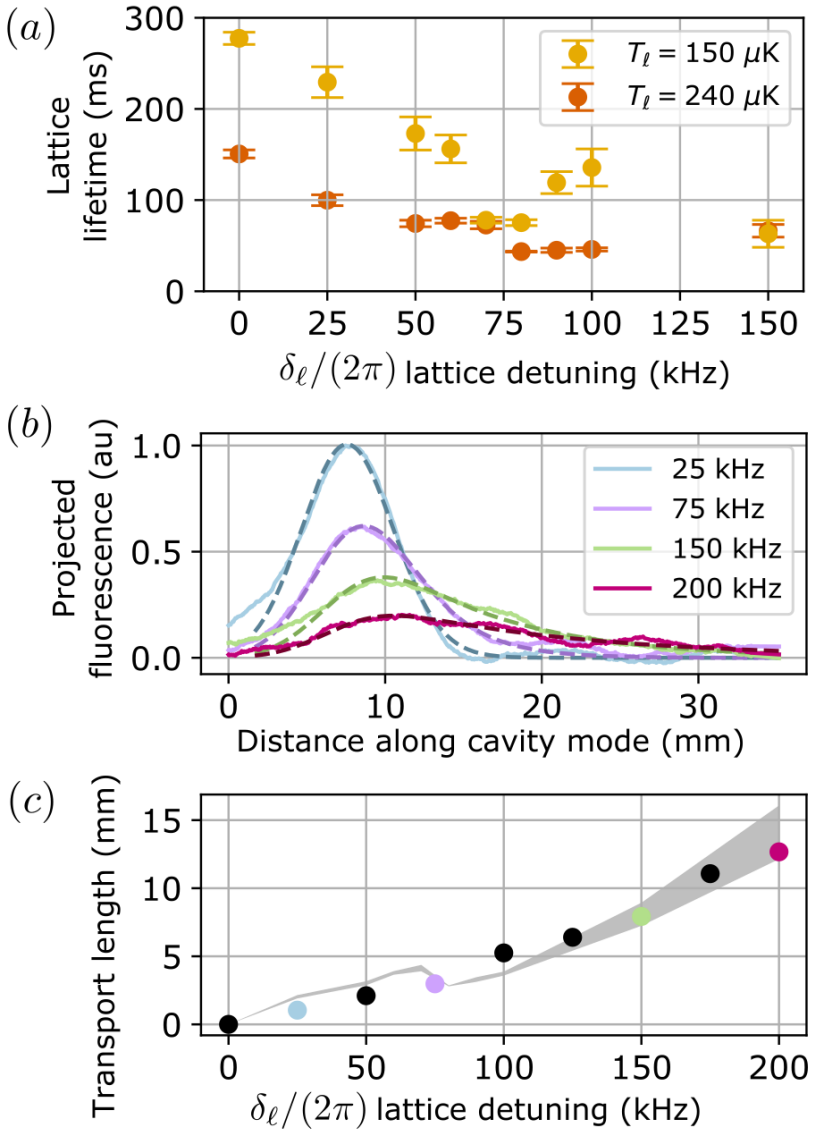

Figure 3.2: Continuous loading of atoms into a traveling wave optical lattice: (a) Measured lattice lifetime versus lattice detuning for lattice depths T_ℓ = 150 μK and 240 μK are shown in yellow and orange, respectively. (b) Atomic distribution projected onto the cavity mode for various lattice detunings, after loading atoms into the lattice for 350 ms (solid lines) and fits to Eq.3.1 (dashed) (c) Transport length extracted from the fit in (b) versus lattice detuning. Colored points match the projections plotted in (b) and black points represent additional detunings. The grey shaded region indicates the measured lattice lifetime times the lattice velocity.

In Fig. 3.2(b) and (c), we demonstrate loading atoms into a travelling wave optical lattice. The density of atoms loaded into a stationary lattice has a Gaussian profile along the lattice, with the width σ and center position z_0' set by the spatial profiles of the beams addressing the atoms.

When we load atoms into a travelling wave lattice, atoms are dragged from the stationary lattice profile in the direction set by the lattice velocity $v = \delta_\ell \lambda_\ell/(2\pi)$. But as we saw in Fig. 3.2(a), the lattice lifetime τ_ℓ varies with lattice detuning, so a faster travelling lattice typically has a shorter lattice lifetime. Thus the distance the atoms are transported along the cavity scales with the lattice velocity and lattice lifetime. We call this distance the transport length ℓ_t and can express it as the product of the lattice velocity v and the lattice lifetime: $\ell_t = v \cdot \tau_\ell$.

If we start loading atoms into the lattice at time 0 and stop loading the atoms at time t, the number of atoms along the cavity axis $N(z')$ can be characterized as:

$$N(z') = \int_0^t R \cdot \exp\left(\frac{-v(t-t')}{\ell_t} - \frac{(z' - z_0' - v(t-t'))^2}{2\sigma^2}\right) dt' \tag{3.1}$$

where R is the loading rate of atoms into the lattice. This integral does not have an analytic solution, but can be expressed as an error function.

Fig. 3.2(b) shows the measured number of atoms along the cavity mode $N(z')$ for various lattice velocities, as well as fits to Eq. 3.1. In this sequence, we turn the lattice on at time 0 to start loading into the lattice and image the cavity 350 ms later. In the fit, σ and z_0' are set by the stationary lattice ($\delta_\ell = 0$) and the only two fit parameters are the transport length ℓ_t and the loading rate R. The fitted ℓ_t is plotted versus lattice detuning in Fig. 3.2(b). The grey shaded region indicates the transport length predicted by the measured lattice lifetime times the lattice velocity, with error bars from the lattice lifetime (as shown in Fig. 3.2(a)). The transport length extracted from the fit agrees remarkably well with the transport length predicted by $\ell_t = v \cdot \tau_\ell$.

Additionally, we wanted to convince skeptics that the atoms we are looking at are indeed trapped in the lattice, as there are background atoms in the red 3D molasses and potentially atoms confined in the dipole potential of the lattice but not trapped in a lattice pancake. We ran a sequence where we loaded atoms into a travelling lattice for a few seconds, turned off all the loading beams and ramped the lattice detuning to 0, waited for all the background atoms to fall away, and then took a picture. Our result in this case was the same as is shown in Fig. 3.2, with the exception of lower overall atom numbers, due to holding the atoms in a lattice for longer with

finite lattice lifetimes.

3.3 Phase Space Density

The development of atomic ensembles with high phase space density (PSD) was originally motivated by efforts to realize a Bose-Einstein Condensate (BEC) [2]. More than 25 years later, we are starting to enter the regime where we can generate beams of atoms with high phase-space densities. These steady-state atomic sources promise to mitigate the Dick effect aliasing [123] intrinsic to almost all of today's pulsed cold atom sensors, where frequency-noise aliasing arises from the dead time between sample interrogations. Additionally, steady-state atomic sources can enable two novel devices: a continuous wave superradiant laser and an atom laser. I have already motivated the creation of a superradiant laser, so here I will introduce an atom laser.

An atom laser is the matter-wave analogue of the optical laser and is perhaps the ultimate source for many cold-atom sensors [124]. In an atom laser, as in an optical laser, the output beams can display desirable properties such as low divergence, high spectral flux, a simple spatial mode, and phase coherence. The high brightness and low divergence of atom laser sources may well allow us to improve substantially on current cold atom inertial sensing technology, as current devices have improved significantly in stability, size and reliability over the last decade, but published sensitivities have not improved substantially in that time. For example, a physically small, low divergence beam of atoms would sample a small region of the spatial mode of the beam splitter and mirror pulses of an atomic interferometer, mitigating imperfections in optical phase fronts that can limit atomic interferometers [125].

Here are the record demonstrations of continuous atomic sources with high phase space density: in 2004 and 2005, Lahaye et al. demonstrated steady-state beams with a PSD of 10^{-7} by repeatedly out-coupling rubidium atoms from a MOT and evaporatively cooling them as they traversed a 4.5-m-long magnetic waveguide [126, 127]. In 2010 and 2011, Aghajani-Talesh and Falkenau et al. realized a chromium beam with 10^7 atoms per second and a PSD of 3×10^{-8} by loading atoms from a moving molasses MOT into a magnetic guide, magnetically compressing the

atoms, and cooling them with an optical molasses [128, 129]. In 2013, Knuffman et al. produced a cesium beam with 5×10^{10} atoms per second and a PSD of 4×10^{-8} by compressing the output of a 2D MOT and cooling the transverse temperature with an optical molasses, before ionizing the atoms to produce a ion beam for focused ion beam applications [130]. In 2019, Chen et al. demonstrated a continuous ^{88}Sr source delivering an atomic beam with 3×10^7 atoms per second and a PSD more than three orders of magnitude greater than previous demonstrations, $1.5(2) \times 10^{-4}$ in the moving frame [98].

In this work, we demonstrate a new record in phase space density for a continuous atomic beam. For atoms loaded in a lattice travelling at $\delta_\ell = 2\pi \times 75$ kHz, we realize a phase space density in the travelling frame of $6(1) \times 10^{-3}$ within each lattice site and $1.0(2) \times 10^{-3}$ over the entire ensemble!! In the following paragraphs, I walk through the phase space density calculation.

We calculate the number of atoms coupled to the cavity mode by measuring the collective vacuum Rabi splitting, $\Omega = 2g\sqrt{N}$, where $2g$ is the frequency of interaction between a single atom and the cavity mode [110, 111] and N is the total atom number. This approximation assumes that all atoms are homogeneously coupled to the cavity mode, all atoms are in the ground state, and the collective vacuum Rabi splitting is much bigger than the Zeeman splitting between atomic transitions. For a travelling lattice moving at $\delta_\ell = 2\pi \times 75$ kHz, we observe a steady-state vacuum Rabi splitting of 8.1 MHz, which gives a steady-state atom number of $1.3(2) \times 10^6$ atoms. Combined with our 69(9) ms lattice loading time constant, we calculate a steady-state travelling lattice loading rate of $1.9(3) \times 10^7$ ^{88}Sr atoms per second.

To calculate the atom density, we need to know the temperature of the atoms, the waist of the lattice and the extent of the atoms along the lattice. The extent of the atoms along the lattice is given by the full-width half maximum of the red 3D molasses projected onto the lattice and is 2.8 mm. This gives an average of 196 atoms per lattice pancake.

Approximately where we load atoms into the lattice, 2 cm away from the upper cavity mirror, the sagittal ($\hat{y}$) and tangential ($\hat{x}$) cavity waists at 813 nm are $w_s = 76.4$ and $w_t = 92.2$ μm. The trap width along the longitudinal direction is half the lattice wavelength, $\lambda_\ell/2$, which for us is

813/2 nm. We make the assumption that within each lattice pancake, the atoms explore a region corresponding to the width of the trap at the atoms' 1D root-mean-squared temperature T, relative to the trap depth T_ℓ. For a lattice along $\hat{z}$, the longitudinal direction, the potential is:

$$U(z) = T_\ell \ \sin^2(2\pi z/\lambda_\ell) \tag{3.2}$$

Setting $U(z) = T$ and solving for z gives half the root-mean squared (rms) width explored by the atoms, $z_{rms}/2$. Thus the full width the atoms explore in the longitudinal direction,z_{rms}, can be expressed as:

$$z_{rms} = \frac{\lambda_\ell}{\pi} \arcsin\left(\sqrt{T/T_\ell}\right) \tag{3.3}$$

Similarly, the potential of the lattice in the $\hat{x}$ direction is:

$$U(x) = T_\ell \ (1 - \exp\frac{-2x^2}{w_t^2}) \tag{3.4}$$

And we can express the rms length the atoms explore x_{rms}, as:

$$x_{rms} = 2\sqrt{\ln\left(1 - T/T_\ell\right)^{-w_t^2/2}} \tag{3.5}$$

The rms length the atoms explore in the $\hat{y}$ direction y_{rms} is identical to Eq. 3.5, with a substitution of the sagittal waist, w_s, for the tangential waist, w_t.

The lattice trap depth is $T_\ell = 150$ μK, the temperature of the atoms along the lattice (in the longitudinal direction) is $T_z = 11(2)$ μK, and the temperature transverse to the lattice (in the radial direction) is $T_r = 3.1(3)$ μK. The atomic temperatures were measured by fluorescence time of flight imaging. Thus the lengths the atoms explore in the longitudinal, tangential, and sagittal directions are $z_{rms} = 71(7)$ nm, $x_{rms} = 18.8(9)$ μm, and $y_{rms} = 15.6(8)$ μm. This gives us an atom density of $\rho = 9.4 \pm 1.5 \times 10^{18}$ atoms/m^3 (equivalently, $9.4 \pm 1.5 \times 10^{24}$ atoms/cm^3).

To convert from atom density to phase space density, we multiply the atom density by the thermal DeBroglie wavelength (Λ) cubed [131]. The phase space density can be thought of as the number of particles in a box of size $\hbar^3$ in phase space. For an atom of mass m and 1D temperature T, with the Boltzmann constant k_B and reduced Planck constant $\hbar$, Λ is defined as:

$$\Lambda = \frac{\hbar\sqrt{2\pi}}{\sqrt{k_B m T}} \tag{3.6}$$

Because we have different temperatures in the longitudinal (T_z) and radial (T_r) directions, the phase space density can be calculated as:

$$PSD = \rho \left(\frac{\hbar \sqrt{2\pi}}{\sqrt{k_B m T_r}} \right)^2 \frac{\hbar \sqrt{2\pi}}{\sqrt{k_B m T_z}} \tag{3.7}$$

For atoms loaded in a lattice travelling at $\delta_\ell = 2\pi \times 75$ kHz, we realize a phase space density in the travelling frame of $6(1) \times 10^{-3}$ within each lattice site and $1.0(2) \times 10^{-3}$ over the entire ensemble!! Compared to the previous phase space density record of $1.5(2) \times 10^{-4}$ [98], our PSD for the entire ensemble is almost an order of magnitude higher and our PSD within each pancake is around a factor of 40 higher. Also note that Ref. [98] uses the peak density to calculate the phase space density, while I use the root-mean-squared density to calculate the phase space density, so my estimate is lower than it should be in a direct comparison with Ref. [98].

Chapter 4

Steady-state Strong Collective Coupling Between an Optical Cavity and Atoms, via a Forbidden Optical Transition

In this Chapter, I present our work demonstrating steady-state strong collective coupling on a narrow linewidth atomic transition, a key milestone in the journey towards the creation of a mHz linewidth superradiant laser. Section 4.1 introduces the strong collective coupling regime, Sec. 4.2 provides a classical model of a vacuum Rabi Splitting, Sec. 4.3 shows our observation of a resolved vacuum Rabi splitting on a narrow linewidth atomic transition, Sec. 4.4 investigates the observed broadening of the vacuum Rabi splitting features and introduces the primary broadening mechanism, and Sec. 4.5 demonstrates a continuous vacuum Rabi splitting for more than twenty minutes.

4.1 Introduction to Collective Strong Coupling

Generally, the goal of cavity quantum electrodynamics (QED) is to create a situation where coherent interactions between the atoms and the cavity are larger than dissipation in the system. This regime is broadly referred to as the strong coupling regime. Often, strong transitions are used in cavity QED experiments to couple atoms to a cavity field. Here, we instead demonstrate strong collective coupling using the dipole forbidden $^1S_0$ to $^3P_1$ transition in ^{88}Sr. Eventually, we would like to demonstrate strong collective coupling on the mHz $^1S_0$ to $^3P_0$ transition in ^{87}Sr, another milestone towards realizing a continuous mHz linewidth superradiant laser. Strong collective coupling via a narrow linewidth transition is important for a superradiant laser because atoms must

be strongly coupled to the cavity to observe superradiance and the fundamental linewidth of a superradiant laser scales with the atomic transition linewidth.

In addition to superradiance, another motivation for strong coupling on dipole-forbidden transitions is to observe state-selective, non-destructive atom counting [132]. Atom counting has been used to generate highly spin-squeezed states that surpass the standard quantum limit on phase estimation [133, 134, 135, 106, 136, 137, 138]. Applied to optical lattice clocks, non-destructive atom counting [139] could enhance the performance of a range of precision measurements. There are two main avenues where non-destructive atom counting could enhance performance: by using entanglement to estimate the atomic phase below the standard quantum limit and by reducing the highly deleterious effects of Dicke effect noise, or local oscillator noise aliasing, [140, 141] that limit current state of the art optical lattice clocks.

What is the strong collective coupling regime? There are two main definitions of the strong collective coupling regime: the collectively enhanced cavity coooperativity must be greater than one $NC \gg 1$, where N is the atom number and C is the single atom cavity cooperativity, and the collective vacuum Rabi frequency Ω must exceed all relevant decoherence rates. The collective vacuum Rabi frequency scales as $\Omega = 2g\sqrt{N}$, where $2g$ is the frequency of interaction between a single atom and the cavity mode.

For the first requirement, $NC = \Omega^2/\kappa\gamma \gg 1$, where κ is the cavity power decay rate, and γ is the atomic transition linewidth. The cooperativity C is independent of the strength of the transition because $g \propto |\vec{d}|$ and $\gamma \propto |\vec{d}|^2$, where $\vec{d}$ is the dipole matrix element of the transition. A forbidden transition has a long-lived excited state because the dipole matrix element $\vec{d}$ associated with the transition is small. However, attaining $NC \gg 1$ is no harder when using a dipole-forbidden transition because the scaling with $\vec{d}$ drops out. Our system is just below the single-atom strong coupling regime, (i.e. $C \geq 1$) but for a characteristic atom number of $N \sim 10^5 - 10^6$, we are deep into the desired collective strong coupling regime $NC \sim 10^4 - 10^5$.

The second requirement is a more stringent definition of the strong collective coupling regime: the collective vacuum Rabi frequency must exceed relevant decoherence rates in the system. This

requirement must be satisfied in order to observe a resolved splitting of the normal modes of the coupled atom-cavity system, known as a collective vacuum Rabi splitting [142, 143]. In a vacuum Rabi splitting, the two modes are separated by $\Omega = 2g\sqrt{N}$. If the two peaks are resolved, it means that their separation, which is set by the rate of coherent interactions, exceeds their width, which is set by decay rates from the system. If a system satisfies the first requirement but not the second, one could observe cavity-enhanced spectroscopic features, but the vacuum Rabi splitting would not be resolved.

The second requirement necessitates not only $\Omega \gg \kappa, \gamma$, but also Ω must exceed other non-fundamental sources of broadening as well, notably Doppler decoherence. Fundamentally, $\Omega \gg \gamma$ is easier to achieve on a weak transition because $\Omega \propto g \propto |\vec{d}|$ and $\gamma \propto |\vec{d}|^2$. However, $\Omega \gg \kappa$ is harder to achieve on a weak transition and requires the use of a relatively high-finesse optical cavity. Because effects like Doppler shifts do not scale with the strength of the atomic transition, it is harder to overcome atomic decoherence when using narrow linewidth transitions, as the coherent interactions are much slower.

Previous works investigating strong collective coupling on a narrow linewidth atomic transition include cavity-enhanced nonlinear spectroscopy [144] of ^{88}Sr in a MOT in the pulsed regime [145, 146, 147], but inhomogeneous doppler broadening prevented the observation of a collective vacuum Rabi splitting. In other words, they did not satisfy the requirement that the collective vacuum Rabi frequency exceed the relevant decoherence rates in the system and thus could not observe the resolved vacuum Rabi splitting. When I first joined the Thompson Lab, fellow graduate student Matt Norcia had just demonstrated the first strong collective coupling between an optical cavity and atoms, via a forbidden optical transition [148]. This experiment was based on ^{88}Sr and operated in a pulsed regime where roughly every second, new atoms had to be captured into a MOT and cooled into the lattice.

Previous works on non-fluorescence based atom-counting were performed in ^{87}Sr [139, 140] and ^{171}Yb [149] using the dipole-allowed transition $^1S_0$ to $^1P_1$ and no optical cavity. Atomic projection noise level sensitivity was achieved, but with the scattering of ~ 100 photons per atom [139, 140]

and with uncharacterized scattering [149]. In Ref. [148], Matt also realized non-destructive differential atom number measurements at the equivalent of sub-projection noise sensitivity, with much less than one photon recoil imparted per atom. More recently, a many-atom entangled state on an ultra-narrow clock transition in ^{171}Yb was demonstrated and used to realize a Ramsey sequence with an Allan deviation below the standard quantum limit (after subtraction of the local-oscillator noise) [150]. Rather than directly generate entanglement on the narrow linewidth clock transition, they first generated spin squeezing between two nuclear sublevels via cavity feedback squeezing and then mapped the entanglement onto the optical clock state. This work was limited by Dick effect noise and by the phase noise of the local oscillator, which could both be reduced with a continuous strongly coupled atom source. A steady-state atom cavity system could reduce dead time between cycles, reducing Dick effect noise, and a steady-state superradiant laser could realize a narrow linewdith local oscillator.

In this work, we demonstrate the first steady-state strong collective coupling on a narrow linewidth atomic transition. To confirm that we have achieved the more stringent definition of the strong collective coupling regime, we show that we can observe a highly-resolved vacuum Rabi splitting, which constitutes a direct verification of the hierarchy $\Omega \gg \kappa, \gamma$.

4.2 Classical Description of a Vacuum Rabi Splitting

A coupled atom-cavity system in the strong coupling regime can be described classically, where the atoms are taken to be classical Lorentz oscillators in the mode of an optical cavity [151]. In this section, I will follow the formalism set out by Ref. [151] and then extend it to our system. Note that in this section, I am following the convention that frequencies represented by letters from the greek alphabet (ex. γ, δ) are expressed in radians per second and frequencies represented by letters from the latin alphabet (ex. f) are expressed in Hz.

The cavity has resonance frequency f_c, roundtrip length ℓ, free spectral range $FSR = c/\ell$, where c is the speed of light, and intensity transmission coefficient T_{in} for the input mirror (where light is coupled into the cavity) and T_{out} for the output mirror (outside of which the transmission

is observed). For a cavity with n_{mirror} mirrors, the round-trip field reflection coefficient r_{tot}, is the product of the field reflection coefficients r for each cavity mirror, $r_{tot} = \prod_{i=1}^{n_{mirror}} r_i$.

For N atoms with resonant full width half maximum γ detuned from the bare resonant frequency f_a by δ, the intensity absorption coefficient α at frequency f is given by:

$$\alpha(f, N, \delta) = \frac{N}{\eta_0} \frac{(\gamma/(2\pi))^2}{(\gamma/(2\pi))^2 + 4(f - f_a - \delta/(2\pi))^2} \tag{4.1}$$

where $\eta_0 \propto 1/(2g)^2$ is a factor to convert from absorption to atom number. For our system, $\eta_0 = 8.1 \times 10^4$. Note that compared to Eq. 4.1, the formula for α in Ref. [151], has one fewer factor of γ in the numerator. We suspect from dimensional analysis that this may be simply a typo.

Light inside the cavity experiences a total round trip phase shift ϵ with contributions from both the bare cavity ϵ_c and the atoms ϵ_a:

$$\epsilon_c(f) = \frac{2\pi(f - f_c)}{FSR} \tag{4.2}$$

$$\epsilon_a(f, N, \delta) = -\alpha(f, N, \delta) \frac{2(f - f_a - \delta/(2\pi))}{(\gamma/(2\pi))} \tag{4.3}$$

$$\epsilon(f, N, \delta) = \epsilon_c(f) + \epsilon_a(f, N, \delta) \tag{4.4}$$

The intensity transmission function of the coupled atom-cavity system is given by:

$$T_{cav} = \frac{T_{in} T_{out} e^{-\alpha}}{(1 - r_{tot} e^{-\alpha})^2 + 4 r_{tot} e^{-\alpha} \sin^2 \epsilon/2} \tag{4.5}$$

where for convenience I have dropped the (f, N, δ) from $\epsilon(f, N, \delta)$ and $\alpha(f, N, \delta)$ so that Eq. 4.11 fits on a single line.

We will pause our derivation to relate this equation back to a vacuum Rabi splitting. If we sweep a probe across the resonance of a bare cavity mode, we expect to see a Lorentzian cavity lineshape in transmission (as shown in Fig. 4.1). This corresponds to T_{cav} for $N = 0$. With atoms in the cavity, we observe a splitting in the normal modes of the atom-cavity system, where the two peaks are split by the collective vacuum Rabi frequency, $\Omega = 2g\sqrt{N}$. Each peak is half atom-like and half photon-like in character, and thus decays at a rate given by the average of the atom and cavity decays $\kappa' = (\kappa + \gamma)/2$. This decay rate determines the width of each of the two peaks. Similarly, the height of each peak is $\kappa^2/(\kappa + \gamma)^2$.

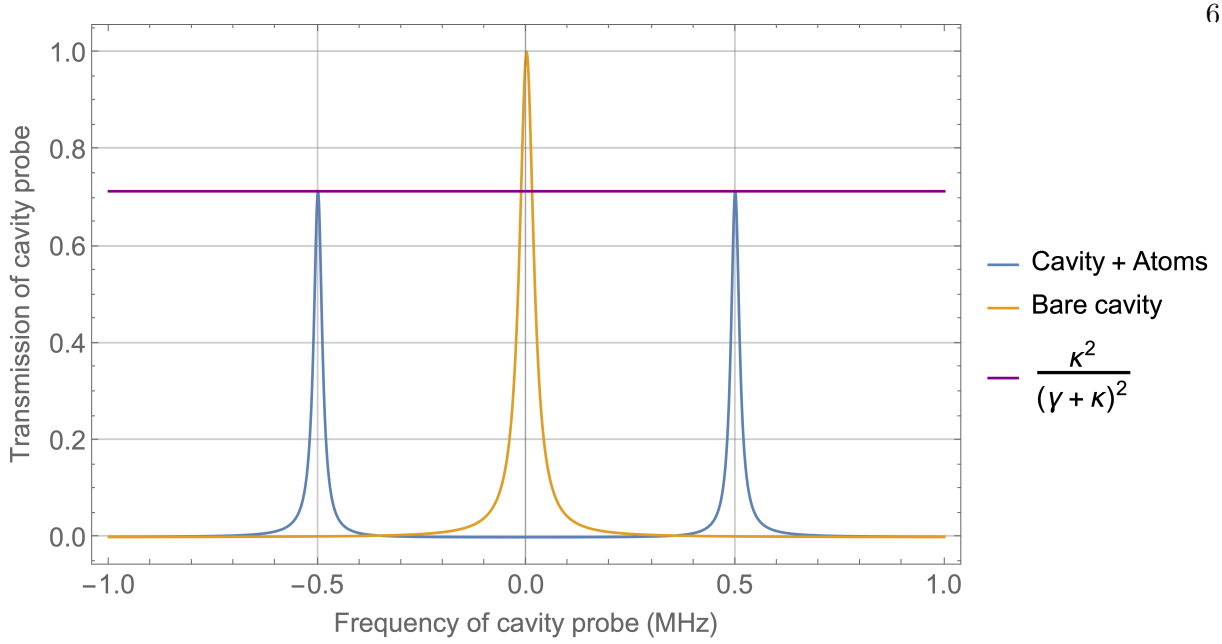

Figure 4.1: Vacuum Rabi splitting. Transmitted power as probe frequency is swept across the atomic resonance for a bare cavity (orange) and for a coupled atom-cavity system (blue). We observe a splitting in the normal modes of the atom-cavity system, where the two peaks are split by the collective vacuum Rabi frequency, $\Omega = 2g\sqrt{N}$. Each peak is half atom-like and half photon-like in character, and thus decays at a rate given by the average of the atom and cavity decays $\kappa' = (\kappa + \gamma)/2$. This decay rate determines the width of each of the two peaks. Similarly, the height of each peak is $\kappa^2/(\kappa+\gamma)^2$ (shown in purple). The transmission has been normalized to the height of the bare cavity resonance and the bare atomic resonance is on resonance with the cavity, $f_a = f_c = 0$

In our system, the ground state $^1S_0$ has only one level, but the excited state $^3P_1$ has three Zeeman levels. For a Zeeman splitting between the magnetic levels $m_F = 0$ and $m_F = 1$ of f_{ZS}, we can express the frequency-dependent intensity absorption coefficient with all three transitions α_{3t} and the round trip phase shift with three transitions $\epsilon_{a,3t}$ as:

$$\alpha_{3t}(f) = \alpha(f, N_+, f_{ZS}) + \alpha(f, N_0, 0) + \alpha(f, N_-, -f_{ZS}) \tag{4.6}$$

$$\epsilon_{3t}(f) = \epsilon_c(f) + \epsilon_a(f, N_+, f_{ZS}) + \epsilon_a(f, N_0, 0) + \epsilon_a(f, N_-, -f_{ZS}) \tag{4.7}$$

where N_+, N_0, and N_- sum to N and represent the normalized projection of the probe polarization onto σ^+, π, and σ^- (with the quantization axis set by the magnetic field) times $\sqrt{N_g - N_{e,i}}$, the square root of the number of atoms in the ground state minus the number of atoms in the excited

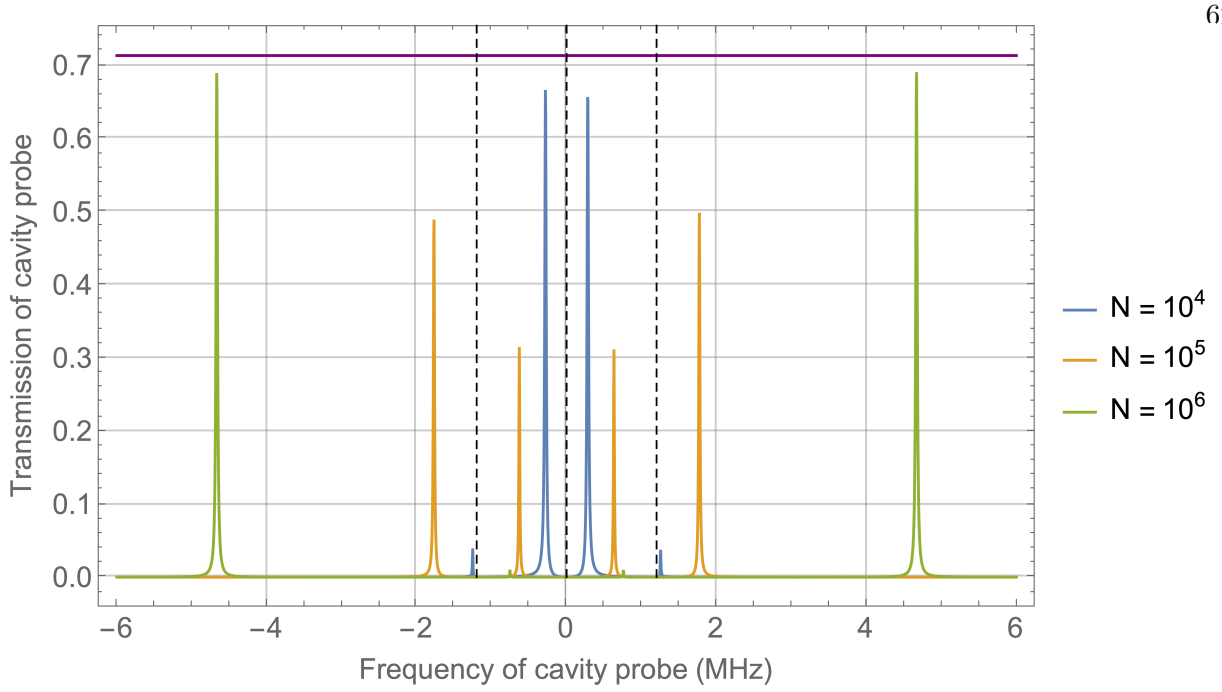

Figure 4.2: Vacuum Rabi splitting for atoms with one ground state and three excited states. Transmitted power as probe frequency is swept across the atomic resonance for three different atom numbers: $N = 10^4$ (blue), $N = 10^5$ (orange), and $N = 10^6$ (green). The three atomic resonances in the absence of the cavity are shown as dashed black lines for Zeeman splitting $f_{ZS} = 1.2$ MHz. In the regimes where the vacuum Rabi splitting is much smaller or larger than f_{ZS}, we observe two predominant peaks. However, in the intermediate regime, as is the case for $N = 10^5$, we observe four peaks. As in Fig. 4.1, the purple line represents $\kappa^2/(\kappa+\gamma)^2$, the height of an atom-cavity transmission feature for a single atomic transition. The transmission has been normalized to the height of the bare cavity resonance, the bare atomic resonance is on resonance with the cavity $f_a = f_c = 0$, and $N_+ = N_0 = N_-$.

state, for the excited $^3P_1$ $m_F = 1, 0$, and -1 states, respectively. The previous statement $\Omega = 2g\sqrt{N}$ is valid when all or almost all the atoms are in the ground state. For convenience, we express the atom numbers in terms of angles, as:

$$N_+ = N\cos(\theta)\sin(\phi) \tag{4.8}$$

$$N_- = N\cos(\theta)\cos(\phi) \tag{4.9}$$

$$N_0 = N\sin(\theta) \tag{4.10}$$

The intensity transmission function of the coupled atom-cavity system with three atomic

transitions is very similar to Eq. 4.11, with a substitution of $\alpha \to \alpha_{3t}$ and $\epsilon \to \epsilon_{3t}$:

$$T_{3t} = \frac{T_{in}T_{out}e^{-\alpha_{3t}}}{(1 - r_{tot}e^{-\alpha_{3t}})^2 + 4r_{tot}e^{-\alpha_{3t}}\sin^2\epsilon_{3t}/2} \tag{4.11}$$

Fig. 4.2 shows the intensity transmission function of the coupled atom-cavity system with three atomic transitions, T_{3t}, for three different atom numbers. In the regimes where the vacuum Rabi splitting is much smaller or larger than f_{ZS}, we observe two predominant peaks. For the smallest atom number case $N = 10^4$, the primary contribution to the vacuum Rabi splitting is from the $m_F = 0$ state, whereas for the highest atom number case $N = 10^6$, all the transitions contribute to generate a large vacuum Rabi splitting. However, in the intermediate regime, as is the case for $N = 10^5$, we observe four peaks. The experiment typically operates in the intermediate or large atom number regimes.

If there is no probe polarization projection onto π ($N_0 = \theta = 0$), we would be in a regime where we could observe magnetically-induced optical transparency [59]. In this case, there would be three transmission features, where the outer two correspond to the normal modes of the atom-cavity system and the center feature is a narrow spectroscopic feature that approaches the atomic transition linewidth.

4.3 Observation of a Steady-State Vacuum Rabi Splitting

Our goal is to demonstrate steady-state strong collective coupling on a narrow linewidth atomic transition. As a quick reminder, we are using the dipole forbidden $^1S_0$ to $^3P_1$ transition in ^{88}Sr, which has a wavelength of 689 nm and an atomic transition linewidth $\gamma = 2\pi \times 7.5$ kHz, roughly 3 orders of magnitude narrower than a dipole allowed transition of the same wavelength.

In Fig. 4.3, we observe a resolved vacuum Rabi splitting on a forbidden optical transition. We characterize the vacuum Rabi splitting by recording the transmitted power as the probe frequency is swept across the atomic resonance, for different atom numbers. We have an independent measure of the relative atom number via fluorescence imaging of atoms in the lattice. For the largest atom numbers, the predominant features are two resolved transmission peaks. We are in a similar limit to

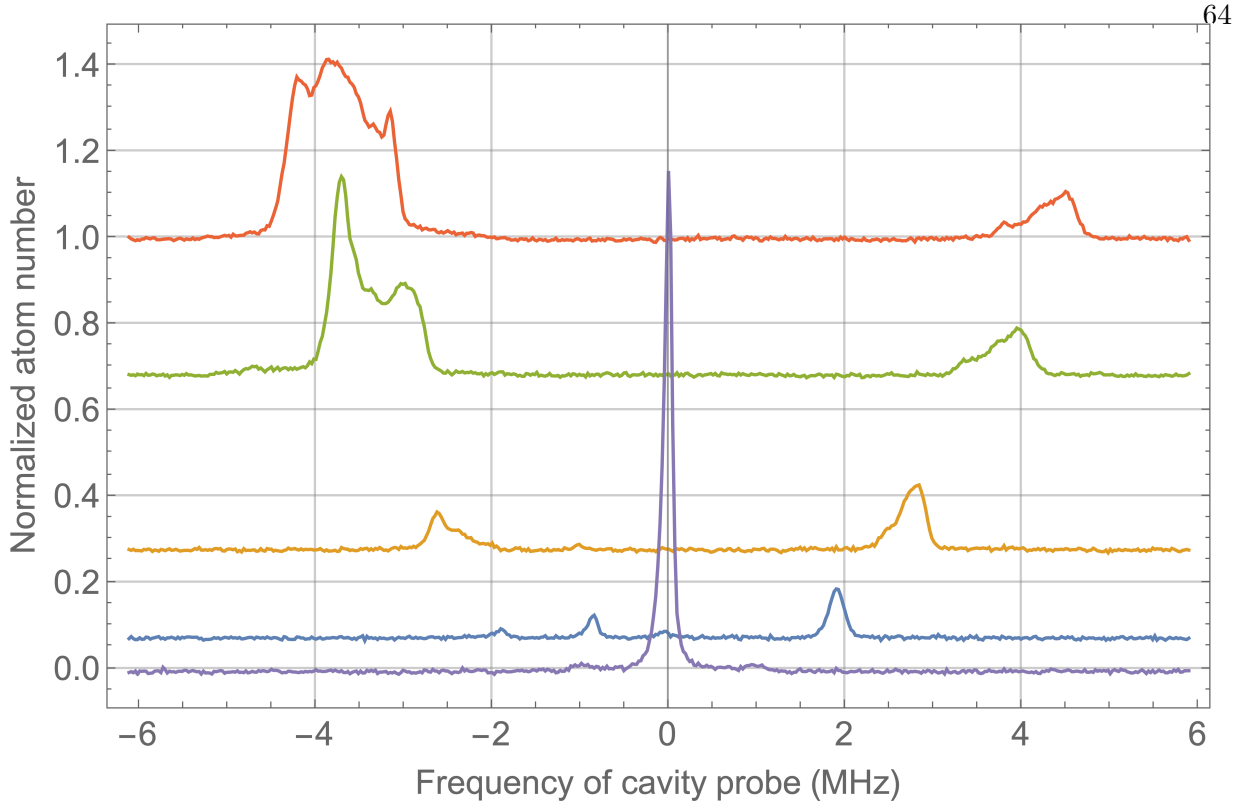

Figure 4.3: Observation of the collective strong coupling regime on a forbidden transition. We characterize the vacuum Rabi splitting by recording the transmitted power as probe frequency is swept across the atomic resonance for $\delta_{ac} \sim 0$. Traces correspond to different atom numbers, where the atom number is measured via fluorescence imaging of atoms in the lattice. For each trace, atoms are continuously loaded into a travelling lattice with $\delta_\ell = 2\pi \times 75$ kHz for 60 seconds (much longer than our vacuum lifetime of $\sim$ 300ms or our measured lattice lifetime) as the cavity probe repeatedly sweeps across the resonances. Traces shown are the average over 30 transmission spectra. The maximum splitting observed is 8.1 MHz (for the red trace).

the trace in Fig. 4.2 with the largest atom number, where the splitting is greater than the Zeeman splitting $f_{ZS} = 1.2(1)$ MHz. The maximum splitting between the outermost peaks is 8.1 MHz (for the red trace of Fig. 4.3). For the smallest nonzero atom number trace, the features are less distinct, but there are four transmission features, two close to ± 2 MHz, one close to 0 MHz, and one close to -1 MHz. This is in the intermediate limit (similar to the middle atom number trace in Fig. 4.2), where the splitting between peaks is comparable to the Zeeman splitting.

We measured the Zeeman splitting by turning our atom number down so that the vacuum Rabi splitting had two transmission features that were dominated by a single atomic resonance (as

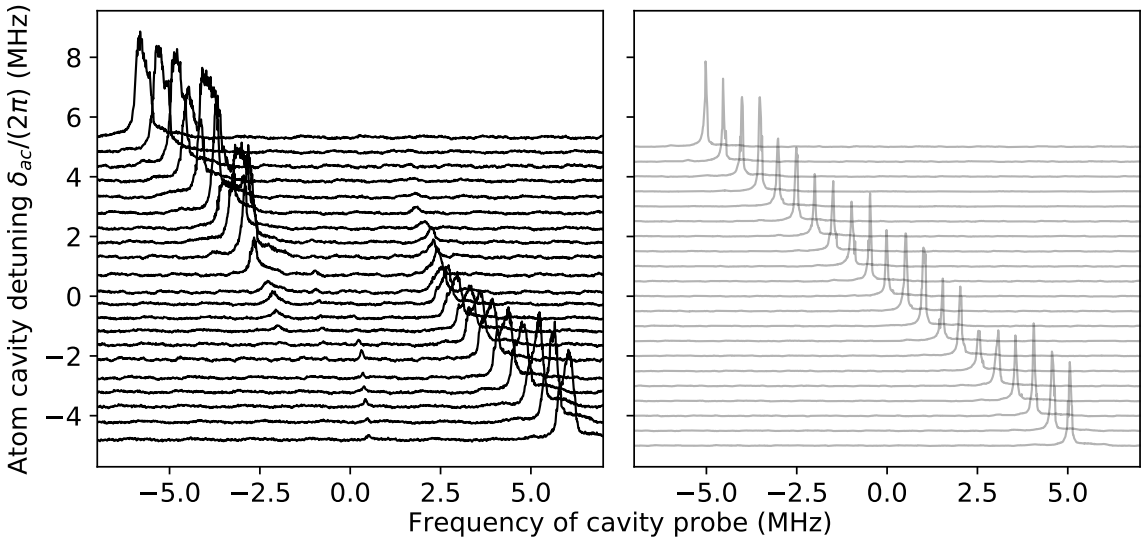

Figure 4.4: Observation of an avoided crossing in the vacuum Rabi splitting. Transmitted power as the probe frequency is swept across the atomic resonance with atoms coupled to the cavity (left) and without atoms in the cavity (right). Traces correspond to different cavity detunings, $\delta_{ac}/(2\pi)$. The bare cavity trace amplitudes have been divided by 5 to show them on the same scale.

in the small atom number trace in Fig. 4.2) and found the average frequency of the two transmission peaks. Then, we changed the atom cavity resonance δ_{ac} so that the contribution to the vacuum Rabi splitting was dominated by a different atomic transition, say the $^1S_0$ to $^3P_1$ $m_F = 1$ state, and again found the average frequency of the two transmission peaks. The Zeeman splitting $f_{ZS} =$ 1.2(1) MHz is the frequency difference between the average of the transmission peaks for $m_F = 0$ and $m_F = 1$. We also measured the frequency difference between the average of the transmission peaks for $m_F = -1$ and $m_F = 0$ and found it to be the same, within error bars.

For this work, the 689 nm probe laser frequency was stabilized to a reference cavity and the ring cavity was stabilized to a p-polarized 689 nm cavity resonance, as described in Sec. 2.7. We probe the atoms with a weak tone coupled to the cavity that is polarized normal to the plane of the cavity (s-polarized), as shown in Fig. 2.15, and measure transmitted power on a single photon counting module (SPCM).

For each trace, atoms are continuously loaded into a travelling lattice with $\delta_\ell = 2\pi \times 75$ kHz for 60 seconds (much longer than our vacuum lifetime of $\sim$ 300ms or our measured lattice lifetime) as the cavity probe repeatedly sweeps across the resonances. The probe sweeps in a symmetric triangle ramp with a 1 Hz frequency. Traces shown are the average over 30 transmission spectra (every upsweep of the triangle ramp). We found that averaging increased the signal to noise and did not change the width or shape of the transmission features.

We also observe an avoided crossing in the vacuum Rabi splitting spectra versus atom cavity detuning. Figure 4.4 shows a vacuum Rabi splitting obtained by continuously loading atoms into a travelling lattice ($\delta_\ell = 2\pi \times 100$ kHz), tuning the empty cavity resonance f_c near the atomic transition frequency f_a, and then recording the transmitted power as a cavity probe is linearly swept in frequency. We also plot the probe transmission for the bare cavity. The different traces in Fig. 4.4 correspond to different detunings $\delta_{ac} = 2\pi \times (f_c - f_a)$, and exhibit an avoided-crossing behavior.

At large detunings, we expect the center frequency of the main transmission feature to approach f_c, the center frequency of the bare cavity. The cavity frequency shift is the frequency difference between the transmission features with atoms in the cavity and without atoms (bare cavity) and can be expressed as $(2g)^2/(4\delta_{ac})$ (in the limit of large δ_{ac} for a single atomic transition). At zero detuning, we expect to see a vacuum Rabi splitting feature similar to in Fig. 4.3.

4.4 Broadening of the Vacuum Rabi Splitting

In Sec. 4.3, we demonstrated a resolved vacuum Rabi splitting, but the experimental transmission features are wider and shorter than one would expect from our earlier theoretical predictions (in Sec. 4.2). Additionally, the shape of the experimentally observed transmission features does not always correspond to a Lorentzian lineshape.

As seen in Fig. 4.1, for a cavity on resonance with a single atomic transition, we expect a splitting in the normal modes of the atom-cavity system, where the two peaks are split by the collective vacuum Rabi frequency, $\Omega = 2g\sqrt{N}$. Each peak is half atom-like and half photon-

like in character, and thus decays at a rate given by the average of the atom and cavity decays $\kappa' = (\kappa + \gamma)/2$. The width of each of the two peaks is set by the modified decay rate, κ'. Similarly, the height of each peak is set by the ratio $\kappa^2/(\kappa + \gamma)^2$. For three atomic transitions in the limits where there are two dominant transmission features, we expect the widths and heights of the transmission features to approach the single atomic transition case.

In Fig. 4.3, for the traces with the largest atom numbers, the widths of the transmission features are a few hundred kHz, in contrast to the theoretical prediction of $\kappa' = 24$ kHz. The lineshapes of the transmission features in Fig. 4.3 are sometimes multi-peaked and do not always look like the expected Lorentzian lineshapes. Furthermore, Figs. 4.3 and 4.4 provide a comparison between the heights of the bare cavity transmission feature and the coupled atom-cavity transmission features (note that the bare cavity transmission amplitude has been divided by 5 in Fig. 4.4). Compared to the height of the bare cavity transmission feature, the heights of the on-resonance ($\delta_{ac} = 0$) transmission features with atoms are a factor of about 3 smaller for the largest atom number and about 20 smaller for the smallest nonzero atom number. For the larger atom numbers (where there are two predominant peaks), we would expect a peak height of $\kappa^2/(\kappa + \gamma)^2 = 0.71$ relative to the bare cavity height.

We think the frequency-swept red 2D molasses beams are the primary cause of the observed broadening. In the following sections, I walk through an explanation of this broadening mechanism and introduce our experimental observations that support this mechanism.

4.4.1 Lattice Loading beams Cause Broadening

In typical cavity QED experiments, atoms are cooled and loaded into the cavity mode, and then any light not relevant for the experiment is turned off and the desired feature is measured. In our case, our goal is to observe a resolved steady-state vacuum Rabi splitting, so the beams that cool the atoms and load them into the lattice are on in steady-state.

Our 2D red molasses beams, 3D red molasses beams, and red vertical slowing beam all spatially overlap with the cavity mode, as shown in Fig. 2.11. The 3D red molasses beams and

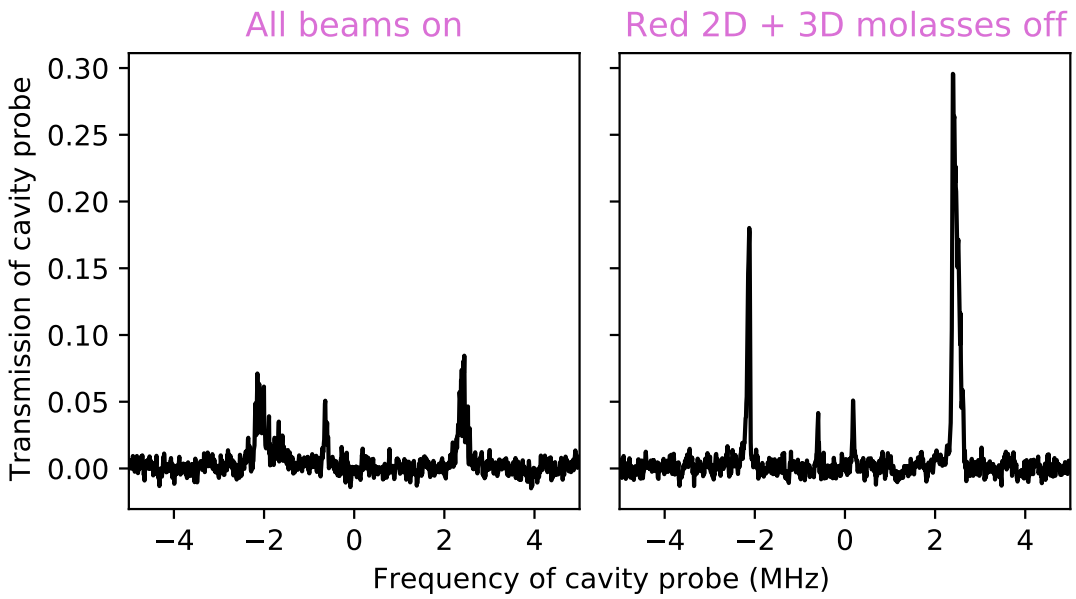

Figure 4.5: Broadening of the vacuum Rabi splitting from the red 2D and 3D molasses beams. Transmitted power as probe frequency is swept across the atomic resonance with all laser beams on (left) and with the red 2D and 3D molasses beams off (right). For the plot with the 2D and 3D molasses beams off, the probe starts sweeping when the beams are turned off and reaches the center of the splitting around 22 ms later. Qualitatively, the peaks appear narrower and taller with the red 2D and 3D molasses off. Additionally, with all beams on, we see two broad outer peaks and a single narrower central peak, but with the red 2D and 3D molasses beams off, we can resolve the fourth peak of the vacuum Rabi splitting.

red vertical slowing beam are constant in frequency, while the red 2D molasses beam sweeps in a sawtooth ramp in frequency. As shown in Fig. 2.13, the red vertical beam is detuned by about 3.75 MHz from the bare atomic resonance and the red 3D molasses beam is detuned about 2.5 MHz from the bare atomic resonance, while the red 2D molasses beams sweep to about 1.5 MHz from the bare cavity resonance. While this is far from the bare cavity resonance, it is near resonance with the ground to excited $m_F = -1$ state, which is detuned 1.2 MHz from the bare cavity resonance.

In Fig. 4.5, we show that the red 2D and 3D molasses beams contribute to the broadening of the vacuum Rabi splitting transmission features. We think the red 2D molasses is the primary culprit behind the broadening, but unfortunately we did not take this same trace with only the

red 2D molasses beams off and the apparatus is not currently working as the strontium oven is no longer operational. We compare the vacuum Rabi splitting transmission spectrum with all beams on to the spectrum where we turn the red 2D and 3D molasses off just prior to sweeping the probe across resonance. The probe starts sweeping when the beams are turned off and reaches the center of the splitting around 22 ms later. I also note that this data was taken with a stationary lattice and a reduced atom number to prevent collective light emission into the cavity via a mechanism that we do not yet understand.

Qualitatively, the peaks appear narrower and taller with the red 2D and 3D molasses off than with all the beams on. We are in the intermediate atom number regime where we expect to see four transmission peaks, as the splitting between the two outermost peaks is only a factor of 2 bigger than the total Zeeman splitting $2f_{ZS}$. With all the beams on, we see two broad outer peaks and a single narrower central peak. With the red 2D and 3D molasses beams off, we can observe all four transmission peaks, with two narrower and taller outer peaks and two narrow central peaks. The heights of the outer transmission peaks with the loading beams off are 0.2-0.3 times the height of the bare cavity mode, which is much closer to the expected amplitude of ~ 0.5 times the height of the bare cavity mode (from Fig. 4.2).

4.4.2 Physical Broadening Mechanism

How do the red 2D molasses beams cause broadening of the vacuum Rabi splitting? The red 2D molasses beams are detuned to the red of the bare atomic transition such that the only transition near resonance during the sweep is from the ground state $^1S_0$ to the $m_F = -1$ Zeeman level of the $^3P_1$ excited state manifold, as shown in Fig. 2.13. During the sweep, the red 2D molasses beams adiabatically transfer some atoms from the ground state to the $m_F = -1$ excited state. Each sweep lasts for 50 μs and occurs once every $\tau_{sweep} = 100$ μs, as the red 2D molasses alternates being toggled on/off with the red vertical slowing beam (described in more detail in Sec. 2.6.3).

Previously in this thesis, we made the approximation that there are few atoms in the excited state, in which case the collective vacuum Rabi splitting can be written as $\Omega = 2g\sqrt{N}$ (for a single

atomic transition interacting with a cavity). But with N_e atoms in the excited state and N_g atoms in the ground state, the collective vacuum Rabi splitting scales as $\Omega = 2g\sqrt{N_g - N_e}$. If there are initially N atoms in the ground state and the red 2D molasses beams adiabatically transfer N_{at} atoms to the $m_F = -1$ excited state, the vacuum Rabi splitting for this transition decreases, as $\Omega_- \propto \sqrt{N - 2N_{at}}$. This also affects the vacuum Rabi splitting component for the $m_F = 1$ and 0 excited states, as the number of atoms in the ground state decreases $\Omega_{0,+} \propto \sqrt{N - N_{at}}$.

Thus in a sweep of the red 2D molasses, the vacuum Rabi splitting decreases when the red 2D molasses beams pass through resonance with the $m_F = -1$ transition and atoms are transferred to the excited state. Then, atoms decay back to the ground state and the vacuum Rabi splitting relaxes to its original position. The excited state lifetime for this transition is 21 μs, but we are primarily concerned with the timescale τ_{relax} for the vacuum Rabi splitting transmission feature to relax back to within the cavity linewidth κ of the full value. If we are probing the cavity and are initially on resonance with a transmission feature with all the atoms in the ground state, when the atoms are transferred to the excited state, we would no longer see transmission, as the vacuum Rabi splitting has decreased. The timescale τ_{relax} is the time delay from when atoms are transferred to the excited state to when we start to see transmission through the cavity.

From the broadened transmission peak widths of a few hundred kHz and the splitting of the outermost vacuum Rabi splitting peaks of a few MHz, we estimate that $5 - 10$ % of the atoms are transferred to the excited state. Based on this estimate of the number of atoms transferred to the excited state, we calculate a time scale of $\tau_{relax} \sim 40 - 50$ μs for the vacuum Rabi splitting transmission feature to relax back to within the cavity linewidth κ of the full value.

In typical experimental configurations, it takes many $\tau_{sweep} = 100$ μs for the cavity probe to sweep in frequency across the broadened transmission feature. Thus we would expect to see oscillations in the transmitted power at τ_{sweep} where for a short time there is transmission, and then for τ_{relax} the transmission feature is not on resonance with the cavity probe, and then for a few tens of μs the transmission increases as the transmission resonance approaches the probe frequency.

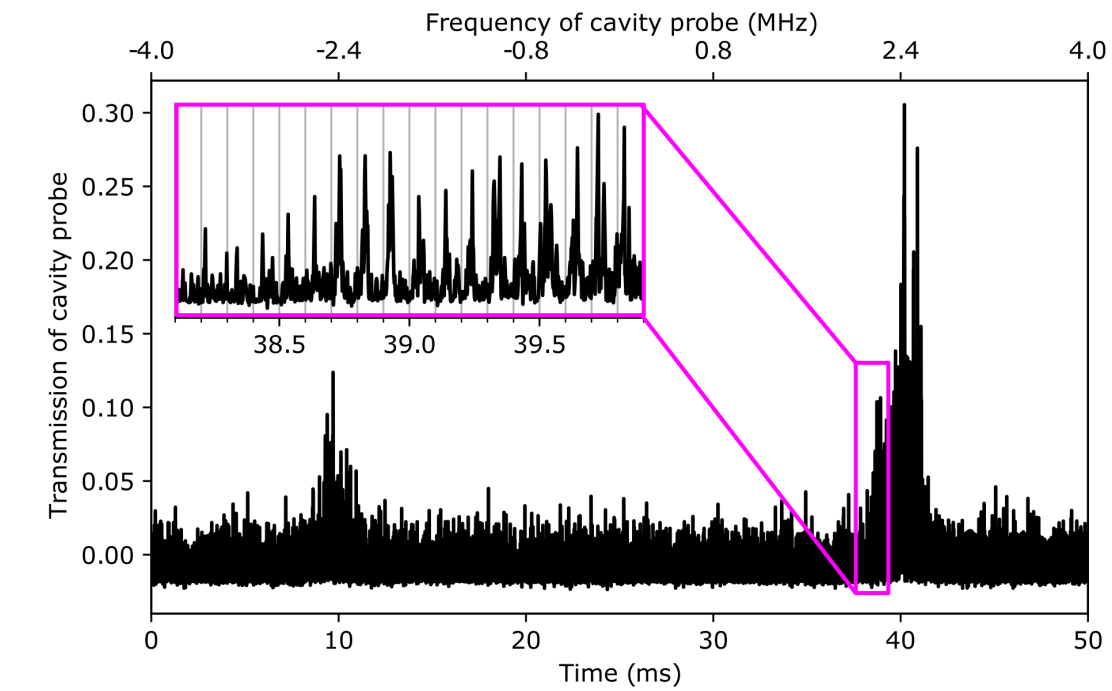

Figure 4.6: Periodic structure of the vacuum Rabi splitting at the red 2D molasses sweep frequency $\tau_{sweep} = 100$ μs. Transmitted power as probe frequency is swept across the atomic resonance with all beams on in steady-state, normalized to the bare cavity transmission. Compared to previous vacuum Rabi splitting plots in this thesis, here the low-pass filter corner frequency is much higher, ~ 100 kHz. The inset shows a zoom of the higher frequency transmission peak, with grey vertical lines every 100 μs. The axes of the inset are the same as those of the main plot. There are transmission peaks every 100 μs, consistent with the frequency sweep of the red 2D molasses causing time-broadening of the vacuum Rabi splitting.

In Fig. 4.6, we measure the transmitted power as the cavity probe frequency is swept across the atomic resonance with all beams on in steady-state. We observe oscillations in the transmitted probe power at the red 2D molasses sweep frequency $\tau_{sweep} = 100$ μs, within the vacuum Rabi splitting peaks. Compared to previous vacuum Rabi splitting plots in this thesis, in this Figure the low-pass filter corner frequency is much higher, ~ 100 kHz, enabling us to see this oscillation. The inset of Fig. 4.6 shows a zoom of the higher frequency transmission peak, with grey vertical lines every 100 μs. We observe transmission peaks every 100 μs, consistent with the frequency sweep of the red 2D molasses causing time-broadening of the vacuum Rabi splitting.

4.4.3 The Observed Broadening is Potentially a Feature

In the previous Sections, we demonstrated that the vacuum Rabi splitting is time-broadened by the red 2D molasses beams. In this Section, we will show that atoms transported by the lattice away from the loading region exhibit a decrease in broadening. Although the presence of broadening is generally undesirable, we actually view it as a potential feature of our system. For our future demonstration of superradiance, in order not to add broadening to the lasing transition, any atoms in the ground $^1S_0$ or excited $^3P_0$ states of the clock transition must either be unperturbed or broadened enough to not participate in superradiance. The ground state atoms in the loading region will be significantly broadened, preventing them from interacting with the superradiant light in the cavity, while atoms trapped in the lattice that have been transported to a quieter region of the cavity see a reduction in broadening and may be able to participate in superradiance.

The spatial extent of the time-broadening from the red 2D molasses beams is set by the spatial extent of the red 2D molasses beams. Thus, if we transport atoms in the travelling lattice away from the loading region where the red 2D and 3D molasses beams load atoms into the lattice, we expect to see a reduction in time-broadening of the vacuum Rabi splitting transmission features. To see this effect, we want the only atoms coupled to the cavity to be atoms in the lattice, far from the loading region.

However, we observe a background of atoms in the red 3D molasses cloud that are coupled to the cavity. We load atoms from the red 3D molasses into the lattice, so the red 3D molasses is intentionally centered on the cavity mode. With the lattice beams off, we observe a resolved vacuum Rabi splitting from atoms in the red 3D molasses cloud, albeit with a smaller splitting indicating a smaller atom number. If we turn off the loading beams, the number of background atoms in the cavity mode decreases to 49 % of the original atom number after waiting 20 ms and 4% after 50 ms.

To separate the atoms in the lattice that have traveled away from the loading region from the atoms in the loading region (whether background atoms or atoms in the lattice), we turn off

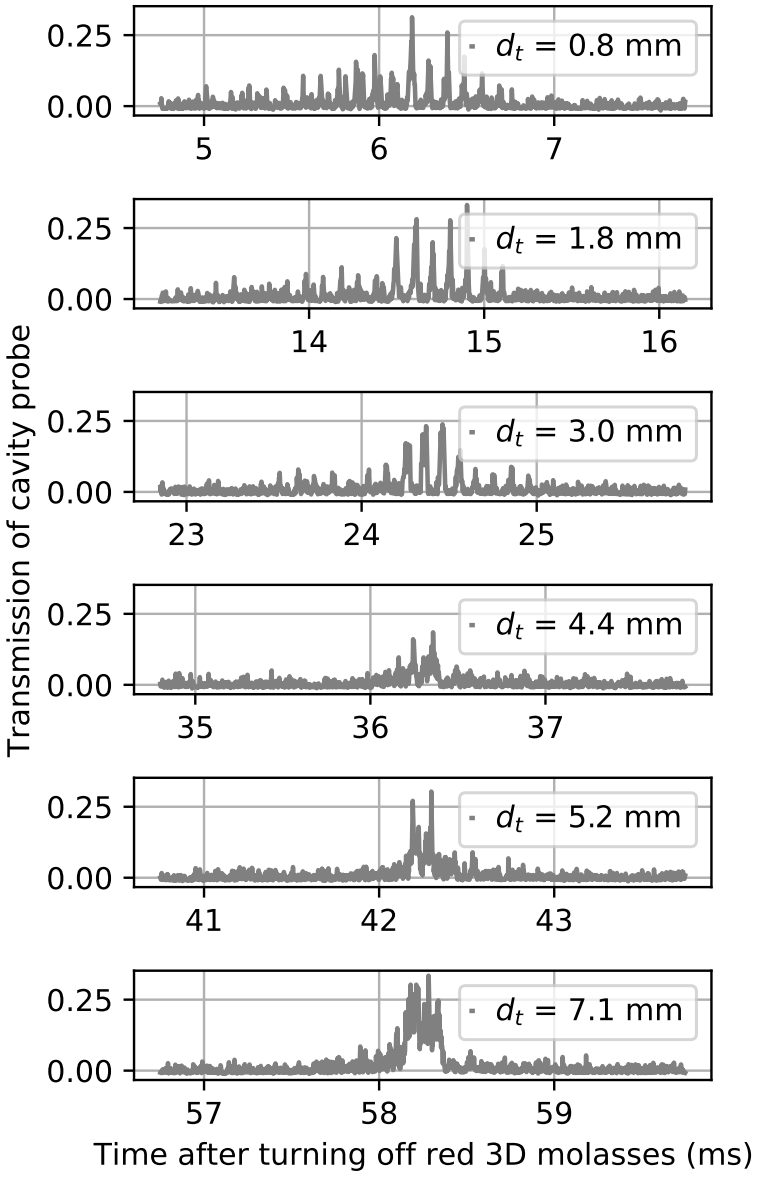

Figure 4.7: Reduction of broadening as atoms in the travelling lattice are transported away from the loading region of the cavity and background atoms in the red 3D molasses cloud fall away. Lower optical frequency transmission peak of the vacuum Rabi splitting for different delay times after turning off the red 3D molasses beams. Atoms are loaded into a travelling lattice $\delta_\ell = 2\pi \times 150$ kHz with no atom-cavity detuning $\delta_{ac} = 0$. In the top panels, we observe oscillations in the transmission peak at 100 μs, exactly how often the red 2D molasses sweeps across resonance with the $m_F = -1$ excited state. In the last panel, those oscillations are no longer present, as background atoms in the red 3D molasses have fallen away and atoms in the travelling lattice have been transported $d_t = 7.1$ mm by the lattice and have moved away from the frequency-swept red 2D molasses beams.

the red 3D molasses beams and look at the evolution of the vacuum Rabi splitting transmission

features in time. Turning off the red 3D molasses beams has two major effects: the red 3D molasses cloud falls out of the cavity mode (due to gravity), so the number of background atoms coupled to the cavity mode decreases, and atoms in the loading region that are trapped in the lattice are transported away from the loading region. Additionally, as we are no longer loading new atoms into the lattice, we observe a reduction of the atom number in the lattice due to a finite lattice lifetime (shown in Fig. 3.2).

To observe this phenomenon, we load atoms into a travelling lattice with $\delta_\ell = 2\pi \times 150$ kHz and $\delta_{ac} = 0$ and leave all the beams on in steady state except for the red 3D molasses beam, which is turned off at time $t = 0$. Then, we repeatedly sweep the cavity probe frequency across the vacuum Rabi splitting to observe how the transmission features change with time. Fig. 4.7 shows the lower optical frequency transmission peak for different time delays from turning off the red 3D molasses beams.

In the top panels of Fig. 4.7, we observe oscillations in the vacuum Rabi splitting transmission peak at 100 μs, exactly how often the red 2D molasses sweeps across resonance with the $m_F = -1$ excited state. By the last panel, those oscillations are no longer present, indicating that the atoms have been transported to a "quieter" region of the cavity where they no longer see the frequency-swept red 2D molasses beams. For the last panel of Fig. 4.7, the transmission peak occurs around 58 ms after turning red 3D molasses beams off. At this delay time, we expect that around 0.02 of the background atoms in the red 3D molasses remain in the cavity mode, so the primary contribution to the vacuum Rabi splitting is from atoms trapped in the lattice. The atoms trapped in the lattice have been transported 7.1 mm by the travelling lattice and have moved away from the loading region, which has a full width half maximum along the lattice of 2.8 mm.

In Fig. 4.8, we fit the transmission features of Fig. 4.7 to a Lorentzian to extract the peak width. We observe that as the background atoms leave the cavity mode and as atoms trapped in the lattice travel away from the red 2D molasses beams, the width of the transmission feature approaches $1/2(\kappa+\gamma)$, the width of a vacuum Rabi splitting transmission feature one would expect with $\delta_{ac} = 0$ and a single atomic transition coupled to a cavity mode. Thus atoms transported by

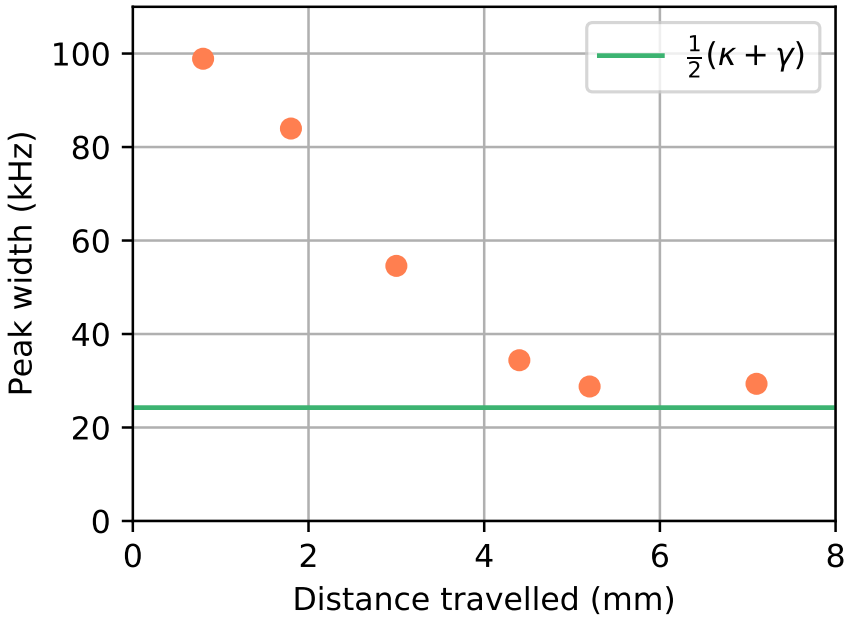

Figure 4.8: Reduction of broadening as atoms in the travelling lattice are transported away from the loading region, part 2. Peak width extracted from fitting the transmission features of Fig. 4.7 to a Lorentzian function. We observe that as the background atoms leave the cavity mode and as atoms trapped in the lattice travel away from the red 2D molasses beams, the width of the transmission feature approaches $(\kappa+\gamma)/2$ (shown in green), the width of a vacuum Rabi splitting transmission feature one would expect with $\delta_{ac} = 0$ and a single atomic transition coupled to a cavity mode.

the lattice away from the loading region exhibit a decrease in broadening.

4.5 Demonstration of a Continuous Vacuum Rabi Splitting for More than Twenty Minutes

Finally, we want to demonstrate the *steady-state* aspect of continuous strong collective coupling. In typical cavity QED experiments, atoms are cooled and loaded into the cavity mode, and then the desired feature is measured. The rate of atom loss dictates the length of the measurement before the atom number must be replenished. After the measurement, the experimental cycle starts again and fresh atoms are cooled and loaded into the cavity mode.

In our experiment, we continuously load atoms into a travelling lattice, as described in the

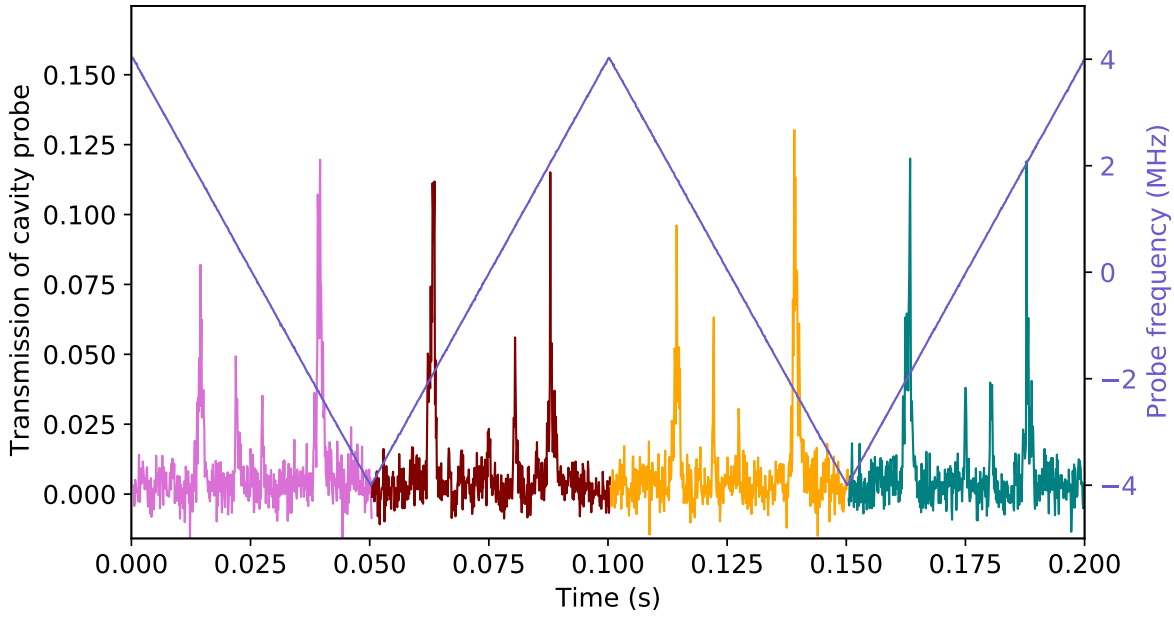

Figure 4.9: Transmitted power as the probe frequency (purple) is swept across the atomic resonance and atoms are continuously loaded into a travelling lattice with $\delta_\ell = 2\pi \times 100$ kHz. The transmission is normalized to the bare cavity resonance and is shown in four different colors (pink, brown, yellow, and green) in order to highlight each sweep of the cavity probe. We observe a vacuum Rabi splitting every time the probe sweeps across the atomic resonance (every 50 ms). We are in the regime of intermediate atom number, where we observe four vacuum Rabi splitting peaks, as shown in Fig. 4.2. This is a short subset of the almost 1400 second long continuous vacuum Rabi splitting data that is plotted in Fig. 4.10.

experimental apparatus section. Our measurement time is instead set by the length of time all the lasers stay locked, typically on the order of hours, or the patience of the graduate student operating the apparatus, whichever comes first.

To demonstrate a continuous vacuum Rabi splitting, we continuously load atoms into a travelling lattice with $\delta_\ell = 2\pi \times 100$ kHz and leave all loading and cooling beams on in steady-state. We repeatedly sweep the frequency of the cavity probe in a symmetric triangle ramp across atomic resonance with a sweep rate of 10 Hz. Thus every 100 ms, the cavity probe sweeps across the vacuum Rabi splitting twice, once on the upsweep of the triangle ramp and once on the down-sweep of the triangle ramp, as shown in Fig. 4.9.

The experimental control apparatus triggers the frequency sweep of the cavity probe, records

the transmission of the cavity probe (measured by a single photon counting module) for sixty seconds, takes about one second to save the data, and then immediately starts again. Everything else is unchanged during the sequence and operates continuously.

Fig. 4.9 shows a short subset of a 23 minute long continuous vacuum Rabi splitting measurement (later plotted in plotted in Fig. 4.10). We plot the transmitted power as the probe frequency is swept across the atomic resonance and observe a vacuum Rabi splitting every 50 ms (every frequency sweep). Atoms are continuously loaded into a travelling lattice with $\delta_\ell = 2\pi \times 100$ kHz. We are in the regime of intermediate atom number, where we observe four vacuum Rabi splitting peaks, as described in Fig. 4.2.

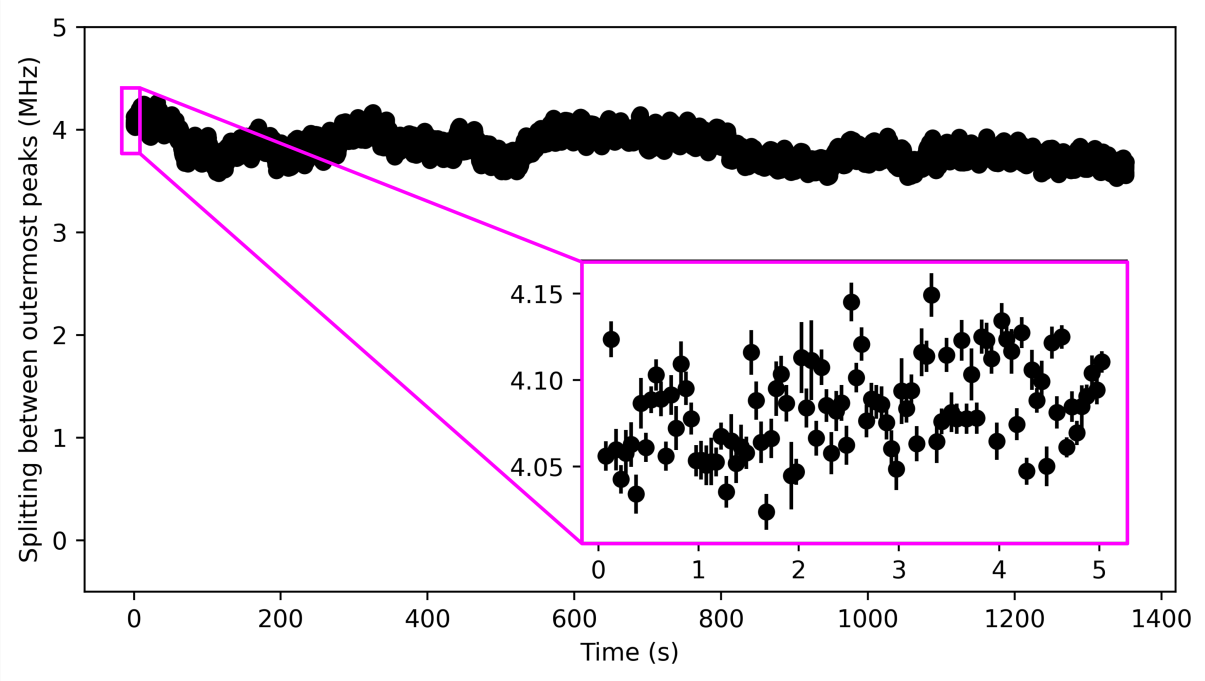

Figure 4.10: Demonstration of a continuous vacuum Rabi splitting for more than twenty minutes. Fitted frequency splitting between the outermost peaks of the vacuum Rabi splitting over a 23 minute measurement. We observe a vacuum Rabi splitting every time the probe sweeps across the atomic resonance (every 50 ms), as shown in Fig. 4.9. This corresponds to a measured frequency splitting once every 50 ms, as shown in the inset. The inset has the same axes as the main plot.

Fig. 4.10 shows the fitted frequency splitting between the outermost peaks of the vacuum Rabi splitting versus time over a 23 minute measurement. As shown in the inset, there is a vacuum Rabi

splitting measurement once every 50 ms over the whole measurement window (with the exception of a 1 second break every 60 s to save the data).

To convince a skeptical reader that we are truly observing a steady-state signal, I will compare these time scales with atomic loss rates in our experiment. The stationary lattice ($\delta_\ell = 0$) lifetime is 277 ± 7 ms. For $\delta_\ell = 2\pi \times 100$ kHz, the travelling lattice lifetime is 140 ± 20 ms (for a 150 μK trap, shown in Fig. 3.2). Collisions with the background gas are likely the dominant loss mechanism for the stationary lattice, as we estimate the vacuum limited lifetime is around 300 ms (see Sec. 2.2 for more details), and parametric heating is likely the dominant loss mechanism for the travelling lattice (see Sec. 2.6.4 for more details). If we were not continuously loading new atoms into the lattice, in 140 ms our atom number would have decreased by $1/e$, or equivalently the vacuum Rabi splitting would have decreased by $\sqrt{1/e} \sim 0.6$. Twenty minutes later, we definitely would not be able to resolve a vacuum Rabi splitting.

Could we be sneakily loading atoms into the lattice between frequency sweeps of the cavity probe? It would be very difficult, as there is about a 25 ms delay between the last vacuum Rabi splitting peak of one sweep and the first peak of the next sweep (shown in Fig. 4.9). For comparison, the pulsed Sr apparatus in our lab operates at a typical experimental cycle time of ~ 1 Hz, where every second new atoms are loaded into a blue 3D MOT, transferred to a red 3D MOT, and then loaded into the lattice. The length of the experimental cycle time is dominated by the ~ 500 ms it takes to accumulate atoms in the blue 3D MOT.

In summary, we have demonstrated the first steady state vacuum Rabi splitting on a narrow linewidth atomic transition.

Chapter 5

Conclusion and Future Outlook

In this thesis, I have demonstrated two major milestones towards the creation of a superradiant laser with kilosecond coherence times: a pulsed superradiant laser on a mHz linewidth transition and continuous loading and strong collective coupling of atoms to a high finesse optical cavity. The pulsed superradiant laser is the most precise active absolute frequency standard realized to date. The continuous atomic source is the first to demonstrate steady-state strong collective coupling on a narrow linewidth transition, possibly the first to demonstrate deterministic transport of atoms around a cavity, and represents the second continuous cold atomic source with high phase space density in the world.

In this chapter, I will give a perspective on the applications of a superradiant laser and present what I think is a promising path to realize a steady-state narrow linewidth superradiant laser.

5.1 Applications of a Superradiant Laser

A continuous wave superradiant laser could dramatically improve precision measurements and research in a broad range of applications. It would not only allow for robust frequency references that could operate outside of the extremely low vibration environment of a precision laser laboratory, but also improve the short-term stability of the best atomic frequency references by two orders of magnitude and outperform reference cavities at long times as well. A superradiant laser could become a high-bandwidth precision measurement tool with a fractional instability of potentially 7×10^{-18} in one second (see Section 1.3), almost a factor of 5 better than current state-

of-the-art values of 3.1×10^{-17} at 1 s reported for synchronous comparisons in a three-dimensional (3D) lattice clock [40] and 4.8×10^{-17} at 1 s for an anti-synchronous comparison between two independent clocks [45].

The ultra-precise measurement capability afforded by a superradiant laser could have a dramatic impact on a broad range of measurements and research, from probing gravity [152], detecting gravity waves [153], and defining the second [154, 47] to quantum computation [155] and searches for physics beyond the standard model [156, 157]. A continuous superradiant laser has a much broader application than just clocks: the combination of a superradiant laser and a frequency comb could lead to improved measurement capability in wavelengths all the way from infrared to XUV [158, 159, 45].

Furthermore, the techniques I developed in creating a continuous superradiant laser could be applied to other research pursuits. For example, the development of continuous loading techniques could be applied to matter wave lasers for inertial sensing [160], determination of fundamental constants [154, 47, 156], and tests of fundamental physics [157]. Additionally, the experimental superradiant atom-cavity system is ideal for proof-of-principle experiments to generate entanglement between strontium atoms for dramatically reducing atom shot noise in clocks and interferometers [133].

5.2 Towards a Steady-State Superradiant Laser

I demonstrated two major milestones towards the creation of a superradiant laser with kilosecond coherence times: lasing on a mHz optical transition and an atom source with continuous strong collective coupling. The next step will be to combine these two advances to realize a steady-state narrow linewidth superradiant laser. There are two main next steps: switching from ^{88}Sr to ^{87}Sr and preparing the atoms in the excited state of the clock transition.

Switching isotopes involves adjusting frequencies to account for isotope shifts, applying more tones to account for the non-zero nuclear spin, and adjusting systems to account for fewer atoms (because of the relative isotopic abundance). I expect of the two next steps, this will be more

straight forward.

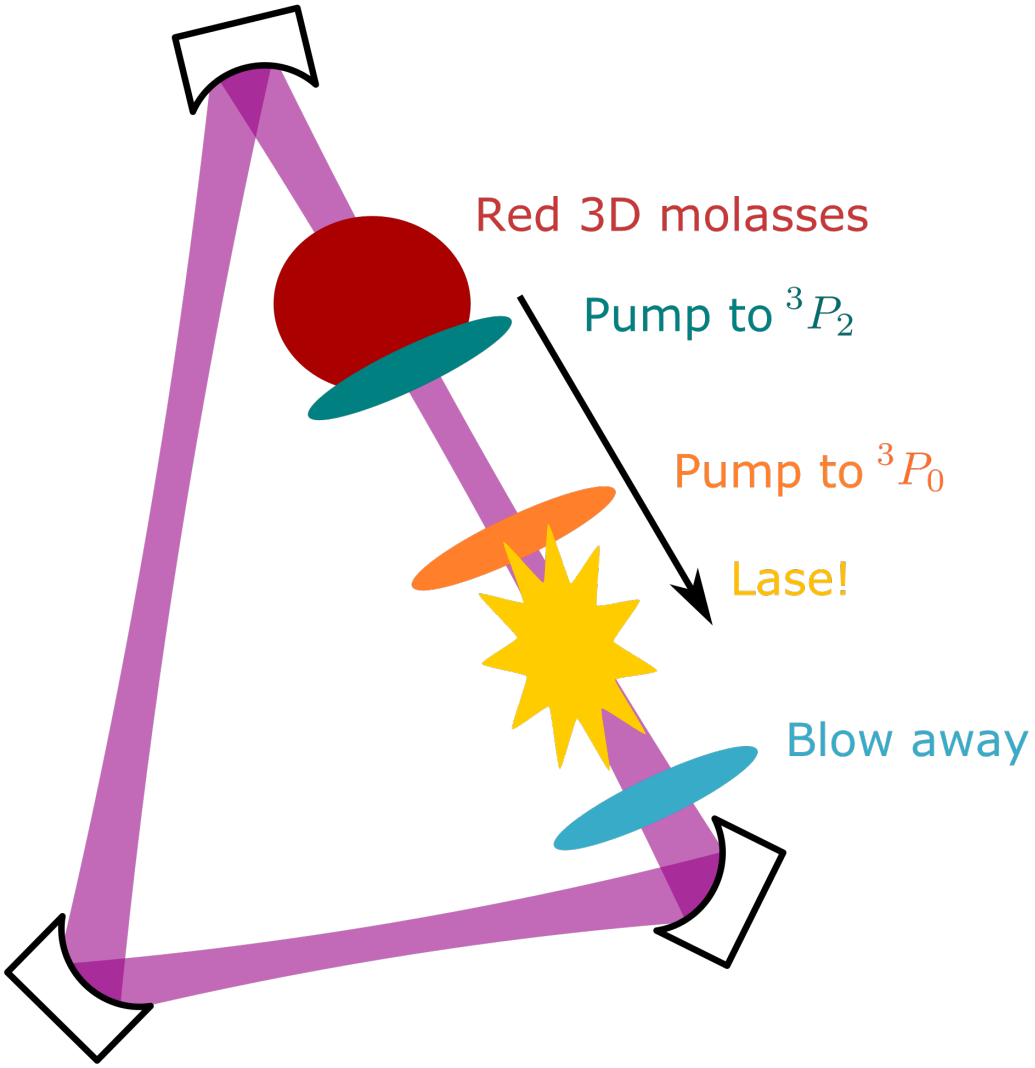

Figure 5.1: A promising approach to excite atoms for steady-state superradiance: load the atoms into a travelling lattice, pump the atoms to a dark state ($^3P_2$) while they are in the "noisy" loading region, transport them over to a "quieter" lasing region, and then pump the atoms to a higher excited state ($^3S_1$) from which they can spontaneously decay to the excited state of the mHz transition ($^3P_0$). Once they reach the excited state, the atoms can interact with the superradiant light in the cavity mode and will be stimulated to "lase" by emitting a photon into the cavity mode. All pumping and blowaway beams are incident on the cavity from the side.

When pumping atoms to the excited state of the clock transition, we must be careful to

avoid writing the phase noise of our "noisy" pump laser onto the atoms. This requirement dictates that we must prepare the atoms all the way in the excited state, with no coherence length (no projection onto the equator of the Bloch sphere other than shot noise). There are a couple of ways to accomplish this: adiabatic transfer to the excited state, which transfers the atoms to the excited state with unit probability, or decay from a higher excited state via spontaneous emission, which scrambles the atomic phase. In our demonstration of mHz superradiance, we adiabatically transferred the atoms from the ground state to the excited state and then destroyed any remaining phase coherence between the ground and the excited state (due to imperfect adiabatic transfer) by scattering blue light off the ground state [66]. In Matt's realization of superradiance on the 7.5 kHz transition, he demonstrated rempumping from the ground state $^1S_0$ to the higher-lying excited state $^3S_1$, via the $m_F = \pm 1$ Zeeman sublevels of $^3P_1$. From $^3S_1$, atoms could decay back to the desired excited state, $m_F = 0$ of $^3P_1$ [56].

I present a scheme to continuously prepare atoms in the excited state of the clock transition in Fig. 5.1. After the atoms are trapped and cooled within the lattice, but before they leave the red 3D molasses loading region, the atoms are transferred to a metastable dark state ($^3P_2$) and then transported over to a "quieter" lasing region by the travelling lattice. When they reach the lasing region, repump beams transfer the atoms to a higher excited state ($^3S_1$) from which they can spontaneously decay to the excited state ($^3P_0$). Once they reach the excited state, the atoms can interact with the superradiant light in the cavity mode and will be stimulated to emit a photon. The velocity of the moving lattice should be sufficiently high relative to the cavity linewidth that one direction of circulating light is shifted off resonance with the cavity and the superradiant light propagates in a well-defined direction.

The lasers needed to pump the atoms from $^1S_0$ to $^3P_2$ (in the presence of the red 3D molasses at 689 nm) are 679 and 688 nm and from $^3P_2$ to $^3P_0$ are 688 and 707 nm. We already use the 679 and 707 nm lasers to repump atoms in the blue 2D MOT and have the third repump laser at 688 nm available in our lab.

The final step is to blow atoms out of the lattice after they have emitted a photon into the

cavity mode. This is to both protect the high finesse mirrors from being coated with strontium and to ensure that we can maintain inversion by removing extra ground state atoms.

An advantage of this approach is that atoms are never in the ground or excited states of the lasing transition unless they are strongly dephased or participating in superradiance. Another potential approach is to adiabatically transfer the atoms to the excited state by using the linear slope of a gaussian beam to generate a linear ac stark shift that the atoms move through at a velocity set by the travelling lattice, adiabatically transferring the atoms to the excited state. In this approach, there would need to be a knife edge on the frequency shifting beam in order to prevent shifts to atoms once they have reached the excited state.

I anticipate the major potential difficulties to achieving continuous wave superradiance are related to dephasing of the clock transition, whether by inhomogeneous magnetic fields, scattered light from the red 3D molasses, or another mechanism. If it is difficult to reach the continuous atom number threshold for lasing, one could start out by demonstrating pulsed superradiance on the mHz transition and move the atoms around the cavity mode to map out the frequency shifts.

I am confident that realizing a continuous wave superradiant laser will be an exciting and unique challenge and I look forward to seeing the next steps of this experiment!

Bibliography

[1] Harold J Metcalf and Peter Straten. Laser cooling and trapping of neutral atoms. Wiley Online Library, 2007.

[2] Mike H Anderson, Jason R Ensher, Michael R Matthews, Carl E Wieman, Eric A Cornell, et al. Observation of Bose-Einstein condensation in a dilute atomic vapor. Science, 269(5221):198–201, 1995.

[3] Kendall B Davis, M-O Mewes, Michael R Andrews, NJ Van Druten, DS Durfee, DM Kurn, and Wolfgang Ketterle. Bose-Einstein condensation in a gas of sodium atoms. Physical Review Letters, 75(22):3969, 1995.

[4] Adam M Kaufman, Brian J Lester, and Cindy A Regal. Cooling a single atom in an optical tweezer to its quantum ground state. Physical Review X, 2(4):041014, 2012.

[5] Luigi De Marco, Giacomo Valtolina, Kyle Matsuda, William G. Tobias, Jacob P. Covey, and Jun Ye. A degenerate fermi gas of polar molecules. Science, 363(6429):853–856, 2019.

[6] Ian D. Leroux, Monika H. Schleier-Smith, and Vladan Vuletić. Implementation of cavity squeezing of a collective atomic spin. Phys. Rev. Lett., 104:073602, Feb 2010.

[7] Markus Greiner, Olaf Mandel, Tilman Esslinger, Theodor W Hänsch, and Immanuel Bloch. Quantum phase transition from a superfluid to a mott insulator in a gas of ultracold atoms. Nature, 415(6867):39–44, 2002.

[8] Kihwan Kim, M-S Chang, Simcha Korenblit, Rajibul Islam, Emily E Edwards, James K Freericks, G-D Lin, L-M Duan, and Christopher Monroe. Quantum simulation of frustrated ising spins with trapped ions. Nature, 465(7298):590–593, 2010.

[9] Onur Hosten, Nils J Engelsen, Rajiv Krishnakumar, and Mark A Kasevich. Measurement noise 100 times lower than the quantum-projection limit using entangled atoms. Nature, 529(7587):505, 2016.

[10] Kevin C Cox, Graham P Greve, Joshua M Weiner, and James K Thompson. Deterministic squeezed states with collective measurements and feedback. Physical Review Letters, 116(9):093602, 2016.

[11] Waseem S Bakr, Jonathon I Gillen, Amy Peng, Simon Fölling, and Markus Greiner. A quantum gas microscope for detecting single atoms in a hubbard-regime optical lattice. Nature, 462(7269):74–77, 2009.

[12] William B. Cairncross, Daniel N. Gresh, Matt Grau, Kevin C. Cossel, Tanya S. Roussy, Yiqi Ni, Yan Zhou, Jun Ye, and Eric A. Cornell. Precision measurement of the electron's electric dipole moment using trapped molecular ions. Phys. Rev. Lett., 119:153001, Oct 2017.

[13] Jacob Baron, Wesley C Campbell, David DeMille, John M Doyle, Gerald Gabrielse, Yulia V Gurevich, Paul W Hess, Nicholas R Hutzler, Emil Kirilov, Ivan Kozyryev, et al. Order of magnitude smaller limit on the electric dipole moment of the electron. Science, page 1248213, 2013.

[14] D Hanneke, S Fogwell, and G Gabrielse. New measurement of the electron magnetic moment and the fine structure constant. Physical Review Letters, 100(12):120801, 2008.

[15] Simon Rainville, James K Thompson, Edmund G Myers, John M Brown, Maynard S Dewey, Ernest G Kessler, Richard D Deslattes, Hans G Börner, Michael Jentschel, Paolo Mutti, et al. World year of physics: A direct test of $E = mc^2$. Nature, 438(7071):1096–1097, 2005.

[16] Savas Dimopoulos, Peter W Graham, Jason M Hogan, and Mark A Kasevich. Testing general relativity with atom interferometry. Physical Review Letters, 98(11):111102, 2007.

[17] Michael J Martin. Quantum metrology and many-body physics: pushing the frontier of the optical lattice clock. PhD thesis, University of Colorado at Boulder, 2013.

[18] X. Zhang, M. Bishof, S. L. Bromley, C. V. Kraus, M. S. Safronova, P. Zoller, A. M. Rey, and J. Ye. Spectroscopic observation of SU(N)-symmetric interactions in Sr orbital magnetism. Science, 345(6203):1467–1473, 2014.

[19] A. Derevianko and M. Pospelov. Hunting for topological dark matter with atomic clocks. Nature Physics, 10(12):933–936, 2014.

[20] A. Derevianko. Atomic clocks and dark-matter signatures. Journal of Physics: Conference Series, 723(1):012043, 2016.

[21] M. S. Safronova, D. Budker, D. DeMille, Derek F. Jackson Kimball, A. Derevianko, and Charles W. Clark. Search for new physics with atoms and molecules. Rev. Mod. Phys., 90:025008, Jun 2018.

[22] M. Zych, F. Costa, I. Pikovski, and Č. Brukner. Quantum interferometric visibility as a witness of general relativistic proper time. Nature Communications, 2:505, 2011.

[23] I. Pikovski, M. Zych, F. Costa, and Č. Brukner. Universal decoherence due to gravitational time dilation. Nature Physics, 11:668–672, 2015.

[24] E. Castro Ruiz, F. Giacomini, and Č. Brukner. Entanglement of quantum clocks through gravity. Proceedings of the National Academy of Sciences, 114(12):E2303–E2309, 2017.

[25] R. H. Dicke. Coherence in spontaneous radiation processes. Phys. Rev., 93(1):99, Jan 1954.

[26] Michel Gross and Serge Haroche. Superradiance: An essay on the theory of collective spontaneous emission. Physics reports, 93(5):301–396, 1982.

[27] N Skribanowitz, IP Herman, JC MacGillivray, and MS Feld. Observation of dicke superradiance in optically pumped HF gas. Phys. Rev. Lett., 30(8):309, 1973.

[28] Y Kaluzny, P Goy, M Gross, JM Raimond, and S Haroche. Observation of self-induced rabi oscillations in two-level atoms excited inside a resonant cavity: the ringing regime of superradiance. Phys. Rev. Lett., 51(13):1175, 1983.

[29] A. Goban, C.-L. Hung, J. D. Hood, S.-P. Yu, J. A. Muniz, O. Painter, and H. J. Kimble. Superradiance for atoms trapped along a photonic crystal waveguide. Phys. Rev. Lett., 115:063601, Aug 2015.

[30] Shoichi Okaba, Deshui Yu, Luca Vincetti, Fetah Benabid, and Hidetoshi Katori. Superradiance from lattice-confined atoms inside hollow core fibre. Communications Physics, 2(1):136, 2019.

[31] Je-Hyung Kim, Shahriar Aghaeimeibodi, Christopher J. K. Richardson, Richard P. Leavitt, and Edo Waks. Super-radiant emission from quantum dots in a nanophotonic waveguide. Nano Letters, 18(8):4734–4740, 08 2018.

[32] D. Meiser and M. J. Holland. Steady-state superradiance with alkaline-earth-metal atoms. Phys. Rev. A, 81(3):033847, Mar 2010.

[33] D. Meiser, Jun Ye, D. R. Carlson, and M. J. Holland. Prospects for a millihertz-linewidth laser. Phys. Rev. Lett., 102(16):163601–163604, Apr 2009.

[34] M Schioppo, RC Brown, WF McGrew, N Hinkley, RJ Fasano, K Beloy, TH Yoon, Gianmaria Milani, D Nicolodi, JA Sherman, et al. Ultrastable optical clock with two cold-atom ensembles. Nature Photonics, 2016.

[35] B. J. Bloom, T. L. Nicholson, J. R. Williams, S. L. Campbell, M. Bishof, X. Zhang, W. Zhang, S. L. Bromley, and J. Ye. An optical lattice clock with accuracy and stability at the 10^{-18} level. Nature, 506:71, February 2014.

[36] Ichiro Ushijima, Masao Takamoto, Manoj Das, Takuya Ohkubo, and Hidetoshi Katori. Cryogenic optical lattice clocks. Nat. Photon., 9:185, Feb 2015.

[37] J. Lodewyck, S. Bilicki, E. Bookjans, J.L. Robyr, C. Shi, G. Vallet, R. Le Targat, D. Nicolodi, Y. Le Coq, J. Guéna, et al. Optical to microwave clock frequency ratios with a nearly continuous strontium optical lattice clock. Metrologia, 53(4):1123, 2016.

[38] C. Grebing, A. Al-Masoudi, S. Dörscher, S. Häfner, V. Gerginov, S. Weyers, B. Lipphardt, F. Riehle, U. Sterr, and C. Lisdat. Realization of a timescale with an accurate optical lattice clock. Optica, 3(6):563–569, 2016.

[39] M. Schioppo, R. Brown, W. McGrew, N. Hinkley, R. Fasano, K. Beloy, T.H. Yoon, G. Milani, D. Nicolodi, J.A. Sherman, et al. Ultrastable optical clock with two cold-atom ensembles. Nature Photonics, 11(1):48, 2017.

[40] S. L. Campbell, R. B. Hutson, G. E. Marti, A. Goban, N. Darkwah Oppong, R. L. McNally, L. Sonderhouse, J. M. Robinson, W. Zhang, B. J. Bloom, and J. Ye. A fermi-degenerate three-dimensional optical lattice clock. Science, 358(6359):90–94, 2017.

[41] T.L. Nicholson, S.L. Campbell, R.B. Hutson, G.E. Marti, B.J. Bloom, R.L. McNally, W. Zhang, M.D. Barrett, M.S. Safronova, G.F. Strouse, et al. Systematic evaluation of an atomic clock at 2×10^{-18} total uncertainty. Nature Communications, 6, 2015.

[42] C.W. Chou, D.B. Hume, J.C.J. Koelemeij, D.J. Wineland, and T. Rosenband. Frequency comparison of two high-accuracy Al^+ optical clocks. Phys. Rev. Lett., 104(7):070802, 2010.

[43] A. Ludlow, M. Boyd, J. Ye, E. Peik, and P. Schmidt. Optical atomic clocks. Rev. Mod. Phys., 87:637–701, Jun 2015.

[44] C. Lisdat, G. Grosche, N. Quintin, C. Shi, S.M.F. Raupach, C. Grebing, D. Nicolodi, F. Stefani, A. Al-Masoudi, S. Dörscher, et al. A clock network for geodesy and fundamental science. Nature Communications, 7, 2016.

[45] E. Oelker, R. B. Hutson, C. J. Kennedy, L. Sonderhouse, T. Bothwell, A. Goban, D. Kedar, C. Sanner, J. M. Robinson, G. E. Marti, D. G. Matei, T. Legero, M. Giunta, R. Holzwarth, F. Riehle, U. Sterr, and J. Ye. Demonstration of 4.8×10^{-17} stability at 1 s for two independent optical clocks. Nature Photonics, 2019.

[46] John M. Robinson, Eric Oelker, William R. Milner, Wei Zhang, Thomas Legero, Dan G. Matei, Fritz Riehle, Uwe Sterr, and Jun Ye. Crystalline optical cavity at 4 K with thermal-noise-limited instability and ultralow drift. Optica, 6(2):240–243, Feb 2019.

[47] Y. Y. Jiang, A. D. Ludlow, N. D. Lemke, R. W. Fox, J. A. Sherman, L.-S. Ma, and C. W. Oates. Making optical atomic clocks more stable with 10^{-16}-level laser stabilization. Nat. Photon., 5:158, Mar 2011.

[48] B. C. Young, F. C. Cruz, W. M. Itano, and J. C. Bergquist. Visible lasers with subhertz linewidths. Phys. Rev. Lett., 82(19):3799–3802, May 1999.

[49] Kenji Numata, Amy Kemery, and Jordan Camp. Thermal-noise limit in the frequency stabilization of lasers with rigid cavities. Phys. Rev. Lett., 93(25):250602, Dec 2004.

[50] Mark Notcutt, Long-Sheng Ma, Andrew D Ludlow, Seth M Foreman, Jun Ye, and John L Hall. Contribution of thermal noise to frequency stability of rigid optical cavity via hertz-linewidth lasers. Phys. Rev. A, 73(3):031804, 2006.

[51] H. M. Goldenberg, D. Kleppner, and N. F. Ramsey. Atomic hydrogen maser. Phys. Rev. Lett., 5:361–362, Oct 1960.

[52] J.G. Bohnet, Z. Chen, J.M. Weiner, D. Meiser, M.J. Holland, and J.K. Thompson. A steady-state superradiant laser with less than one intracavity photon. Nature, 484(7392):78–81, 2012.

[53] Justin G Bohnet, Zilong Chen, Joshua M Weiner, Kevin C Cox, and James K Thompson. Linear-response theory for superradiant lasers. Physical Review A, 89(1):013806, 2014.

[54] Justin G Bohnet, Zilong Chen, Joshua M Weiner, Kevin C Cox, and James K Thompson. Active and passive sensing of collective atomic coherence in a superradiant laser. Phys. Rev. A, 88(1):013826, 2013.

[55] J. G. Bohnet, Z. Chen, J. M. Weiner, K. C. Cox, and J. K. Thompson. Relaxation oscillations, stability, and cavity feedback in a superradiant raman laser. Phys. Rev. Lett., 109:253602–253606, Dec 2012.

[56] Matthew A. Norcia and James K. Thompson. Cold-strontium laser in the superradiant crossover regime. Phys. Rev. X, 6:011025, Mar 2016.

[57] Torben Laske, Hannes Winter, and Andreas Hemmerich. Pulse delay time statistics in a superradiant laser with calcium atoms. Phys. Rev. Lett., 123:103601, Sep 2019.

[58] Stefan A. Schäffer, Mikkel Tang, Martin R. Henriksen, Asbjørn A. Jørgensen, Bjarke T. R. Christensen, and Jan W. Thomsen. Lasing on a narrow transition in a cold thermal strontium ensemble. Phys. Rev. A, 101:013819, Jan 2020.

[59] Matthew N Winchester, Matthew A Norcia, Julia RK Cline, and James K Thompson. Magnetically induced optical transparency on a forbidden transition in strontium for cavity-enhanced spectroscopy. Physical Review Letters, 118(26):263601, 2017.

[60] M.A. Norcia, J.R.K. Cline, J.P. Bartolotta, M.J. Holland, and J.K. Thompson. Narrow-line laser cooling by adiabatic transfer. New Journal of Physics, 2018.

[61] Juan A Muniz, Matthew A Norcia, Julia RK Cline, and James K Thompson. A robust narrow-line magneto-optical trap using adiabatic transfer. arXiv preprint arXiv:1806.00838, 2018.

[62] Matthew A. Norcia, Julia R. K. Cline, and James K. Thompson. Role of atoms in atomic gravitational-wave detectors. Phys. Rev. A, 96:042118, Oct 2017.

[63] Matthew A. Norcia, Robert J. Lewis-Swan, Julia R. K. Cline, Bihui Zhu, Ana M. Rey, and James K. Thompson. Cavity-mediated collective spin-exchange interactions in a strontium superradiant laser. Science, 361(6399):259–262, 2018.

[64] Juan A. Muniz, Dylan J. Young, Julia R. K. Cline, and James K. Thompson. Cavity-qed measurements of the ^{87}Sr millihertz optical clock transition and determination of its natural linewidth. Phys. Rev. Research, 3:023152, May 2021.

[65] Juan A. Muniz, Diego Barberena, Robert J. Lewis-Swan, Dylan J. Young, Julia R. K. Cline, Ana Maria Rey, and James K. Thompson. Exploring dynamical phase transitions with cold atoms in an optical cavity. Nature, 580(7805):602–607, Apr 2020.

[66] Matthew A Norcia, Matthew N Winchester, Julia RK Cline, and James K Thompson. Superradiance on the millihertz linewidth strontium clock transition. Science advances, 2(10):e1601231, 2016.

[67] Matthew A. Norcia, Julia R. K. Cline, Juan A. Muniz, John M. Robinson, Ross B. Hutson, Akihisa Goban, G. Edward Marti, Jun Ye, and James K. Thompson. Frequency measurements of superradiance from the strontium clock transition. Phys. Rev. X, 8:021036, May 2018.

[68] M.D. Swallows, M.J. Martin, M. Bishof, C. Benko, Y. Lin, S. Blatt, A.M. Rey, and J. Ye. Operating a ^{87}Sr optical lattice clock with high precision and at high density. IEEE Transactions on Ultrasonics, Ferroelectrics, and Frequency Control, 59(3):416–425, March 2012.

[69] M. Bishof, X. Zhang, M. J. Martin, and J. Ye. Optical spectrum analyzer with quantum-limited noise floor. Phys. Rev. Lett., 111:093604, Aug 2013.

[70] H. M. Goldenberg, D. Kleppner, and N. F. Ramsey. Atomic hydrogen maser. Phys. Rev. Lett., 5:361–362, Oct 1960.

[71] F. Riehle. Frequency Standards: Basics and Applications. Wiley, 2006.

[72] Ian D. Leroux, Monika H. Schleier-Smith, and Vladan Vuletić. Orientation-dependent entanglement lifetime in a squeezed atomic clock. Phys. Rev. Lett., 104:250801, Jun 2010.

[73] Monika H. Schleier-Smith, Ian D. Leroux, and Vladan Vuletić. Squeezing the collective spin of a dilute atomic ensemble by cavity feedback. Phys. Rev. A, 81:021804, Feb 2010.

[74] Justin G Bohnet, Brian C Sawyer, Joseph W Britton, Michael L Wall, Ana Maria Rey, Michael Foss-Feig, and John J Bollinger. Quantum spin dynamics and entanglement generation with hundreds of trapped ions. Science, 352(6291):1297–1301, 2016.

[75] J. Hu, W. Chen, Z. Vendeiro, A. Urvoy, B. Braverman, and V. Vuletić. Vacuum spin squeezing. Phys. Rev. A, 96:050301, Nov 2017.

[76] JC Allred, RN Lyman, TW Kornack, and MV Romalis. High-sensitivity atomic magnetometer unaffected by spin-exchange relaxation. Physical Review Letters, 89(13):130801, 2002.

[77] J. M. McGuirk, H. J. Lewandowski, D. M. Harber, T. Nikuni, J. E. Williams, and E. A. Cornell. Spatial resolution of spin waves in an ultracold gas. Phys. Rev. Lett., 89:090402, Aug 2002.

[78] C. Deutsch, F. Ramirez-Martinez, C. Lacroûte, F. Reinhard, T. Schneider, J. N. Fuchs, F. Piéchon, F. Laloë, J. Reichel, and P. Rosenbusch. Spin self-rephasing and very long coherence times in a trapped atomic ensemble. Phys. Rev. Lett., 105:020401, 2010.

[79] X. Du, L. Luo, B. Clancy, and J. E. Thomas. Observation of anomalous spin segregation in a trapped fermi gas. Phys. Rev. Lett., 101:150401, 2008.

[80] Hidetoshi Katori, Tetsuya Ido, Yoshitomo Isoya, and Makoto Kuwata-Gonokami. Magneto-optical trapping and cooling of strontium atoms down to the photon recoil temperature. Phys. Rev. Lett., 82:1116–1119, Feb 1999.

[81] Kurt R Vogel, Timothy P Dinneen, Alan Gallagher, and John L Hall. Narrow-line doppler cooling of strontium to the recoil limit. IEEE Transactions on Instrumentation and Measurement, 48(2):618–621, 1999.

[82] Simon Stellmer, Benjamin Pasquiou, Rudolf Grimm, and Florian Schreck. Laser cooling to quantum degeneracy. Phys. Rev. Lett., 110:263003, Jun 2013.

[83] P. M. Duarte, R. A. Hart, J. M. Hitchcock, T. A. Corcovilos, T.-L. Yang, A. Reed, and R. G. Hulet. All-optical production of a lithium quantum gas using narrow-line laser cooling. Phys. Rev. A, 84:061406, Dec 2011.

[84] Tetsuya Ido, Yoshitomo Isoya, and Hidetoshi Katori. Optical-dipole trapping of sr atoms at a high phase-space density. Phys. Rev. A, 61:061403, May 2000.

[85] Thomas H. Loftus, Tetsuya Ido, Andrew D. Ludlow, Martin M. Boyd, and Jun Ye. Narrow line cooling: Finite photon recoil dynamics. Phys. Rev. Lett., 93:073003, Aug 2004.

[86] John P. Bartolotta, Matthew A. Norcia, Julia R. K. Cline, James K. Thompson, and Murray J. Holland. Laser cooling by sawtooth-wave adiabatic passage. Phys. Rev. A, 98:023404, Aug 2018.

[87] John P. Bartolotta and Murray J. Holland. Sawtooth-wave adiabatic passage in a magneto-optical trap. Phys. Rev. A, 101:053434, May 2020.

[88] John P. Bartolotta, Jarrod T. Reilly, and Murray J. Holland. Speeding up particle slowing using shortcuts to adiabaticity. Phys. Rev. A, 102:043107, Oct 2020.

[89] John P. Bartolotta, Simon B. Jäger, Jarrod T. Reilly, Matthew A. Norcia, James K. Thompson, Graeme Smith, and Murray J. Holland. Entropy transfer from a quantum particle to a classical coherent light field. arXiv preprint arXiv:2105.03780, 2021.

[90] S. Snigirev, A. J. Park, A. Heinz, I. Bloch, and S. Blatt. Fast and dense magneto-optical traps for strontium. Phys. Rev. A, 99:063421, Jun 2019.

[91] N. Petersen, F. Mühlbauer, L. Bougas, A. Sharma, D. Budker, and P. Windpassinger. Sawtooth-wave adiabatic-passage slowing of dysprosium. Phys. Rev. A, 99:063414, Jun 2019.

[92] G P Greve, B Wu, and J K Thompson. Laser cooling with adiabatic transfer on a Raman transition. New Journal of Physics, 21(7):073045, Jul 2019.

[93] Amir Mahdian, Artjom Krükow, and Johannes Hecker Denschlag. Direct observation of swap cooling in atom–ion collisions. New Journal of Physics, 23(6):065008, jun 2021.

[94] Johann Gan, M. E. Pantalon, and F. Robicheaux. Simulations of sawtooth-wave adiabatic passage with losses. Phys. Rev. A, 101:013422, Jan 2020.

[95] Qian Liang, Tao Chen, Wen-Hao Bu, Yu-He Zhang, and Bo Yan. Laser cooling with adiabatic passage for type-ii transitions. Frontiers of Physics, 16(3):32501, 2020.

[96] Tomoya Akatsuka, Koji Hashiguchi, Tadahiro Takahashi, Noriaki Ohmae, Masao Takamoto, and Hidetoshi Katori. Three-stage laser cooling of sr atoms using the $5s5p^3p_2$ metastable state below doppler temperatures. Phys. Rev. A, 103:023331, Feb 2021.

[97] Shayne Bennetts, Chun-Chia Chen, Benjamin Pasquiou, and Florian Schreck. Steady-state magneto-optical trap with 100-fold improved phase-space density. Phys. Rev. Lett., 119:223202, Dec 2017.

[98] Chun-Chia Chen, Shayne Bennetts, Rodrigo González Escudero, Benjamin Pasquiou, and Florian Schreck. Continuous guided strontium beam with high phase-space density. Phys. Rev. Applied, 12:044014, Oct 2019.

[99] Rodrigo González Escudero, Chun-Chia Chen, Shayne Bennetts, Benjamin Pasquiou, and Florian Schreck. Steady-state magneto-optical trap of fermionic strontium on a narrow-line transition. Phys. Rev. Research, 3:033159, Aug 2021.

[100] Chun-Chia Chen, Rodrigo González Escudero, Jiří Minář, Benjamin Pasquiou, Shayne Bennetts, and Florian Schreck. An ultracold Bose-Einstein condensate in steady state. arXiv preprint arXiv:2012.07605, 2020.

[101] Haonan Liu, Simon B. Jäger, Xianquan Yu, Steven Touzard, Athreya Shankar, Murray J. Holland, and Travis L. Nicholson. Rugged mhz-linewidth superradiant laser driven by a hot atomic beam. Phys. Rev. Lett., 125:253602, Dec 2020.

[102] Hidetoshi Katori, Masao Takamoto, V. G. Pal'chikov, and V. D. Ovsiannikov. Ultrastable optical clock with neutral atoms in an engineered light shift trap. Phys. Rev. Lett., 91:173005, Oct 2003.

[103] Jun Ye, H. J. Kimble, and Hidetoshi Katori. Quantum state engineering and precision metrology using state-insensitive light traps. Science, 320(5884):1734–1738, 2008.

[104] S. B. Nagel, C. E. Simien, S. Laha, P. Gupta, V. S. Ashoka, and T. C. Killian. Magnetic trapping of metastable $^3P_2$ atomic strontium. Phys. Rev. A, 67:011401, Jan 2003.

[105] E. D. Erikson, D. D. Berger, and B. A. Frazier. A comparison of the outgassing characteristics of several solar absorbing coatings. Journal of Vacuum Science & Technology A, 3(3):1711–1714, 1985.

[106] Monika H. Schleier-Smith, Ian D. Leroux, and Vladan Vuletić. States of an ensemble of two-level atoms with reduced quantum uncertainty. Phys. Rev. Lett., 104:073604, Feb 2010.

[107] G. Krenz, S. Bux, S. Slama, C. Zimmermann, and P. W. Courteille. Controlling mode locking in optical ring cavities. Applied Physics B, 87(4):643–647, 2007.

[108] Martin M Boyd, Tanya Zelevinsky, Andrew D Ludlow, Sebastian Blatt, Thomas Zanon-Willette, Seth M Foreman, and Jun Ye. Nuclear spin effects in optical lattice clocks. Physical Review A, 76(2):022510, 2007.

[109] Hidetoshi Katori, Masao Takamoto, VG Pal'Chikov, and VD Ovsiannikov. Ultrastable optical clock with neutral atoms in an engineered light shift trap. Physical Review Letters, 91(17):173005, 2003.

[110] E.T. Jaynes and F.W. Cummings. Comparison of quantum and semiclassical radiation theories with application to the beam maser. Proceedings of the IEEE, 51(1):89–109, 1963.

[111] H J Kimble. Strong interactions of single atoms and photons in cavity qed. Physica Scripta, 1998(T76):127, 1998.

[112] Daniel J. Thompson and Robert E. Scholten. Narrow linewidth tunable external cavity diode laser using wide bandwidth filter. Review of Scientific Instruments, 83(2):023107, 2012.

[113] Albert Ryou and Jonathan Simon. Active cancellation of acoustical resonances with an fpga fir filter. Review of Scientific Instruments, 88(1):013101, 2017.

[114] Markus Greiner, Immanuel Bloch, Theodor W. Hänsch, and Tilman Esslinger. Magnetic transport of trapped cold atoms over a large distance. Phys. Rev. A, 63:031401, Feb 2001.

[115] Daniel Pertot, Daniel Greif, Stephan Albert, Bryce Gadway, and Dominik Schneble. Versatile transporter apparatus for experiments with optically trapped bose–einstein condensates. Journal of Physics B: Atomic, Molecular and Optical Physics, 42(21):215305, oct 2009.

[116] T. L. Gustavson, A. P. Chikkatur, A. E. Leanhardt, A. Görlitz, S. Gupta, D. E. Pritchard, and W. Ketterle. Transport of bose-einstein condensates with optical tweezers. Phys. Rev. Lett., 88:020401, Dec 2001.

[117] Julian Léonard, Moonjoo Lee, Andrea Morales, Thomas M Karg, Tilman Esslinger, and Tobias Donner. Optical transport and manipulation of an ultracold atomic cloud using focus-tunable lenses. New Journal of Physics, 16(9):093028, sep 2014.

[118] D. Schrader, S. Kuhr, W. Alt, M. Müller, V. Gomer, and D. Meschede. An optical conveyor belt for single neutral atoms. Applied Physics B, 73(8):819–824, 2001.

[119] Stefan Schmid, Gregor Thalhammer, Klaus Winkler, Florian Lang, and Johannes Hecker Denschlag. Long distance transport of ultracold atoms using a 1d optical lattice. New Journal of Physics, 8(8):159–159, aug 2006.

[120] J. A. Sauer, K. M. Fortier, M. S. Chang, C. D. Hamley, and M. S. Chapman. Cavity qed with optically transported atoms. Phys. Rev. A, 69:051804, May 2004.

[121] Till Klostermann, Cesar R. Cabrera, Hendrik von Raven, Julian F. Wienand, Christian Schweizer, Immanuel Bloch, and Monika Aidelsburger. Fast long-distance transport of cold cesium atoms. arXiv preprint arXiv:2109.03804, 2021.

[122] Norman F Ramsey. History of early atomic clocks. Metrologia, 42(3):S1–S3, jun 2005.

[123] Audrey Quessada, Richard P Kovacich, Ir ne Courtillot, Andr Clairon, Giorgio Santarelli, and Pierre Lemonde. The dick effect for an optical frequency standard. Journal of Optics B: Quantum and Semiclassical Optics, 5(2):S150–S154, apr 2003.

[124] N.P. Robins, P.A. Altin, J.E. Debs, and J.D. Close. Atom lasers: Production, properties and prospects for precision inertial measurement. Physics Reports, 529(3):265–296, 2013. Atom lasers: production, properties and prospects for precision inertial measurement.

[125] Rym Bouchendira, Pierre Cladé, Saïda Guellati-Khélifa, Fran çois Nez, and Fran çois Biraben. New determination of the fine structure constant and test of the quantum electrodynamics. Phys. Rev. Lett., 106:080801, Feb 2011.

[126] T. Lahaye, J. M. Vogels, K. J. Günter, Z. Wang, J. Dalibard, and D. Guéry-Odelin. Realization of a magnetically guided atomic beam in the collisional regime. Phys. Rev. Lett., 93:093003, Aug 2004.

[127] T. Lahaye, Z. Wang, G. Reinaudi, S. P. Rath, J. Dalibard, and D. Guéry-Odelin. Evaporative cooling of a guided rubidium atomic beam. Phys. Rev. A, 72:033411, Sep 2005.

[128] A Aghajani-Talesh, M Falkenau, V V Volchkov, L E Trafford, T Pfau, and A Griesmaier. Laser cooling of a magnetically guided ultracold atom beam. New Journal of Physics, 12(6):065018, Jun 2010.

[129] Markus Falkenau, Valentin V. Volchkov, Jahn Rührig, Axel Griesmaier, and Tilman Pfau. Continuous loading of a conservative potential trap from an atomic beam. Phys. Rev. Lett., 106:163002, Apr 2011.

[130] B. Knuffman, A. V. Steele, and J. J. McClelland. Cold atomic beam ion source for focused ion beam applications. Journal of Applied Physics, 114(4):044303, 2013.

[131] C. G. Townsend, N. H. Edwards, C. J. Cooper, K. P. Zetie, C. J. Foot, A. M. Steane, P. Szriftgiser, H. Perrin, and J. Dalibard. Phase-space density in the magneto-optical trap. Phys. Rev. A, 52:1423–1440, Aug 1995.

[132] P. Maioli, T. Meunier, S. Gleyzes, A. Auffeves, G. Nogues, M. Brune, J. M. Raimond, and S. Haroche. Nondestructive rydberg atom counting with mesoscopic fields in a cavity. Phys. Rev. Lett., 94:113601, Mar 2005.

[133] J. G. Bohnet, K. C Cox, M. A. Norcia, J. M. Weiner, Z. Chen, and J. K. Thompson. Reduced spin measurement back-action for a phase sensitivity ten times beyond the standard quantum limit. Nat. Photon., 8:731–736, July 2014.

[134] Kevin C. Cox, Joshua M. Weiner, Graham P. Greve, and James K. Thompson. Generating entanglement between atomic spins with low-noise probing of an optical cavity. In 2015 Joint Conference of the IEEE International Frequency Control Symposium the European Frequency and Time Forum, pages 351–356, 2015.

[135] J. Appel, P.J. Windpassinger, D. Oblak, U.B. Hoff, N. Kjærgaard, and E.S. Polzik. Mesoscopic atomic entanglement for precision measurements beyond the standard quantum limit. Proc. Natl. Acad. Sci., 106(27):10960–10965, 2009.

[136] Zilong Chen, Justin G. Bohnet, Shannon R. Sankar, Jiayan Dai, and James K. Thompson. Conditional spin squeezing of a large ensemble via the vacuum Rabi splitting. Phys. Rev. Lett., 106:133601, Mar 2011.

[137] R. J. Sewell, M. Koschorreck, M. Napolitano, B. Dubost, N. Behbood, and M. W. Mitchell. Magnetic sensitivity beyond the projection noise limit by spin squeezing. Phys. Rev. Lett., 109:253605, Dec 2012.

[138] Georgios Vasilakis, Heng Shen, Kasper Jensen, Misha Balabas, Daniel Salart, Bing Chen, and Eugene Simon Polzik. Generation of a squeezed state of an oscillator by stroboscopic back-action-evading measurement. Nature Physics, 11(5):389–392, 2015.

[139] Jérôme Lodewyck, Philip G. Westergaard, and Pierre Lemonde. Nondestructive measurement of the transition probability in a Sr optical lattice clock. Phys. Rev. A, 79:061401, Jun 2009.

[140] Philip Westergaard, Jérôme Lodewyck, and Pierre Lemonde. Minimizing the dick effect in an optical lattice clock. IEEE Trans. Ultr. Ferr. Freq. Cont., 57(3):623–628, March 2010.

[141] G Dick. Local oscillator induced instabilities in trapped ion frequency standards. Proc. of Precise Time and Time Interval, pages 133–147, 1987.

[142] M. G. Raizen, R. J. Thompson, R. J. Brecha, H. J. Kimble, and H. J. Carmichael. Normal-mode splitting and linewidth averaging for two-state atoms in an optical cavity. Phys. Rev. Lett., 63:240–243, Jul 1989.

[143] Yifu Zhu, Daniel J. Gauthier, S. E. Morin, Qilin Wu, H. J. Carmichael, and T. W. Mossberg. Vacuum Rabi splitting as a feature of linear-dispersion theory: Analysis and experimental observations. Phys. Rev. Lett., 64:2499–2502, May 1990.

[144] M. J. Martin, D. Meiser, J. W. Thomsen, Jun Ye, and M. J. Holland. Extreme nonlinear response of ultranarrow optical transitions in cavity qed for laser stabilization. Phys. Rev. A, 84:063813, Dec 2011.

[145] Philip G. Westergaard, Bjarke T. R. Christensen, David Tieri, Rastin Matin, John Cooper, Murray Holland, Jun Ye, and Jan W. Thomsen. Observation of motion-dependent nonlinear dispersion with narrow-linewidth atoms in an optical cavity. Phys. Rev. Lett., 114:093002, Mar 2015.

[146] Bjarke T. R. Christensen, Martin R. Henriksen, Stefan A. Schäffer, Philip G. Westergaard, David Tieri, Jun Ye, Murray J. Holland, and Jan W. Thomsen. Nonlinear spectroscopy of sr atoms in an optical cavity for laser stabilization. Phys. Rev. A, 92:053820, Nov 2015.

[147] S. A. Schäffer, B. T. R. Christensen, M. R. Henriksen, and J. W. Thomsen. Dynamics of bad-cavity-enhanced interaction with cold sr atoms for laser stabilization. Phys. Rev. A, 96:013847, Jul 2017.

[148] Matthew A. Norcia and James K. Thompson. Strong coupling on a forbidden transition in strontium and nondestructive atom counting. Phys. Rev. A, 93:023804, Feb 2016.

[149] T. Takano, M. Fuyama, R. Namiki, and Y. Takahashi. Spin squeezing of a cold atomic ensemble with the nuclear spin of one-half. Phys. Rev. Lett., 102:033601, Jan 2009.

[150] Edwin Pedrozo-Peñafiel, Simone Colombo, Chi Shu, Albert F. Adiyatullin, Zeyang Li, Enrique Mendez, Boris Braverman, Akio Kawasaki, Daisuke Akamatsu, Yanhong Xiao, and Vladan Vuletić. Entanglement on an optical atomic-clock transition. Nature, 588(7838):414–418, 2020.

[151] Yifu Zhu, Daniel J. Gauthier, S. E. Morin, Qilin Wu, H. J. Carmichael, and T. W. Mossberg. Vacuum rabi splitting as a feature of linear-dispersion theory: Analysis and experimental observations. Phys. Rev. Lett., 64:2499–2502, May 1990.

[152] W. F. McGrew, X. Zhang, R. J. Fasano, S. A. Schäffer, K. Beloy, D. Nicolodi, R. C. Brown, N. Hinkley, G. Milani, M. Schioppo, T. H. Yoon, and A. D. Ludlow. Atomic clock performance enabling geodesy below the centimetre level. Nature, 564(7734):87–90, 2018.

[153] G. Cagnoli, L. Gammaitoni, J. Hough, J. Kovalik, S. McIntosh, M. Punturo, and S. Rowan. Very high q measurements on a fused silica monolithic pendulum for use in enhanced gravity wave detectors. Phys. Rev. Lett., 85(12):2442–2445, Sep 2000.

[154] A. D. Ludlow, T. Zelevinsky, G. K. Campbell, S. Blatt, M. M. Boyd, M. H. G. de Miranda, M. J. Martin, J. W. Thomsen, S. M. Foreman, Jun Ye, M. Fortier, J. E. Stalnaker, S. A. Diddams, Y. Le Coq, Z. W. Barber, N. Poli, N. D. Lemke, K. M. Beck, and C. W. Oates. Sr lattice clock at 1×10^{-16} fractional uncertainty by remote optical evaluation with a Ca clock. Science, 319(5871):1805–8, Mar 2008.

[155] D. Leibfried, R. Blatt, C. Monroe, and D. Wineland. Quantum dynamics of single trapped ions. Rev. Mod. Phys., 75(1):281–324, Mar 2003.

[156] S. Blatt, A. D. Ludlow, G. K. Campbell, J. W. Thomsen, T. Zelevinsky, M. M. Boyd, J. Ye, X. Baillard, M. Fouché, R. Le Targat, A. Brusch, P. Lemonde, M. Takamoto, F.-L. Hong,

H. Katori, and V. V. Flambaum. New limits on coupling of fundamental constants to gravity using ^{87}Sr optical lattice clocks. Phys. Rev. Lett., 100(14):140801, Apr 2008.

[157] T. M. Fortier, N. Ashby, J. C. Bergquist, M. J. Delaney, S. A. Diddams, T. P. Heavner, L. Hollberg, W. M. Itano, S. R. Jefferts, K. Kim, F. Levi, L. Lorini, W. H. Oskay, T. E. Parker, J. Shirley, and J. E. Stalnaker. Precision atomic spectroscopy for improved limits on variation of the fine structure constant and local position invariance. Phys. Rev. Lett., 98(7):070801, Feb 2007.

[158] Gil Porat, Christoph M. Heyl, Stephen B. Schoun, Craig Benko, Nadine Dörre, Kristan L. Corwin, and Jun Ye. Phase-matched extreme-ultraviolet frequency-comb generation. Nature Photonics, 12(7):387–391, 2018.

[159] Daniel M. B. Lesko, Henry Timmers, Sida Xing, Abijith Kowligy, Alexander J. Lind, and Scott A. Diddams. A six-octave optical frequency comb from a scalable few-cycle erbium fibre laser. Nature Photonics, 15(4):281–286, 2021.

[160] T. L. Gustavson, P. Bouyer, and M. A. Kasevich. Precision rotation measurements with an atom interferometer gyroscope. Phys. Rev. Lett., 78:2046–2049, Mar 1997.

[161] The AIP National Task Force to Elevate African American Representation in Undergraduate Physics & Astronomy (TEAM-UP). The Time Is Now: Systemic Changes to Increase African Americans with Bachelor's Degrees in Physics and Astronomy. American Institute of Physics, 2020.

[162] Emily M. Levesque, Rachel Bezanson, and Grant R. Tremblay. Physics gre scores of prize postdoctoral fellows in astronomy. arXiv 1512.03709, 2015.

[163] Casey W. Miller, Benjamin M. Zwickl, Julie R. Posselt, Rachel T. Silvestrini, and Theodore Hodapp. Typical physics ph.d. admissions criteria limit access to underrepresented groups but fail to predict doctoral completion. Science Advances, 5(1):eaat7550, 2019.

[164] Mike Verostek, Casey W. Miller, and Benjamin Zwickl. Analyzing admissions metrics as predictors of graduate gpa and whether graduate gpa mediates ph.d. completion. Phys. Rev. Phys. Educ. Res., 17:020115, Sep 2021.

[165] Joshua D Hall, Anna B O'Connell, and Jeanette G Cool. Predictors of student productivity in biomedical graduate school applications. PLoS ONE, 12, 2017.

[166] Liane Moneta-Koehler, Abigail M Brown, Kimberly A Petrie, and Brent J Evans. The limitations of the gre in predicting success in biomedical graduate school. PLoS ONE, 12(1), 2017.

[167] Linda Sealy, Christina Saunders, Jeffrey Blume, and Roger Chalkley. The gre over the entire range of scores lacks predictive ability for phd outcomes in the biomedical sciences. PLOS ONE, 14(3):1–17, 03 2019.

[168] Sandra L. Petersen, Evelyn S. Erenrich, Dovev L. Levine, Jim Vigoreaux, and Krista Gile. Multi-institutional study of gre scores as predictors of stem phd degree completion: Gre gets a low mark. PLOS ONE, 13(10):1–15, 10 2018.

[169] J Guillochon. Gre requirements & admissions fees for us/canadian astronomy & physics programs, Updated 2021.

[170] R A Kusurkar, T J Ten Cate, C M P Vos, P Westers, and G Croiset. How motivation affects academic performance: a structural equation modelling analysis. Advances in Health Science Education, 2013.

Appendix A

Equity Work

A.1 Why Include This?

Physics is fundamentally a human endeavor, as physicists are people and are situated within society. Disregarding the human context of physics research limits who can do physics, what counts as physics, and what physics can achieve.

The fundamental idea of research is to make small contributions towards a greater objective. In a physics department, it is readily acknowledged that building an experiment, taking data, or performing analysis counts as a contribution to a greater whole. Similarly, it is acknowledged that teaching undergrads, mentoring graduate students, and supporting post-docs are worthwhile endeavors to train the next generation of physicists. I will go a step further and say that equity work is the logical progression of work towards the greater whole. Creating an environment where everyone is able to contribute to the fullest of their abilities is of paramount importance, yet it is all too often forgotten or pushed aside. I hope that my efforts, as well as my choice to include this work in my thesis, help to normalize the idea that equity work in a physics department *is* physics.

Finally, another motivation to include my equity work in this thesis is that it documents a significant body of work that may prove valuable to future members of the physics department at CU or to the physics community at large.

A.2 Introduction

I'll begin by unpacking the title, "Equity Work". Equity refers to practices, policies, and structures that ensure everyone can thrive. Equity is different from equality in that equality implies treating everyone as if their experiences are exactly the same. Equality puts everyone on the same footing without acknowledging that in our society, people with marginalized identities face additional barriers. Equity, by contrast, means dismantling the oppressive structures that perpetuate policies and practices which disadvantage marginalized groups.

I'll briefly comment on the second word of the title, "Work". Changing the status quo requires a great amount of work. Not investing effort towards change is a choice to preserve the status quo. On a personal level, I have spent time doing equity work between my duties in physics research and my activities outside of CU, and have been rarely, if ever, formally compensated. I am motivated to do this work because I cannot stand by while I see unopposed unfairness.

I hope that my contributions to equity at CU have laid a pebble in the meandering and branching path towards an equitable enterprise. Many small things add up to physics being an inhospitable environment for many. Although my contributions exist within the oppressive systems of the status quo, I hope to have slightly ameliorated the physics environment for those who follow.

In this Appendix, I discuss the three groups I have been most involved with in my graduate studies: Women and Gender Minorities in Physics (Sec. A.3), R-Cubed (Sec. A.4), and Graduate Admissions (Sec. A.5). In each of these sections, I begin by introducing the group and then discuss particular roles I held and projects I significantly contributed to.

A.3 Women and Gender Minorities in Physics (WaGMiP)

The Women and Gender Minorities in Physics (WaGMiP) group is a community of graduate and undergraduate students, post-docs, and faculty working to support the inclusion, participation, and success of women and gender minorities in the physics department at CU and around the world.

I joined WaGMiP in August 2015, at which point it was called "Women in Physics". It was

led by a faculty member and was primarily a journal club over lunch, where members selected papers to read relating to gender in physics. Over the course of my time in grad school, the name changed to "Women and Gender Minorities in Physics" and the group morphed into a student-led affinity group with activities that are part social event, part networking, and part professional development.

Early on, I helped organize the Conference for Undergraduate Women in Physics (CUWiP) held at CU Boulder in January 2017. On my part, this included applying to host the conference and organizing an event during the conference called the Science Cafe, where undergrads had the opportunity to talk to faculty about their research and life paths in a casual setting.

The main WaGMiP programming centers around monthly lunch meetings, about half of which feature presentations from various speakers affiliated with the University, while the rest are less formal discussions on relevant themes. My chief roles in the monthly lunch meetings have been co-orchestrating the meetings and ordering the food (2016 - 2020). A few of the workshops I helped organize include: a workshop on networking from Career Services, a presentation by Bernadette Park and Erin McPherson from CU's Psychology and Neuroscience Department on their research on gender ideologies, and a workshop on Dismantling Racism from CU Center for Inclusion & Social Change. During the pandemic, the frequency of our monthly meetings fell off and I look forward to helping re-start them in Fall 2021.

In 2018, I founded an event for underrepresented graduate students during the admitted students visiting weekend and have helped organize the event in subsequent years. Over the years, it has taken different forms, starting the first year as a lunch and migrating to a dinner. One lesson I learned is that it is important that the event not be concurrent with any other events, so students do not have to choose between the "traditional program" and the event for underrepresented graduate students. In its current form, WaGMiP hosts a dinner for any student who self-identifies as underrepresented in physics, during the two admitted student open house weekends in the Spring. It takes place after the events of the weekend so that students do not have to miss out on other admissions events. The dinner is an opportunity for admitted students to meet current WaGMiP

members and several faculty members, in an environment that facilitates conversation about anything from physics research to the latest movie to the culture of the department. Additionally, I helped start and organize an effort by current WaGMiP members to reach out to the admitted underrepresented graduate students to welcome them and offer to answer their questions.

Lastly, I helped WaGMiP create an executive committee leadership structure with 5-7 students to ensure the group continues in perpetuity.

A.4 R-Cubed (R^3)

R-Cubed (R^3) is a standing committee in the CU physics department that is focused on improving representation, recruitment, and retention in physics. R^3 is a community effort involving staff, faculty, post-docs, undergraduate, and graduate students to support equity and inclusion in the Physics Department. I served on R^3 from October 2017 until the present. Practically speaking, the membership of R^3 is made up of a few appointed professors, a handful of graduate students, and a staff member, post-doc, and undergraduate or two.

In the Spring of 2020, I and a fellow graduate student led the creation of a semesterly graduate town hall, where the graduate chair gives updates on program requirements and students can ask questions. This was motivated by changes to the graduate program requirements that were only communicated to graduate students via updating the CU Physics website. The town hall proved to be very useful during the pandemic, as there were a lot of uncertainties, especially regarding residency, TAing remotely, and the comprehensive exams.

In 2020, I co-created a departmental diversity statement, as well as a diversity tab on the physics department website. The physics faulty had voted in 2018 to develop a diversity statement, but there had been no development of a statement, so R^3 decided to take on this project. I and another student on R^3 drafted a statement that expressed the value the department places on equity and identified key avenues for improvement. After many iterations incorporating feedback from the department chair, the executive committee of the department, and the rest of R^3, the executive committee voted unanimously to approve the diversity statement.

The diversity statement effort coincided with the department chair Mike Ritzwoller's request for R^3 to create a departmental diversity website. A key feature of the website I advocated for and helped create are anonymous issue forms that can be sent to the department chair or the chair of R^3. These forms attempted to create a mechanism to report issues within the department that are a problem, but do not meet the legal threshold for discrimination (issues that meet the legal threshold are addressed by the Office of Institutional Equity and Compliance). Additionally, we created a resource list of campus support structures and equity groups related to physics. While the creation of the diversity tab content went relatively smoothly, the process of announcing it and adding it to the department's website was very rocky and took several months, mostly because R^3 lacks formal powers and any changes or announcements needed to go through the department chair.

Amidst the national reckoning on racialized police violence, R-Cubed hosted a virtual "town hall meeting with moderated discussion to discuss what specific actions the department could take to improve the climate for underrepresented groups and address structural racism within the department" as part of *#Strike4BlackLives* on June 10, 2020. This town hall had fantastic attendance with > 150 department members. As a breakout room moderator, I observed broad support for improving equity in the department but a low level of awareness of existing efforts.

Combining ideas from the breakout rooms of the town hall, the TEAM-UP report [161], and our own personal research, R-Cubed curated a list of "Immediate Actions to Combat Anti-Black Racism in the CU Physics Department". I served as one of the primary authors of this document, but putting it tother was very much a group effort. After R-Cubed distributed the document at the end of July, I and a group of other students involved in departmental equity work created a petition to demonstrate support for the document. We collected 273 signatures, primarily from students and individuals outside the department (and generated significant backlash within the department). To follow up on the document and facilitate the implementation of the action items, R^3 sought meetings with the departmental chair and executive committee. The executive committee drew up their own list of action items informed by our document, and we have gone back and forth several

times to clarify the meaning of action items, prioritize items, and decide who is responsible for implementing these items.

I am happy to report that since releasing our document, many of our suggested changes have been implemented (although I won't claim any causality, there are many efforts from many people in the department towards equity):

- Creation and funding of Community Of Support for Marginalized Students (COSMOS), a student group for marginalized student in Physics
- Funding for physics students to attend the National Society of Black Physicists (NSBP)
- Creation of the physics department Chair of Inclusion and Diversity
- Creation of service and teaching assistant awards for students to reward efforts in equity and teaching
- Request for an APS site visit from the Committee on the Status of Women in Physics (CSWP) and the Committee on Minorities (COM)
- Initial steps towards the creation of a College of Arts and Sciences Justice, Equity, Diversity, and Inclusion (JEDI) center

Finally, the last R^3-related project I have been involved with was the creation of a graduate student association in physics. In the Winter of 2020, I and another student on R^3 came to the realization that a graduate student association would fill a communication/advocacy gap between graduate students and the department. We quickly recognized the opportunity to build a more comprehensive organization to support physics graduate students and recruited additional organizers (esp. through equity group connections) across student levels. The new association is called Graduate Association of Students in Physics (GASP) and is a student run organization for graduate students from the Physics Department at the University of Colorado. After helping get the ball rolling, I focused on facilitating connections and stepped back from an organizational role in the group.

A.5 Graduate Admissions

Graduate physics programs want the best graduate students. But what does best mean and how should we evaluate the students that apply?

The graduate admissions committee at CU is in charge of graduate admissions and is composed of about 25 faculty members and 2 graduate students. At least two members of the graduate admissions committee read each student's application folder. Committee members make a single quantitative evaluation, the "evaluator score", based on the applicant's personal statement, resume, and letters of recommendation. All applicants are ranked based on their evaluator score, undergrad GPA, Physics GRE, and general and Physics GRE scores. Then, the committee goes through the ranked list and decides whether or not to accept each applicant.

A.5.1 Are our Admissions Metrics Biased?

I first want to answer the question: how is graduate admissions related to equity? The answer is relatively simple: admissions processes and metrics can introduce systematic bias that influence who is admitted.

Here, I will specifically pick on the Physics GRE subject test, as it introduces systematic bias into admissions processes without providing predictive information. A Physics GRE percentile cutoff of 60% would have eliminated 44% of the 2010 - 2015 U.S. prize postdoctoral fellows in Astronomy, including 60% of the female fellows [162]. A 2019 Science Advances article found that the general and Physics GREs fail to predict doctoral completion and limit access to underrepresented groups [163]. A 2021 Phys. Rev. PER article presents an in-depth analysis of 1955 physics graduate students from 19 Ph.D. programs and shows that undergraduate grade point average predicts graduate grades and Ph.D. completion more effectively than GRE scores [164]. They found that students' undergraduate GPA and Physics GRE scores are statistically significant predictors of graduate course grades, while only undergrad GPA is a significant predictor of overall Ph.D. completion. Furthermore, they found that males and females score equally well in their graduate

coursework despite a statistically significant 18 percentile point gap in median Physics GRE scores between genders.

Other studies at UNC Chapel Hill [165], Vanderbilt University [166], Vanderbilt's Initiative for Maximizing Student Diversity [167], and four state flagship institutions [168] come to similar conclusions about the General GRE. Physics departments across the US have slowly started to change their admissions processes and not require the Physics GRE [169].

A.5.2 Analysis of CU's Graduate Admission Metrics

My interest in graduate admissions began while taking the Teaching and Learning Physics class in the Fall of 2017. For my final project for that class, I wrote a 37 page report that presented an analysis of and suggested refinements for CU's physics graduate admissions process. This section contains an overview and abbreviated results from that report.

I wanted to see whether admission metrics are correlated with passing the first two comprehensive exams. I partnered with the graduate chair at the time, Kevin Stenson, to get unidentified admissions data and comprehensive exam scores. Graduate students must pass the comprehensive exams in order to receive their PhD. The first comprehensive exam consists of passing 5 core graduate physics classes and the second comprehensive exam consists of a presentation and paper on a physics topic unrelated to the students research and an oral exam.

In my report, passing comps I is defined as getting a 3.0 or better on the core classes. Passing comps II is defined as passing comps II on the first attempt. I chose these two metrics because they are the most significant barriers to continuing in graduate school. For reference, the vast majority of people satisfactorily completed the 10 graduate classes (4 students of 304 had under a 3.0 graduate gpa). More people failed comps I and II: 15 students of 300 had under a 3.0 in core gpa and 37 students of 207 did not pass comps II on the first try. Note that the number of total students changes because not all students had taken comps II.

Figure A.1 shows the admission metrics of students who passed or failed comps I and II. There is no significant difference in any of the evaluation metrics between students who passed

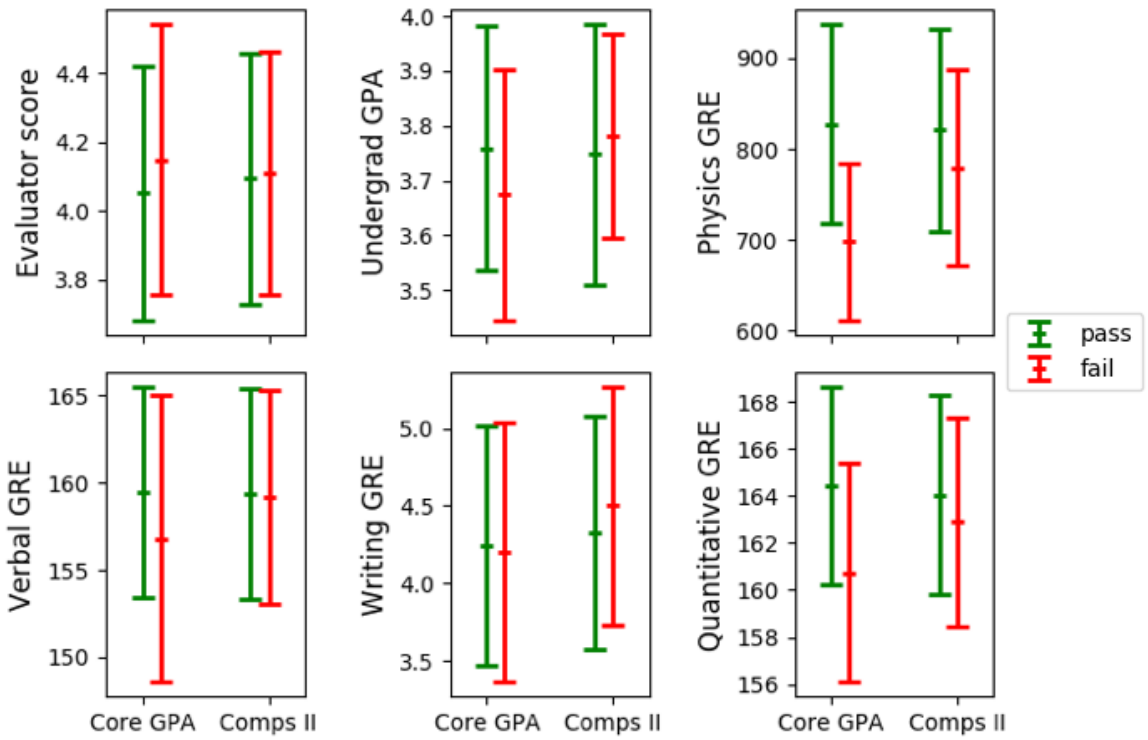

Figure A.1: Admissions metrics for students who passed or failed comps I and II. Error bars are plus and minus one standard deviation. Passing comps I (core gpa) is defined as getting a 3.0 or better on the core classes. Passing comps II is defined as passing comps II on the first attempt. Both passing scores are represented in green and both failing scores are represented in red. There is not a significant difference in any admission metric between students who passed or failed comps II. Students who failed the core gpa tended to do worse on the Physics GRE and quantitative section of the general GRE.

and failed comps II. Students who failed the core gpa tended to do worse on the Physics GRE and quantitative section of the general GRE, but the scores were within one standard deviation of each other.

Our current admission metrics are not a good predictor of who will pass comps I or comps II. The strongest correlation observed here is between performing well on the Physics GRE or the quantitative section of the general GRE and passing comps I. However, what we really care about is who will succeed in a research environment, which is not necessarily associated with performing well in classwork [166]. To have a better metric of admission, it would be useful to have a better metric of evaluating graduate student success.

To refine the idea of success in graduate school, I set out to investigate what characteristics faculty value in prospective graduate students and created a survey asking faculty which traits they found important when admitting graduate students. Kevin Stenson sent out the survey to the physics faculty listserv on behalf of the graduate admissions committee and I. 43 faculty completed the survey (for reference, there are currently 52 tenure-track physics faculty and 145 people on the physics faculty listserv – the listserv includes NIST faculty, several retired faculty, and staff, in addition to the tenure-track faculty).

The survey asks "Of the following, what are the five most important traits for the department to consider when admitting graduate students?" and "Of the following, which five traits does the department measure best when admitting graduate students?". For reference, the traits are shown in Fig. A.2. The order of the traits was randomized to prevent options closer to the top from being selected more often.

Several of the traits can be associated with current admissions criteria. "Good preparation (physics content knowledge)" can be associated with the Physics GRE or undergraduate GPA in physics. "Performs well on timed tests" can be associated with the general and Physics GRE, as well as contributing to the undergraduate GPA. "Good writing skills" can be associated with the writing or verbal sections of the general GRE.

Many other traits are not directly measured by the current admissions process. These traits include "creative," "enthusiastic," "self-motivated, takes initiative," etc. These traits might be referenced in recommendation letters or in the personal statement, but are not necessarily contained in the application.

Figure A.2 shows traits that faculty selected as important (Q 1.1) and traits that faculty think the department measures well (Q 2.1). 42 faculty responded to Q 1.1 and 40 to Q 2.1. There is a significant difference between what faculty deemed important and what faculty think the department measures well.

Additionally, many of the traits that the faculty identified as important are not directly measured by our current admissions process. Of the top seven traits, five of them are non-directly

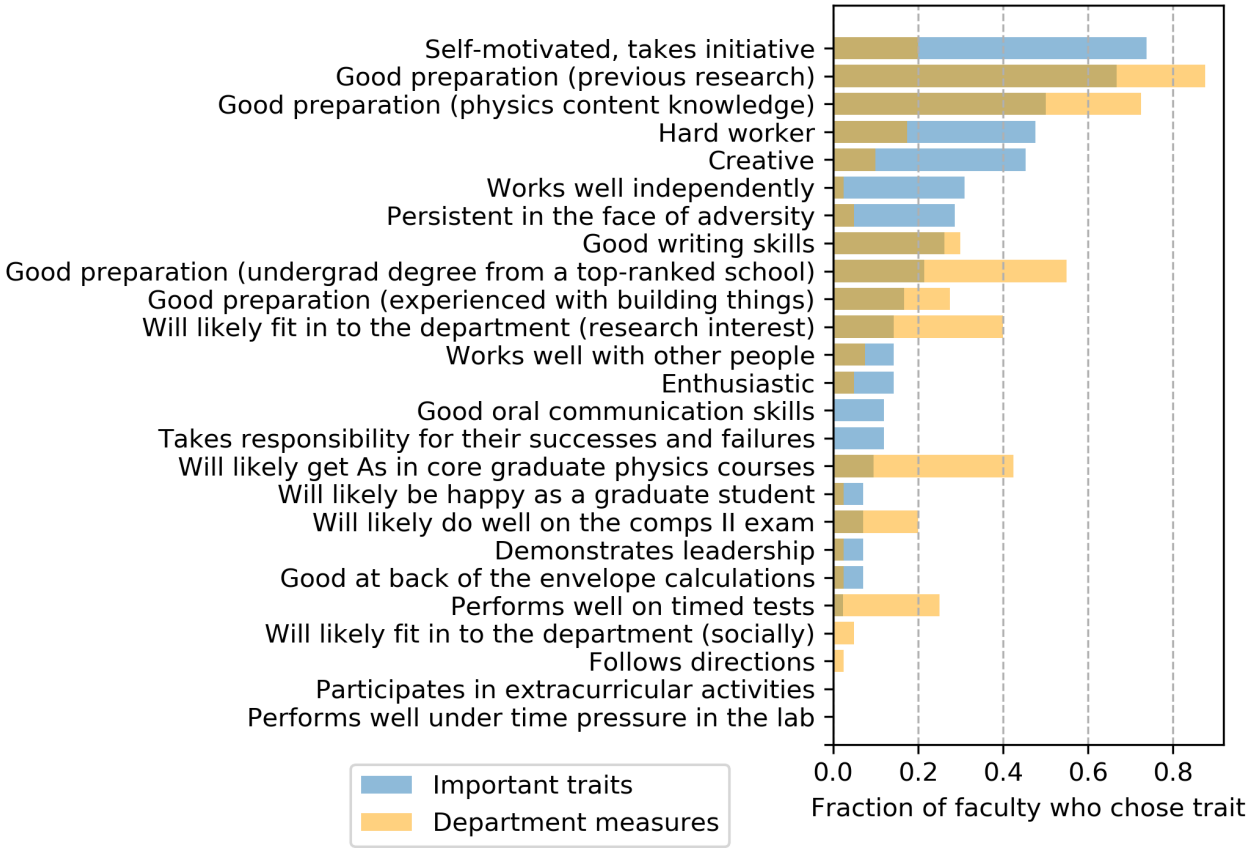

Figure A.2: Results of survey questions Q 1.1: "Of the following, what are the five most important traits for the department to consider when admitting graduate students?" (blue) and Q 2.1 "Of the following, which five traits does the department measure best when admitting graduate students?" (orange). The traits are ordered by the fraction of the faculty who marked the trait as important. There is a significant difference between what faculty deemed important and what faculty think the department measures well. Additionally, many of the traits that the faculty identified as important are not directly measured by our current admissions process (for example, "self-motivated, takes initiative," "hard worker," and "creative").

measurable traits: "self-motivated, takes initiative," "hard worker," "creative," "works well independently," and "persistent in the face of adversity." These traits could be present in the letters of recommendation or personal statement, but may not be mentioned. One could argue that "self-motivated, takes initiative" (for example) is likely correlated with undergrad gpa. Indeed, studies demonstrate a weak correlation between self-motivation and gpa, with a correlation coefficient of about 0.147 [170].

In order to admit students who will be successful in graduate school, we must have an idea

of what success in graduate school means. Our current metrics for evaluating success consist of the graduate gpa, score on comps II, and receiving a PhD. Yet I would argue that success in graduate school is mostly dependent on research, rather than on classwork and exams. The faculty survey was the first step towards refining the idea of success in graduate school. More work is needed to determine admissions metrics that map to success in graduate school and reflect the traits that faculty value in graduate students.

A.5.3 Physics Department Graduate Admissions Committee

In the Spring of 2018, I served on the Physics Department Graduate Admissions Committee. This included reading applications, making admissions decisions, and advocating for the inclusion of applicants from historically underrepresented groups.

While on the admissions committee, one of my highlights was working to change the allocation of signing bonuses. After deciding to accept an applicant, the admissions committee decides how much to offer the student as a "signing bonus". The signing bonus serves as both an incentive for students to decide attend CU and to help cover the costs of moving, such as flights or a rental deposit (although in my year, most people received the signing bonus in October). In the years prior to 2018, signing bonuses had been allocated based on perceived "applicant desirability" and ranged anywhere from $\$0 - 15,000$, with most in the $\$2,000 - 5,000$ range. If they chose to attend CU, students would most likely compare notes and realize that not everyone received the same amount. For those that were awarded smaller amounts, this contributes to a sense of feeling less valued. I advocated for a more inclusive allocation of signing bonuses, where everyone gets a $\$3,000$ signing bonus and a few select students were offered a fellowship, which gave them an extra $\$7,000$. The committee adopted this signing bonus allocation and it has been in place in the years since.

A.5.4 My Efforts to Reform Graduate Admissions

In the Fall of 2020, I and another graduate student decided to implement need-based fee waivers for applicants to CU's graduate physics program. CU's fee is $60 for domestic applicants

and $80 for international applicants. Previously, the department had no structure to award fee waivers and awarded around 1-2 each year in exceptional circumstances. Our goal was to eliminate this barrier for applicants for whom the fee represented a financial burden. We reached out to Eric Cornell, who generously offered to contribute $10k towards domestic fee waivers, which covers 165 waivers (but no international waivers, due to the source of the funding). We modified the language on the website to: "We are aware that the application fee may be an obstacle to applying to our graduate program. For domestic applicants, need-based fee waivers are available upon request. Need may be based on income, personal circumstances, or other need-based circumstances." and we wrote a Qualtrics survey students could fill out to request a fee waiver. For the class of 2021, 29 fee waivers were requested and all of the requests were awarded (the department paid for 2 and Eric funded the others). Of the students who were awarded fee waivers, 4 were admitted! For the longevity of this program, it would be great if there could be department funds set aside for this every year so that it is not dependent on finding a generous donor (thank you Eric!).

In the Winter of 2021, I worked with graduate chair Murray Holland to write a proposal to reform the graduate admissions process at CU for the class of 2022. The goals of this reform were to minimize use of metrics that introduce systematic bias (see Sec. A.5.1) and better match the admissions criteria to characteristics faculty value in grad students (see Sec. A.5.2). Here is a summary of our key proposed changes to the admissions process:

- Change the personal statement to a series of short-answer questions
    - Disadvantages: asking extra of students, they already have personal statements for other institutions.
    - Advantages: potentially faster/easier to evaluate, can directly ask pertinent questions, allows comparison of applicant pool on same basis, can ask multiple choice questions that can be converted to quantitative metrics for use in presorting applications.
- Evaluate candidates on multiple pillars, rather than a single evaluator score

    - Disadvantages: possibly asking more of evaluators.
    - Advantages: allows for scoring on multiple categories, enables weighting categories, and can potentially help mitigate unconscious bias.

- Recruit and retain underrepresented students
- Do not require Physics GRE
    - Whether we decide to keep the Physics GRE in the long term is a separate discussion, but for the class of 2022 there are special considerations due to COVID. The Physics GRE test is only available in person, many testing centers are closed, and due to the uncertainty about vaccines and COVID remedies, we cannot predict what will be available and safe. In combination with the geographical heterogeneity of COVID's effects, this makes it logistically difficult to require the Physics GRE at the point we have to finalize our admissions process (by roughly Jan 2021.)

Murray presented our proposal to the Graduate Committee and they agreed to pursue it further. A subcommittee of the Graduate Committee consisting of myself and three faculty was convened to draft a concrete proposal for admissions for the class of 2022. Our suggested changes to the application were similar to the proposal Murray and I drafted, but smaller in scope:

- Do not require Physics GRE, request students not to report (for class of 2022)
- Change the personal statement to a series of short-answer questions (do not request the personal statement essay).
- Change the multiple choice questions asked on the recommendation letter submission to better normalize the answers.
- Group applicants by broader research interest categories to lessen shot noise.

We also created a list of proposed short-answer questions, possible changes for evaluation and broader admissions, and possible longer-term actions. After drafting and revising this document

as a subcommittee, one of the faculty presented the proposal to the broader admissions committee. While this proposal was not acted upon, I hope that future iterations of the graduate admissions process will minimize use of metrics that introduce systematic bias and better match the admissions criteria to characteristics faculty value in grad students.